Chapter 21
Enceladus: An Active Cryovolcanic Satellite

John R. Spencer, Amy C. Barr, Larry W. Esposito, Paul Helfenstein, Andrew P. Ingersoll, Ralf Jaumann, Christopher P. McKay, Francis Nimmo, and J. Hunter Waite

Abstract Enceladus is one of the most remarkable satellites in the solar system, as revealed by Cassini's detection of active plumes erupting from warm fractures near its south pole. This discovery makes Enceladus the only icy satellite known to exhibit ongoing internally driven geological activity. The activity is presumably powered by tidal heating maintained by Enceladus' 2:1 mean-motion resonance with Dione, but many questions remain. For instance, it appears difficult or impossible to maintain the currently observed radiated power (probably at least 6 GW) in steady state. It is also not clear how Enceladus first entered its current self–maintaining warm and dissipative state- initial heating from non-tidal sources is probably required. There are also many unanswered questions about Enceladus' interior. The silicate fraction inferred from its density of 1.68 g cm^{-2} is probably differentiated into a core, though we have not direct evidence for differentiation. Above the core there is probably a global or regional liquid water layer, inferred from several models of tidal heating, and an ice shell thick enough to support the ∼1 km amplitude topography seen on Enceladus. It is possible that dissipation is largely localized beneath the south polar region. Enceladus' surface geology, ranging from moderately cratered terrain to the virtually crater-free active south polar region, is highly diverse, tectonically complex, and remarkably symmetrical about the rotation axis and the direction to Saturn. South polar activity is concentrated along the four "tiger stripe" fractures, which radiate heat at temperatures up to at least 167 K and are the source of multiple plumes ejecting ∼200 kg s^{-1} of H_2O vapor along with significant N_2 (or C_2H_4), CO_2, CH_4, NH_3, and higher-mass hydrocarbons. The escaping gas maintains Saturn's neutral gas torus, and the plumes also eject a large number of micron-sized H_2O ice grains that populate Saturn's E-ring. The mechanism that powers the plumes is not well understood, and whether liquid water is involved is a subject of active debate. Enceladus provides perhaps the most promising potential habitat for life in the outer solar system, and the active plumes allow the unique opportunity for direct sampling of that zone. Enceladus is thus a prime target for Cassini's continued exploration of the Saturn system, and will be a tempting target for future missions.

J.R. Spencer, A.C. Barr
Southwest Research Institute, Boulder, USA

J.H. Waite
Southwest Research Institute, San Antonio, USA

L.W. Esposito
LASP, University of Colorado, Boulder, USA

P. Helfenstein
Center for Radiophysics and Space Research, Cornell University, USA

A.P. Ingersoll
Division of Geological and Planetary Sciences, California Institute of Technology, Pasadena, USA

R. Jaumann
Institute of Planetary Research, DLR, Berlin, Germany

C.P. McKay
NASA Ames Research Center, Mountain View, USA

F. Nimmo
Dept. Earth and Planetary Sciences, University of California Santa Cruz, Santa Cruz, USA

21.1 Cassini's Exploration of Enceladus

Enceladus (Fig. 21.1) has been known to be an unusual satellite since the early 1980s. The Voyager encounters in 1980 and 1981 revealed Enceladus' extraordinarily high albedo, the highest of any solid body in the solar system, and its heterogeneous cratered and fractured surface terrains (Smith et al. 1982). At around the same time, ground-based observations revealed that Saturn's tenuous E-ring was concentrated at the orbit of Enceladus (Baum et al. 1981). The inferred short lifetimes of the micron-sized E-ring particles implied a continuous source of supply at Enceladus, and geyser-like activity on Enceladus was suggested as a possible source by several authors (Haff et al. 1983, Pang et al. 1984). The neutral OH cloud discovered in the 1990s by the Hubble Space Telescope (Shemansky et al. 1993) also appeared to require a strong source near Enceladus (Jurac et al. 2001).

M.K. Dougherty et al. (eds.), *Saturn from Cassini-Huygens*,
DOI 10.1007/978-1-4020-9217-6_21,

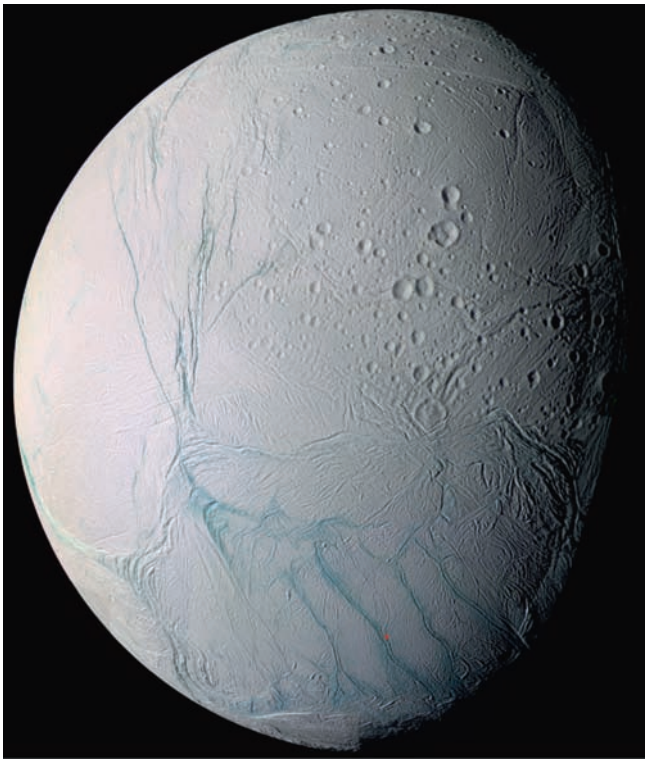

Fig. 21.1 Global false-color view of Enceladus taken by ISS on July 14 2005. The location of the south pole is shown by the red dot, and the four active "tiger stripe" fractures appear as prominent blue-green lines surrounding the pole. From Cassini Press Release PIA06254, NASA/JPL/SSI

Enceladus was thus a high-priority target of the Cassini mission since the program's inception: of the ten targeted flybys of Saturn's mid-sized satellites included in the prime mission tour, three were of Enceladus. In addition, the tour included a fourth close non-targeted Enceladus flyby in February 2005. Flybys in prime mission and subsequent mission extensions are listed in Table 21.1, and the geometry of the closest flybys in the prime and Equinox missions is illustrated in Fig. 21.2.

Cassini's first important Enceladus-related discovery was made even before Saturn orbit insertion. Scans of the Saturn system with the UVIS instrument in early 2004 revealed neutral O emission (Esposito et al. 2005) concentrated near the orbit of Enceladus, complementing the neutral OH emission previously detected. The first close encounters, on orbits 3 and 4, viewed the surface from low latitudes. The ISS images revealed spectacular details of the intense tectonic disruption of the surface and the modification of older cratered terrain (Porco et al. 2006). A stellar occultation observed by the UVIS instrument during the Orbit 3 flyby detected no trace of an atmosphere at the latitudes probed (15 N and 31 S) (Hansen et al. 2006). However, a large perturbation of the ambient magnetic field was seen, indicating a conducting barrier near Enceladus but larger than the moon itself (Dougherty et al. 2006). As a result of a presentation made to the Cassini Project by the Magnetometer Team in April of 2005, in which they noted that their data indicated that Enceladus has a significant atmosphere composed of water-group molecules and ions being continuously replenished (Dougherty et al. 2006), the upcoming July 2005 flyby was modified to reduce Cassini's closest approach distance from a planned 1,000 km to 173 km, to more closely investigate.

It was the July 2005 flyby that revealed with certainty the active nature of Enceladus. The southerly approach provided a good view of the south polar region, and the CIRS instrument detected anomalous thermal emission from the south pole (Spencer et al. 2006) which correlated with four prominent fresh fractures informally dubbed "tiger stripes" seen in detail by the ISS cameras (Porco et al. 2006, Fig. 21.1). Near closest approach, UVIS observed another stellar occultation, and this time detected water vapor over the south pole (Hansen et al. 2006), but not at equatorial latitudes. The south polar water vapor cloud was also detected by INMS, which also found a few percent of CO_2, CH_4, and CO and/or N_2 (Waite et al. 2006). Simultaneously, CDA detected a large concentration of dust grains above the south pole (Spahn et al. 2006a). Combining these data, it became clear that Enceladus' south pole was actively erupting plumes of ice grains, water vapor, and other gases, probably from the tiger stripe fractures, to supply both the E-ring and the neutral torus. Near-IR spectra from VIMS added to the picture, showing concentrations of CO_2 and C-H stretch features near the tiger stripes, consistent with the gas composition (Brown et al. 2006). The dust plumes were then seen directly at high resolution in high-phase ISS images taken on November 27 2005, which revealed multiple individual jets (Porco et al. 2006). Lower-resolution ISS images taken in January and February 2005 also showed the dust plume (Porco et al. 2006), but the plume was not recognized with any certainty at that time, and was not announced.

It was over 2 years till the next close Enceladus flyby, but in the meantime ISS obtained numerous high-phase-angle images of the plume, allowing triangulation of the major plume sources and confirming their location along the tiger stripes, near the warmest regions seen by CIRS (Spitale and Porco 2007), and CIRS observed the south polar hot spot again in November 2006, showing no change in activity since the previous year (Abramov and Spencer 2009).

The very close March 2008 flyby provided an opportunity to penetrate the plume much more deeply than in July 2005, resulting in high quality INMS measurements of the gas composition, and CIRS obtained a high resolution view of the thermal emission along the tiger stripes, revealing heat radiation along the full length of each the fractures imaged. However, because Enceladus was in Saturn's shadow

Table 21.1 Cassini's past and planned close Enceladus flybys

Orbit, encounter name	Date and time (UT)	Speed ($km\,s^{-1}$)	Close approach		Geometry 1 h before encounter		Geometry 1 h after encounter	
			Altitude (km)	Sub-spacecraft point	Sub-spacecraft point	Solar phase	Sub-spacecraft point	Solar phase
3, E0	2005/02/17 03:30	6.7	1,260	239 W, 51 N	318 W, 1 N	27	163 W, 3 N	159
4, E1	2005/03/09 09:08	6.6	497	304 W, 30 S	202 W, 1 S	45	41 W, 0 S	130
11, E2	2005/07/14 19:55	8.2	166	327 W, 22 S	197 W, 48 S	46	36 W, 47 N	132
61, E3	2008/03/12 19:06	14.4	47	135 W, 21 S	125 W, 70 N	114	327 W, 70 S	65
80, E4	2008/08/11 21:06	17.7	50	97 W, 28 S	87 W, 62 N	107	289 W, 63 S	72
88, E5	2008/10/09 19:06	17.7	25	97 W, 31 S	86 W, 62 N	107	289 W, 63 S	72
91, E6	2008/10/31 17:14	17.7	197	97 W, 26 S	86 W, 62 N	107	288 W, 63 S	72
120, E7	2009/11/02 07:41	7.7	99	159 W, 88 S	329 W, 1 S	174	170 W, 0 N	5
121, E8	2009/11/21 02:09	7.7	1,602	112 W, 82 S	189 W, 3 S	145	31 W, 3 S	33
130, E9	2010/04/28 00:10	6.5	99	147 W, 89 S	317 W, 1 S	172	159 W, 0 S	7
131, E10	2010/05/18 06:04	6.5	434	304 W, 34 S	201 W, 0 S	154	42 W, 1 S	27
136, E11	2010/08/13 22:31	6.9	2,550	29 W, 78 S	198 W, 17 S	153	39 W, 4 N	23
141, E12	2010/11/30 11:53	6.3	47	53 W, 62 S	315 W, 0 S	166	156 W, 0 S	14
142, E13	2010/12/21 01:08	6.3	47	232 W, 62 S	314 W, 0 S	166	156 W, 0 S	15
154, E14	2011/10/01 13:52	7.4	99	204 W, 89 S	192 W, 0 S	151	34 W, 1 S	28
155, E15	2011/10/19 09:23	7.5	1,229	114 W, 14 S	189 W, 0 S	154	36 W, 1 S	31
156, E16	2011/11/06 04:59	7.4	495	295 W, 30 S	193 W, 0 S	151	34 W, 0 S	29
163, E17	2012/03/27 18:29	7.2	82	191 W, 76 S	191 W, 0 N	160	32 W, 1 S	20
164, E18	2012/04/14 14:00	6.5	175	206 W, 49 S	191 W, 0 N	160	32 W, 1 S	20
165, E19	2012/05/02 09:31	7.6	73	291 W, 72 S	191 W, 0 N	159	32 W, 1 S	21
223, E20	2015/10/14 10:41	8.4	1,838	106 W, 78 N	185 W, 4 N	23	24 W, 4 N	148
224, E21	2015/10/28 15:22	8.5	48	66 W, 84 S	336 W, 0 N	41	177 W, 1 S	139
228, E22	2015/12/19 17:48	9.5	4,999	353 W, 88 S	342 W, 6 S	46	183 W, 10 S	144

while the south pole was in view, the highest-resolution remote sensing with other instruments covered the northern hemisphere.

Cassini's first extended mission, the "Equinox Mission", from mid-2008 to -2010, includes seven additional close Enceladus flybys designed to follow up on the discoveries of the prime mission (Table 21.1). The first three were high-inclination passes with good sunlit views of the south pole on departure, and included deep passages through the plume in orbits 80 and 88 and very high resolution remote sensing on orbits 80 and 91. The four flybys in orbits 120 – 131 are low inclination passes which can only observe the south pole near closest approach, but will provide good coverage of low latitudes. These flybys include the deepest plume penetrations yet planned, on orbits 120 and 130, and a mixture of occultations, gravity observations, and remote sensing including high-resolution observations of the plume jets.

At the time of writing, a second extended mission, the "Solstice Mission", has been designed but is not yet approved for funding. This extension includes 12 additional Enceladus flybys through 2015 (Table 21.1). The south pole will be largely in darkness for most of this mission phase, and remote sensing of the south pole will be largely restricted to thermal and Saturn-light observations, and observations of the upper parts of the jets and plume that extend thousands of kilometers above the pole. There will also be several more close south polar flybys to sample the plume and investigate its longer-term variability.

21.2 Interior and Tidal Heating

21.2.1 Introduction

Cassini observations of Enceladus' active south polar region confirm that this tiny moon ranks alongside the Earth, Io, and possibly Triton as one of the few currently volcanically or cryovolcanically active worlds in the solar system. Much of the endogenic power output is concentrated within linear features referred to as "tiger stripes" (Spencer et al. 2006, Porco et al. 2006), which are also the source of the plume materials (Spitale and Porco 2007). Characterization of tectonic features elsewhere on Enceladus indicates that heat flows comparable to values presently observed in the south polar terrain (SPT) may have been present in those regions at the time of deformation (Bland et al. 2007, Giese et al. 2008).

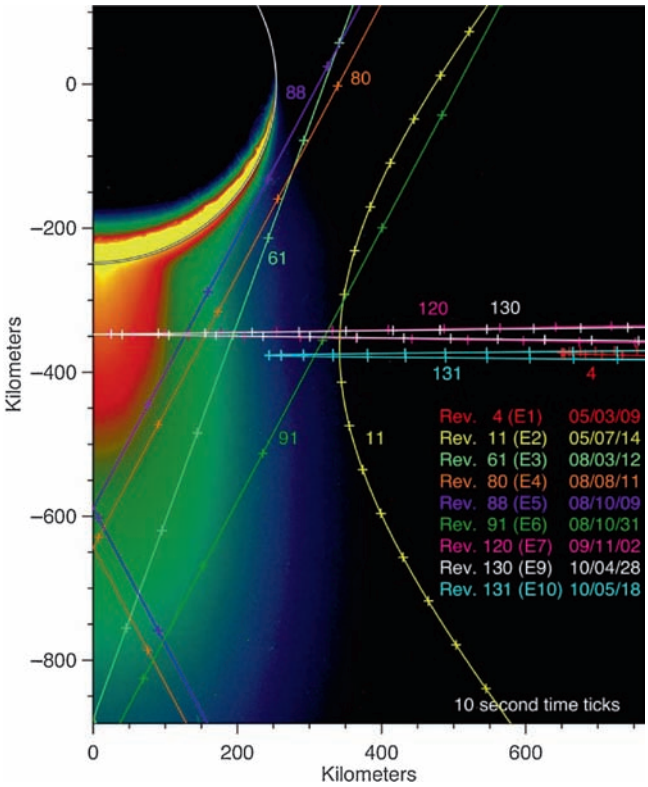

Fig. 21.2 The geometry of Cassini's closest Enceladus flybys during the prime and Equinox missions (Table 21.1) is shown relative to the south polar plume, assuming rotational symmetry about the spin axis. The plume image, taken on April 24 2007, is stretched logarithmically to highlight the faint outermost regions of the plume. Tick marks are shown at 10 s intervals

This suggests that the strong heating occurring presently in the SPT may have occurred at other locations in Enceladus in the past (Section 21.3.2). In contrast, other regions of the surface, particularly in the northern hemisphere, are quite heavily cratered and may be several billion years old (Kargel and Pozio 1996, Porco et al. 2006). Such profound variations in interior structure and surface morphology across the satellite suggest that Voyager-era models, all of which assume a radially symmetric interior structure, probably do not capture key processes driving its past and present-day activity.

Observations of Enceladus offer a chance to understand the origin of cryovolcanism, and the observed heat flux from the SPT provides a unique opportunity to constrain geodynamical models. The main source of Enceladus' energy is undoubtedly tidal dissipation, maintained over long time scales by Enceladus' 2:1 mean motion resonance with neighbor satellite Dione (e.g., Murray and Dermott 1999). Thus, Enceladus provides a unique natural laboratory for the study of how the interaction between tidal flexing, interior thermal and compositional heterogeneity, and heat transport gives rise to cryovolcanism and resurfacing on icy bodies. In this section we will focus on the interior of Enceladus, addressing its state of differentiation, heat sources, heat transport mechanisms, and the time evolution of its interior structure. The question of whether or not Enceladus has a subsurface ocean is of particular interest, not only because the presence or absence of an ocean strongly affects the generation of tidal heat, but also because its ocean is potentially habitable.

21.2.2 Bulk Structure

21.2.2.1 Observational Constraints

Three types of observations can be made by Cassini to infer the internal structure of Enceladus: bulk density, shape, and gravity moments. Based on Cassini observations, the mean radius of Enceladus is 252 km, $GM = (7.207 \pm 0.011) \times 10^9\,\mathrm{m^3\,s^{-2}}$, and its bulk density is $1{,}608 \pm 5\,\mathrm{kg\,m^{-3}}$ (Jacobson et al. 2006, Thomas et al. 2007, Rappaport et al. 2007), much higher than Voyager density estimates of roughly $1{,}200\,\mathrm{kg\,m^{-3}}$ (Smith et al. 1982). Given its mean density, Enceladus is likely composed of rock and ice, with a rock mass fraction of roughly 50–60%. A fully differentiated Enceladus would have an H_2O layer 60–100 km thick, which may be partly liquid in the form of a global ocean (Nimmo and Pappalardo 2006, Barr and McKinnon 2007a, Schubert et al. 2007). Pressures reach 1 MPa at depths of ∼10 km on Enceladus, so near-surface porosity is unlikely to significantly affect its bulk density.

Enceladus' measured principal axes indicate that its interior is not in hydrostatic equilibrium. If Enceladus were in hydrostatic equilibrium, its shape could be used to infer its polar moment of inertia (e.g., Dermott and Thomas 1988) and state of differentiation. The measured radii a, b and c are 256.6, 251.4 and 248.3 km (Thomas et al. 2007), respectively, with uncertainties of 0.6, 0.2 and 0.2 km, respectively. The derived quantity $(a–c)/(b–c) = 2.7 \pm 0.5$, much lower than 4.0, the expected value for a hydrostatic body. Porco et al. (2006) argue that the observed value of $a - c$ is also smaller than that expected for a hydrostatic, differentiated body with the present-day rotation rate, and thus that Enceladus is either undifferentiated (or slightly differentiated), or was rotating more rapidly (and perhaps closer to Saturn) when the shape was acquired. The former possibility is unlikely (see Schubert et al. 2007 and below); the latter possibility requires that Enceladus have a finite rigidity (in order to maintain its shape) and is thus non-hydrostatic at the present day, though it is unlikely that Enceladus has undergone much orbital evolution (Porco et al. 2006). If Enceladus is fully differentiated and in hydrostatic equilibrium, its shape indicates an asymmetric interior distribution of mass (Porco et al. 2006). Collins and Goodman (2007) point out that the original value of c might have been affected by melting and

subsidence at the south pole, and that a differentiated Enceladus may be consistent with the shape observations. Note that this approach again implicitly assumes a non-hydrostatic Enceladus at the present day.

Degree-2 gravitational coefficients determined from spacecraft radio tracking are commonly used to infer a satellite's interior density structure, but this inversion can only be performed if the satellite's interior is in hydrostatic equilibrium (e.g., Rappaport et al. 2007). At present, the gravity coefficients of Enceladus are unknown, but given the apparently non-hydrostatic nature of this satellite, measuring these coefficients will at best provide only a limited improvement in our understanding of its internal structure. One method of determining the moment of inertia without requiring the hydrostatic assumption is to measure both the degree-2 gravity coefficients and the obliquity (Bills and Nimmo 2008). However, this technique requires an alternative assumption: that the obliquity is tidally damped, such that the spin axis, orbit pole and pole of the ecliptic are coplanar (i.e., a Cassini state, Bills et al. 2009). At present we do not know Enceladus' rotational state well enough to test this assumption.

21.2.2.2 Indirect Arguments

In addition to direct observational constraints, theoretical arguments based on heat sources and thermal evolution models can be used in combination with observations to give likely interior structures (see e.g., Schubert et al. 2007 for discussion). Existing arguments are based on thermal evolution models of Enceladus, or on its observed present-day heat flux. The present-day observed heat flux at the south pole of Enceladus is at least 5.8 ± 1.9 GW (Spencer et al. 2006). This power is much larger than the current radiogenic heat production, and is likely a result of tidal heating (Spencer et al. 2006, see Section 21.2.4 below). Even in the absence of tidal heating, a conductive Enceladus is marginally capable of differentiating in the presence of long-lived radionuclides, and is certain to differentiate if significant amounts of the short-lived nuclide ^{26}Al are present at the time of its formation (Schubert et al. 2007).

Because the tidal heating experienced by a differentiated Enceladus depends strongly on its interior structure, estimates of Enceladus' tidal heat flux may provide clues about its interior structure. Ross and Schubert (1989) showed that a homogeneous undifferentiated (uniform-density ice-rock) Enceladus could generate as much as 920 GW, but only if the viscosity were as low as 10^{12} Pa s. This value is too low even for pure ice (Goldsby and Kohlstedt 2001), and certainly too low once the likely effects of silicate particulates on ice viscosity (Friedson and Stevenson 1983, Durham et al. 1992) are included. For a more reasonable viscosity of 10^{14} Pa s (Durham and Stern 2001), assuming a plausible grain size near 1 mm (Barr and McKinnon 2007a) and rigidity of 3 GPa, the heat production for a uniform Enceladus is 2 GW, less than but more comparable to the observed value. The presence of a rigid silicate core will reduce the amplitude of the tidal deformation and produce a lower heat flow. However, the presence of an ocean decoupling the ice shell from the silicate interior enhances the total volumetric tidal heat production by a factor of $\sim$10 (Roberts and Nimmo 2008a). A differentiated Enceladus without an ocean does not generate enough heat to account for the observations, but in cases with a subsurface ocean, the modeled *global* heat production is comparable to that observed (Roberts and Nimmo 2008a). Tobie et al. (2008) examined heating with lateral variations in viscosity, and concluded that to reproduce the amplitude and pattern of heating observed, either a global ocean or a liquid layer spanning a major part of the southern hemisphere is required. Nimmo et al. (2007) examined a different mechanism of tidal heating, wherein friction due to strike-slip motion along faults generates heat in the shallow subsurface of the ice shell, but also concluded that a subsurface ocean was required to generate the observed heat flow.

An alternative to a global ocean model is a model wherein the south polar hot spot sits above a local "sea" (Collins and Goodman 2007). Melting of the ice shell to generate the sea could explain the low topography at the south pole, but requires either strong heating from Enceladus' silicate interior or the downwards percolation of melt from within the ice shell (Tobie et al. 2008). As discussed in Section 21.2.4 below, it is difficult to generate enough tidal heating within the silicates to melt the ice shell in the manner envisioned by Collins and Goodman. Melt generation within the ice shell is possible, but has not yet been quantitatively demonstrated.

The high regional heat fluxes in the south polar region, averaging at least $\sim$100 mW m^{-2} over the region S of 55° S, could imply the presence of water at a depth of only 6 km. However, this calculation assumes that the heat is transported by conduction, which may not be correct: Spencer et al. (2006) and Nimmo et al. (2007) argue that the bulk of the heat is advected (by flow of vapor) and thus that the subsurface thermal gradient cannot be inferred from the heat flow measurements. See Section 21.5.3.1.

21.2.2.3 Discussion and Summary

Most existing models assume that Enceladus is presently differentiated, even though the direct evidence supporting this hypothesis is weak. The strongest argument for a differentiated Enceladus is its large heat flux, which seems to require a differentiated structure and a global subsurface ocean (see below). Shape measurements suggesting a non-hydrostatic interior, and the significant north-to-south variations in Enceladus' geology, both indicate that deductions

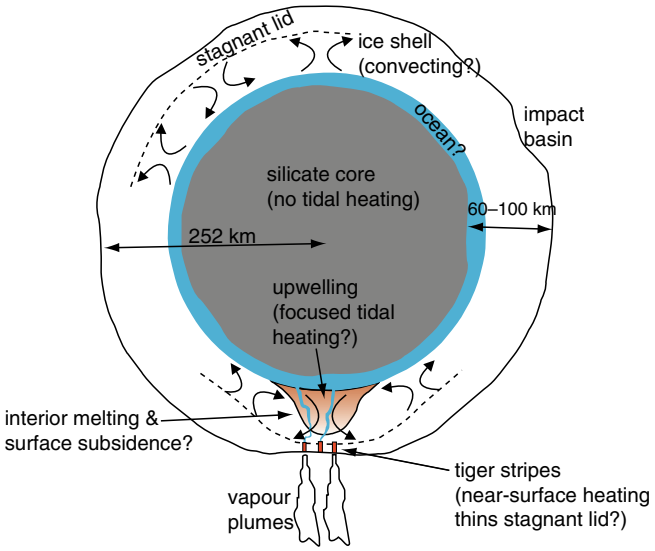

Fig. 21.3 A sketch of the potential internal structure of Enceladus, after Nimmo and Pappalardo (2006), Schubert et al. (2007) and Tobie et al. (2008). The amplitude of the surface topography is exaggerated. The arguments for a convective interior and thinning of the lithosphere near the south pole are presented in Section 21.2.5

about the interior structure cannot be made from the static gravitational field by assuming hydrostatic equilibrium and a radially symmetric structure. More complex models will be required, which will be less likely to yield unique solutions.

Figure 21.3 is a sketch illustrating our current understanding of Enceladus, aspects of which are discussed through the remainder of this section. The presence of question marks indicates the uncertainty of many of the inferences made.

21.2.3 Interior Composition and Chemistry

The plume of water vapor and other materials erupting from Enceladus' south pole provides the first opportunity to directly sample material from the interior of an icy satellite. Cassini INMS data (Section 21.5.2.4) suggest that Enceladus' gas plume is composed of roughly 90–94% water vapor by mass, plus 5% CO_2, 0.9% CH_4, and 0.8% NH_3, and small amounts of organics, H_2S, and ^{40}Ar. There may also be significant N_2, though this is uncertain because INMS cannot distinguish N_2 from C_2H_4 (Waite et al. 2009). CAPS measurements of magnetospheric nitrogen ions detect nitrogen in the plume: the data imply a source of nitrogen and perhaps NH_3 at Enceladus (Smith et al. 2008a, b). Most E-ring particles measured by CDA appear to contain a small amount of sodium, and some are rich in both NaCl and $NaHCO_3$ (Postberg et al. 2009 and Section 21.5.2.5), suggesting an oceanic provenance. However, the abundances of CO_2, CH_4, and perhaps other gas species are too high to originate from gas dissolved in liquid (Waite et al. 2009), and subsurface clathrates have been suggested as a source for these species (Kieffer et al. 2006).

The compositional measurements from Enceladus have so far been interpreted in two contexts: as a constraint on its present-day ocean chemistry, and as a constraint on Enceladus' early thermal evolution. Calculations of the water-rock chemistry occurring over Enceladus' lifetime suggest that its present ocean should include significant Na-Cl-HCO_3 (Zolotov 2007), consistent with the CDA measurements of E-ring particle composition.

Because nitrogen is likely delivered to Enceladus from the solar nebula in the form of NH_3 clathrate within ice grains during its accretion (Mousis et al. 2002, Lunine and Gautier 2004), the conversion from ammonia to molecular nitrogen (if present) likely occurs within Enceladus itself (Matson et al. 2007, Glein et al. 2008). Matson et al. (2007) suggest that N_2 is formed from NH_3 by thermal decomposition, which requires high temperatures (∼500–800 K) within the silicate core, and further suggest that the satellite's interior had been heated to these temperatures by a combination of short-lived radioisotopes (SLRI's, such as ^{26}Al and ^{60}Fe) and tidal heat early in its history. Glein et al. (2008) favor a different evolutionary pathway for nitrogen, in which the NH_3 to N_2 conversion occurs within hydrothermal systems created during an early phase of core volcanism driven by SLRI's.

The apparent presence in the plume of ^{40}Ar, which originates from radioactive decay in Enceladus' silicate fraction, is also likely to constrain the interior evolution of Enceladus (Waite et al. 2009).

It should also be noted that if the current plume gas production rate of about 200 kg s^{-1} has been maintained over the age of the solar system, Enceladus would have lost about 20% of its mass and 40% of its water, with drastic consequences for its chemical and physical evolution (Kargel 2006), including a loss of volatile elements and a major reduction in radius.

21.2.4 Heat Production and Tides

Observations of the south polar heat flow anomaly place direct constraints on heat production within Enceladus. The observed heat flow is at least 5.8±1.9 GW (Spencer et al. 2006), and is likely to be higher, because published observations are insensitive to heat radiated at temperatures below about 85 K. The observed power significantly exceeds the expected radiogenic contribution of ∼0.3 GW (Porco et al. 2006, Schubert et al. 2007), suggesting that the bulk of the energy is derived from tidal dissipation (cf. Squyres et al. 1983,

Ross and Schubert 1989). Although this conclusion appears robust, many details of the heat production are still poorly understood.

Tidal heating arises because a satellite in an eccentric orbit experiences a tidal bulge that varies in amplitude and location over the course of the orbit. These time-dependent strains will dissipate energy if the deforming material is not perfectly elastic (i.e., if there is a phase lag). For a synchronous satellite the dissipation rate can be written as (e.g., Peale and Cassen 1978)

$$\dot{E} = -\frac{21}{2}\frac{k_2}{Q}\frac{(\Omega R)^2}{G}e^2$$

where Ω, e and R are the orbital angular frequency and eccentricity and the satellite radius, respectively, and G is the gravitational constant. The quantity k_2 is the magnitude of the tidal Love number, which depends on density and rigidity of the satellite and determines the amplitude of the tidal bulge. The quantity Q is the quality factor: $Q/(2\pi)$ is the ratio between the total energy of an oscillation and the energy dissipated per cycle, and is proportional to the phase lag of the tidal bulge. Q can be calculated if the specific dissipation mechanism is known- smaller values imply a more dissipative interior. The tidal Q is generally poorly known and on the Earth is observably frequency-dependent (e.g., Anderson 1989, Benjamin et al. 2006).

Geological materials exhibit both a brittle/elastic behavior described by a rigidity, μ, and ductile behavior, described by a viscosity, η. The most commonly used viscoelastic model, which best approximates the behavior of real geological materials, is the Maxwell model (Ross and Schubert 1986). For Maxwellian materials the phase lag depends on the ratio of the forcing period to the characteristic relaxation or Maxwell time ($= \eta/\mu$) (Ross and Schubert 1986). For a Maxwell body the Love number is complex and k_2/Q is given by $Im(k_2)$ (Zschau 1978). Assuming a Maxwell rheology, the total tidal dissipation, and the spatial distribution of this heating, may be calculated for an arbitrary satellite structure (Segatz et al. 1988, Tobie et al. 2005).

An early application of this method to Enceladus was performed by Ross and Schubert (1989), who demonstrated that significant (up to $\sim$1 TW) tidal heating could occur in a viscoelastic Enceladus, depending on material properties, though the properties required for the highest heat flows were not necessarily realistic (Section 21.2.2.2). More recently, Roberts and Nimmo (2008a) investigated viscoelastic tidal dissipation in Enceladus in some detail. They assumed a radially symmetric body with a uniform silicate layer, an optional ocean and an ice shell in which the temperature and viscosity structure were appropriate to either a conductive or a convective setting. Tidal dissipation in the silicates was found to be negligible for any likely viscosity. This conclusion is important because Collins and Goodman (2007) require significant silicate heating to explain the south polar topographic depression. Dissipation in the ice shell increases by a factor of $\sim$10 if the shell is decoupled from the interior by an ocean. For models with a subsurface ocean, the global heat flow is comparable to or exceeds the measured heat flow of the south polar thermal anomaly. However, the spatial pattern of the modeled heating has maxima at both poles, in contrast to the observations.

This last point illustrates a basic problem with almost all published tidal heating models: they are symmetrical about the equator, which is not the case for the heat flow on Enceladus. Enceladus may have large lateral variations in mechanical properties, which can in turn focus tidal heating. A recent study by Tobie et al. (2008) calculates the tidal dissipation in a non-radially symmetric body and confirms that tidal heating can indeed be focused in a warm upwelling, as suggested by previous authors (Sotin et al. 2002, Mitri and Showman 2008). The focusing of tidal heating may explain the high heat flux at the south pole, if this region is indeed the site of an upwelling diapir (Nimmo and Pappalardo 2006).

Most tidal heating models focus only on eccentricity tides. However, tidal heating can also occur if Enceladus has a non-zero obliquity, or if it is undergoing forced rotational librations (Wisdom 2004, see his Equation 45). Forced librations can occur if the libration and spin frequencies are in a simple integer ratio (Wisdom 2004), however, no librations have been detected within uncertainty ($\pm$0.026 radian), implying a current librational heating that is at most comparable to radiogenic heating (Porco et al. 2006). The obliquity of Enceladus is currently unknown, but based on theoretical investigations of the Galilean satellites (Bills 2005) it is likely to be small but non-zero, and could contribute to the total tidal heating.

It is also not yet clear that the Maxwellian rheology is appropriate to real planetary materials, including water ice. For instance, both observations and laboratory measurements of silicates suggest that Q has a significantly weaker dependence on frequency than the Maxwell model implies (e.g., Anderson 1989, Gribb and Cooper 1998, Karato 1998, Jackson et al. 2004, Benjamin et al. 2006). Another non-Maxwellian process that may be important is friction on shallow faults. Tidal stresses can cause oscillatory strike-slip motion (Hoppa et al. 1999), which can in turn cause shear heating (Nimmo and Gaidos 2002). Shear heating is a possible way of explaining the high temperatures of the tiger stripes relative to the surrounding terrain (Nimmo et al. 2007), and exhibits fundamentally different dependencies compared with equation (1). A third non-Maxwellian process of possible interest is turbulent dissipation in the subsurface ocean (Nash et al. 1986, Ross and Schubert 1989, Tyler 2008). Shallow seas on Earth are the dominant location of tidal dissipation: on Enceladus, dissipation in a thin ocean

could generate several GW of heat. Developing dissipation models using more realistic rheologies is likely to be another focus of future work.

21.2.5 Thermal Structure

The spatial localization of Enceladus' activity at its south pole strongly suggests that tidal dissipation has become concentrated there. As described in Section 21.2.4, most tidal dissipation models (e.g., Ojakangas and Stevenson 1989, Tobie et al. 2005, Roberts and Nimmo 2008a) imply that dissipation should be concentrated in warm ice in Enceladus' ice shell, and should be broadly distributed as a function of latitude and longitude. Tobie et al. (2008), however, showed that a low viscosity region can focus tidal deformation and heating, and suggested that episodic behavior might result. Nimmo and Pappalardo (2006) suggest that the activity is concentrated in the south polar region because a large density perturbation in its ice shell and/or rocky interior caused the satellite to "roll over" to place this active region on the satellite's rotation axis. Solid state convection would be one way of creating a thermal and density anomaly in the ice shell, although it is currently unclear why only one such convective plume should have developed (cf. Grott et al. 2007), or whether a purely thermal plume could generate a sufficiently large mass anomaly. Localization of tidal heating probably requires some thermal, compositional, or mechanical anomaly.

Convection may also play a role in Enceladus' interior evolution by regulating the temperature in its interior. Barr and McKinnon (2007a) find that initiating convection in a floating conductive ice I shell on Enceladus may be difficult, in part because of the satellite's low gravity, which implies that thermal buoyancy stresses created by local temperature highs and lows (which are required as initial perturbations for the onset of convection) are very low. As a result, convection can only begin in a the thickest possible ice shell ($D \sim 100$ km) with a low melting point viscosity, implying that grain sizes in the warm ice at the base of its shell must be less than 0.3 mm, close to the lower limit on grain size in natural terrestrial systems (i.e., glaciers) (McKinnon 2006, Barr and McKinnon 2007b). Tidal dissipation may play a role in helping to trigger ice shell convection if tidal heat can create pockets of warm ice on length scales comparable to the thickness of Enceladus' ice shell, a length scale comparable to the size of temperature fluctuations maximally efficient at triggering convection (Solomatov and Barr 2007). Other modes of convection have also been proposed, including "whole-Enceladus" degree-1 convection in an undifferentiated or partially differentiated satellite (Grott et al. 2007). Such a pattern would provide a natural means of creating a large thermal anomaly at one location in Enceladus, which could be further amplified by tidal dissipation to create the north/south dichotomy.

Spread over the $\sim$70,000 km^2 region of the south polar terrain (Porco et al. 2006), the total power output of at least 5.8 ± 1.9 GW (Spencer et al. 2006) corresponds to a heat flux $F = 55$ to 110 mW m^{-2}. Because the viscosity of water ice is strongly temperature dependent, most existing models of convective heat transfer in Enceladus' ice shell assume that convection occurs beneath a thick "stagnant lid" of highly viscous, immobile ice at the satellite's surface. The stagnant lid inhibits convective heat transport by preventing convective plumes from reaching close to the surface of the satellite. On Enceladus, the upper limit on the heat flux from stagnant lid convection is $F \sim 20$ mW m^{-2} (Barr and McKinnon 2007a, Barr 2008, Roberts and Nimmo 2008a), a factor of $\sim$3–4 less than the regional heat flux within the SPT.

However, if the near-surface ice on Enceladus is very weak, convective plumes can reach closer to the surface of the satellite, permitting the observed SPT heat flux to be carried by convection in a thick ice shell rather than by conduction in a thin ice shell. If the yield strength of Enceladus' lithosphere within the SPT region is less than $\sim$10 kPa, convection occurs in the "sluggish" or "mobile-lid" regime, characterized by larger heat fluxes comparable to the observed value, and horizontal velocities $\sim$1–10 m year^{-1} (Barr 2008). Lithospheric spreading associated with convection in a weak ice shell may provide a natural explanation for the region's $<$0.5 Myr surface age (Porco et al. 2006) and the compressional tectonics at its flanks (Helfenstein et al. 2009, and Section 21.3). The ice shell of Enceladus within the SPT may become mechanically weakened by cyclical tidal deformation (Barr 2008), or thermally weakened by tidal dissipation in the shallow subsurface (Roberts and Nimmo 2008b).

The effects of the recent detection of NH_3 in the plume (Waite et al. 2009, and Section 21.5.2.4), and therefore in the interior of Enceladus, on the internal rheology and thermal state of the ice shell may be significant, but have yet to be considered in detail.

The surface topography of Enceladus provides an important additional constraint. Limb profiles (Thomas et al. 2007), suggest topographic variations with amplitudes of hundreds of meters on wavelengths of $\sim$100 km. These wavelengths are comparable to those predicted by theoretical convection models (see Fig. 21.4), but the amplitudes are much larger than predicted for stagnant lid convection. The amplitudes will be larger if there is lithospheric yielding (Showman and Han 2005) or compositional buoyancy contrasts. The latter effect may arise if tidal heating is focused within upwelling regions (Sotin et al. 2002, Mitri and Showman 2008), leading to melting and removal of dense contaminants (cf. Pappalardo and Barr 2004).

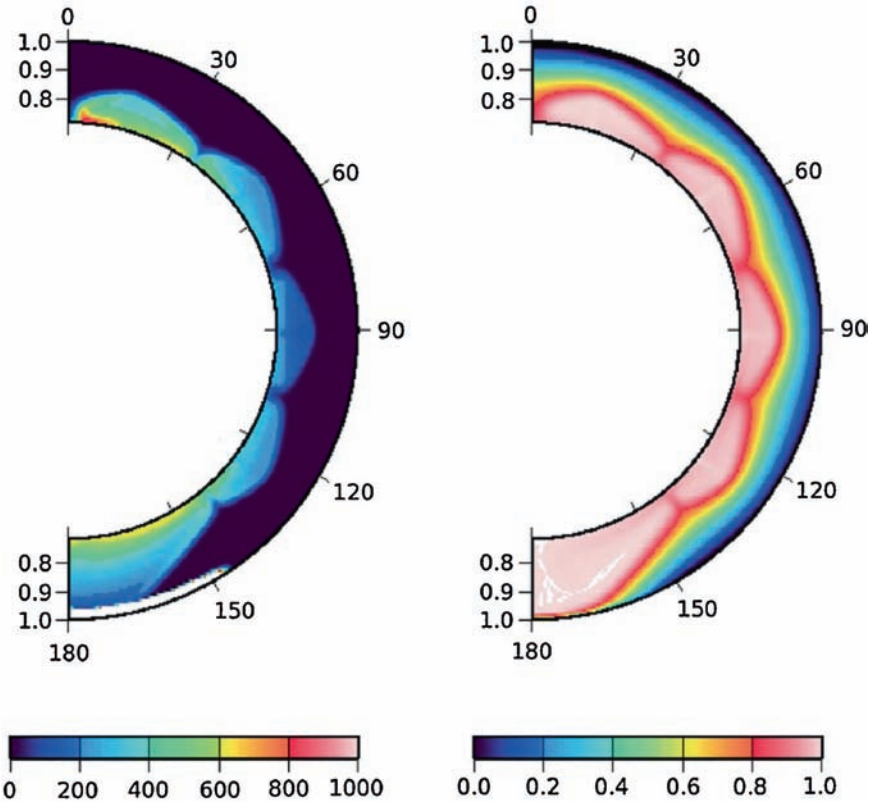

Fig. 21.4 Plot of heating rate in units of 10^{-9} W m^{-3} (*left*) and dimensionless internal temperature (*right*: 0.0 and 1.0 correspond to 75 K and 273 K respectively) for a convecting axisymmetric Enceladus, from Roberts and Nimmo 2008b). Maxwellian tidal heating is greatest at the poles and at the base of the ice shell; heating in the stagnant lid is negligible owing to the high viscosity. An additional (frictional) shallow heat source has been imposed polewards of 55°S; note that this generates an abnormally large upwelling and thinned stagnant lid at the south pole

A number of hypotheses have been proposed for the relationship between tidal heat generation, heat transport, and the tiger stripes. The high brightness temperatures observed close to the tiger stripes (Spencer et al. 2006 and Fig. 21.14) led Nimmo et al. (2007) to suggest that shear heating due to cyclical strike-slip motion along fault zones within the stripes could be the dominant mode of tidal heat generation in this region. Because the SPT sits topographically lower than the surrounding terrain, Collins and Goodman (2007) suggest that the SPT is a region where the ice shell is locally thin. Tobie et al. (2008) suggest that subsurface tidal dissipation focused within the SPT causes melting within the ice shell, leading to subsidence. Conversely, in the Nimmo et al. (2007) scenario, frictional heating on faults within the tiger stripes is currently the dominant mode of tidal dissipation in the region. If shear heating occurs in an ice shell that is convecting, convective upwellings are "drawn to" the fault zones, resulting in locally enhanced heat fluxes and a thinned stagnant lid (Roberts and Nimmo 2008b, see Fig. 21.4). The interaction between shear heating and convection is an active area of research in the context of Europa's double ridges (Han and Showman 2008): similar efforts for Enceladus could provide insight into the modes of heat generation and transport within the SPT.

21.2.6 Evolution Through Time

The thermal evolution of satellites is much more complicated than that of their planetary cousins because tidal heating, which can show large temporal variability, provides the main satellite heat source. Dissipation in a satellite depends on the mechanical (and thus thermal) structure of the satellite, and causes the orbital eccentricity to decrease, while dissipation in the primary increases the satellite semi-major axis (e.g., Dermott et al. 1988). Changing the satellite eccentricity changes the tidal heating and thus the thermal structure; as the thermal structure changes, so does the dissipation, and so on. Orbital and thermal evolution are thus intimately coupled (Ojakangas and Stevenson 1986, Showman et al. 1997, Hussman and Spohn 2004). In the case of Enceladus the eccentricity is prevented from damping out by the Enceladus:Dione 2:1 mean motion resonance.

Meyer and Wisdom (2007) recently pointed out that the present-day eccentricity of Enceladus cannot be a steady-state value. A constant eccentricity, e, implies that the increase in e driven by dissipation in Saturn and the resonance with Dione is balanced by the decrease in e driven by dissipation in the two satellites. In this steady-state case, the total dissipation in the satellites can be calculated based on the Q of Saturn, without needing to know Q or k_2 of either satellite (cf. Lissauer et al. 1984). Assuming it is frequency-independent, a lower bound on Q_{Saturn} can be derived by considering the orbital evolution of Mimas (e.g., Dermott et al. 1988). The resulting upper bound on dissipation within Enceladus is about 1.1 GW for the minimum Q_{Saturn} of 18,000, less than the $>5.8 \pm 1.9$ GW currently observed (Spencer et al. 2006). Thus, Enceladus has an eccentricity that is not in steady state but is presumably decreasing with time, while the satellite releases energy stored at an earlier epoch.

The orbital evolution of Enceladus turns out to be complicated (Meyer and Wisdom 2008). Capture into its present-day 2:1 "e-Enceladus" resonance was probably preceded by temporary capture into several other nearby 2:1 resonances, and could only have occurred for certain values of Dione's eccentricity and k_2/Q. None of these resonances generate an eccentricity in excess of 0.007, which limits the amount of tidal heating that could have occurred in the recent past. Passage through the Mimas:Enceladus 3:2 resonance does not appear to generate eccentricities above the equilibrium value (resulting in a maximum heat flow of 0.48 GW); furthermore, there is no obvious way of escaping this resonance (Meyer and Wisdom 2008). An alternative way to generate a transient, high-eccentricity episode in the recent past might be for Janus to have passed through a 2:1 resonance with Enceladus, which was then disrupted by some unspecified process (Lissauer et al. 1984), but recent estimates of the resulting tidal heating (Meyer and Wisdom 2007) are much smaller than is observed on Enceladus.

As outlined above, it seems likely that Enceladus possesses a subsurface ocean at the present day. The lifetime of the ocean is therefore a question of considerable interest from both an astrobiological and a geophysical point of view. In particular, because tidal heating is much reduced in cases lacking an ocean, it is unclear how an initially solid Enceladus could be tidally heated enough to allow an ocean to form, unless it did so early in its history when radioactive heating was important (Schubert et al. 2007). The long-term stability of an ocean beneath tidally heated Maxwellian conductive and convective ice shells was examined by Roberts and Nimmo (2008a). These authors concluded that in both cases the removal of heat from the top of the ocean significantly exceeded the likely (radioactive) heat flow into the base of the ocean, and thus that the ocean would freeze over timescales of a few tens of Myr. Tobie et al. (2008) reached a similar conclusion, but also suggested that a local subsurface "sea" might be sustained indefinitely by melting in the overlying ice shell. The presence of antifreezing agents (e.g., ammonia) in a global ocean would delay but not halt the freezing process. Turbulent dissipation in a thin ocean might prevent it from freezing altogether (cf. Ross and Schubert 1989). Alternatively, an eccentricity three times higher than the present-day value, if it could be maintained, would allow an ocean to persist indefinitely, again strongly pointing towards an earlier epoch when Enceladus had a higher eccentricity.

The coupled thermal-orbital evolution of Enceladus has not yet been investigated in any detail. The arguments of Meyer and Wisdom (2007) suggest that either heat production within Enceladus has varied with time, or heat production has stayed constant but the heat output has varied. Ojakangas and Stevenson (1986) pointed out that Enceladus' eccentricity might undergo oscillatory behavior in a manner similar to that predicted for the Galilean satellites (cf. Hussmann and Spohn 2004), but Meyer and Wisdom (2008) have shown that such a model can't work for Enceladus because it is too small. Tobie et al. (2008) argue that tidal heating itself might result in oscillatory behavior, with Enceladus currently generating an abnormally high level of heat. These authors also argue that the putative ocean must be ancient, because in the absence of an ocean it is impossible to initiate sufficient tidal heating, as noted above. Coupling the thermal and orbital evolution of icy satellites is a challenging task that will undoubtedly form the focus of much future work.

In addition to explaining the current activity on Enceladus, any self-consistent theory has to also explain the fact that Mimas appears to be geologically inactive. If Mimas and Enceladus had the same value of Q, tidal heating in Mimas should be about 25 times stronger than in Enceladus (Squyres et al. 1983). There are two possible solutions to this problem: either Enceladus has an additional source of heat not available to Mimas; or small variations in initial conditions lead to different evolutionary paths. In the first category, Wisdom (2004) proposed that Enceladus was in a spin-orbit resonance which causes enhanced (librational) tidal heating, though as discussed above this heat source is probably not important at present. In the second category, it is well known that tidal heating can lead to softening of the interior, a decrease in Q and thus enhanced tidal heating, leading to a runaway effect: the tidal heating becomes self-sustaining if there is sufficient energy in the orbital resonance to maintain the heating. Thus, if Enceladus were initially more strongly heated than Mimas, they might have experienced different evolutionary paths (e.g., Czechowski 2006). One possibility is that Enceladus, which is presumed to have a higher rock fraction than Mimas (Thomas et al. 2007), experienced more heating due to the decay of short-lived radioisotopes such as ^{26}Al (e.g., Matson et al. 2007). While reasonable, this hypothesis is probably not unique, given that the orbital

evolution of the Saturn system was complex and likely involved various satellite resonant encounters. For short-lived radioisotopes to have initiated the currently observed tidal heating, the tidal heating must have been nearly continuous since the origin of the Saturn system, which is difficult to arrange (Meyer and Wisdom 2007).

21.2.7 Summary and Future Work

After nearly 5 years of observing Enceladus from Cassini, we are only beginning to unravel its interior structure. Given the amount of tidal and radiogenic heating Enceladus has experienced, and the present-day tidal heating rate (see Section 21.2.2.2), it seems likely that Enceladus is differentiated. Its shape indicates that its interior is probably not in hydrostatic equilibrium, which means that direct observational constraints on its internal structure from static gravity or shape data will prove difficult (Section 21.2.2.1).

The interior structure and material properties of Enceladus are very likely laterally heterogeneous, and probably include a warm upwelling region at the south pole, in which tidal heating is focused (Section 21.2.5). This upwelling may have been promoted by near-surface shear heating along the tiger stripes, and may have led to reorientation of the satellite. The magnitude of the observed heating strongly suggests the presence of either a global subsurface ocean or a regional "sea" (Sections 21.2.2.2, 21.2.4). Whether such an ocean could have survived over geological timescales depends on the history and amount of tidal heat production and is currently very much an open question.

The amount of heating observed at the south polar terrain exceeds that which can be produced by standard tidal heating models if Enceladus' eccentricity is in steady state (Section 21.2.6). Because there is no obvious alternative to the Maxwell viscoelastic tidal heating model, this result strongly suggests that the orbital and thermal evolution of Enceladus has been complex and non-monotonic.

The long-term thermal evolution of Enceladus is a major unsolved question, and will benefit from coupled thermal-orbital models in a manner similar to those developed for the Jovian satellites by Ojakangas and Stevenson (1986), Showman et al. (1997) and Hussmann and Spohn (2004). The spatial heterogeneity of Enceladus' interior structure and mechanical/rheological properties pose a challenge to current radially symmetric geodynamical and orbital models. As geodynamical models become more complex, and involve more realistic and detailed models of Enceladus' interior and material properties, more laboratory data about ice behavior and observations of Enceladus will be needed to constrain them.

The complexity of Enceladus' interior and the observations of its behavior from Cassini have sparked renewed interest in icy satellite interiors, and have suggested new areas of theoretical development and new laboratory experiments. We have been granted a unique opportunity to characterize an icy satellite during the time of its cryovolcanic activity with a well-instrumented spacecraft. Understanding the processes at work in Enceladus' interior will no doubt lead to substantial progress in our understanding of tidal heating, icy satellite resurfacing, and coupled thermal/orbital evolution.

Several arguments suggest that Enceladus is currently in an atypically warm and active state. Its current energy output is difficult to sustain over the long term. In addition, there is no geological evidence for the large change in radius implied if current mass loss rates have been maintained through Enceladus' lifetime, and ^{40}Ar is apparently being lost through the plume much faster than it is being generated by radioactive decay (Waite et al. 2009 and Section 21.5.2.4). Against these arguments must be weighed the probability of our appearing on the scene at just the right epoch to witness this unusual activity. The apparent difficulty in re-starting tidal heating in a cold and frozen Enceladus, if heating were ever to cease completely, may also place limits on how much the level of activity has varied.

21.3 Geology

21.3.1 Introduction

Voyager's highest resolution coverage (~1 km per pixel) of Enceladus provided views only of the Saturn facing hemisphere and its north polar region. That coverage was sufficient to show that Enceladus' surface morphology and geology is characterized by distinct provinces that show abrupt changes in crater densities and which are confined by major tectonic contacts. The major geological provinces identified in Voyager images are heavily cratered terrain and ridged and fractured plains. Each of these provinces can further be subdivided in terms of specific regional crater densities and complexities as well as their tectonic characteristics (Smith et al. 1982, Squyres et al. 1983, Passey 1983, Plescia and Boyce 1983, Lissauer et al. 1988, Kargel and Pozio 1996).

Cassini has now provided near-global coverage at Voyager resolution or better (Roatsch et al. 2008, Helfenstein et al. 2009). Globally, Enceladus exhibits large-scale geological and tectonic patterns that have remarkable symmetry relative to the spin axis and the Saturn/anti-Saturn direction (Porco et al. 2006, Helfenstein et al. 2009). Four broad terrain regions, with subdivisions that encompass and extend

the earlier classes, are systematically arranged relative to these directions. These are cratered plains, western hemisphere fractured plains, eastern hemisphere fractured plains, and the South Polar Terrain (SPT) province (Fig. 21.5). For detailed image maps and feature names referred to below, see Chapter 24, this book.

21.3.2 Major Terrains: Nature and Global Distribution

21.3.2.1 Cratered Plains:

A nearly continuous N-S band of heavily cratered materials wraps from the Saturn-facing side of Enceladus, over the north pole, and down the anti-Saturn side. It is interrupted only near the south pole by the SPT province. The band of cratered plains separates the tectonically resurfaced terrains on the leading and the trailing hemispheres. Kilometer and smaller scale craters in the cratered plains often exhibit bowl shapes, however almost all larger craters show varying stages of viscous relaxation (Smith et al. 1982, Passey 1983, Moore et al. 2004) with updomed floors, subdued topographic relief, and lobate or ramparted crater rims (Fig. 21.6A1, A2). The craters are all less than 40 km in diameter with topographic relief that varies from less than 100 m to about 1,000 m (Kargel and Pozio 1996). Large craters in the cratered plains are also heavily dissected by numerous fine fractures with spacing downward from kilometers to hundreds of meters (Miller et al. 2007). The degradation state of craters increases toward southern latitudes. The most extreme examples of viscously relaxed impact features occur especially near the outer boundaries of the cratered plains, such as at the northern margin of Sarandib and Dyar Planitias (near 35°N, 290°W), and adjacent to the South Polar Terrain province. Within the cratered plains, prominent orthogonal sets of N-S and E-W trending rifts occur near the sub-Saturn (0°N, 0°W) and anti-Saturn (0°N, 180°W) points. Evidence of strike-slip motion is seen on the sub-Saturn example (Kargel and Pozio 1996). Their symmetric placement relative to the tidal axis of Enceladus suggests that tidal interactions played a role in their formation (cf. Helfenstein et al. 2009).

21.3.2.2 Eastern (Trailing) Hemisphere Fractured Plains

The eastern hemisphere (centered at 270°W) is heavily resurfaced by tectonism. From equatorial to mid-northern latitudes, it is dominated by two major fractured plains regions, Sarandib Planitia (5°N, 305°W) and Diyar Planitia (5°N, 250°W). The fractured plains exhibit both negative and positive tectonic relief forms. Troughs, scarps, grooves, and pit chains reflect mainly extensional stress while ridges may indicate compressional forces (Passey 1983). Networks of kilometer-scale troughs, fractures, and ridges further subdivide these plains into crudely polygonal sections, each of which is several tens of kilometers across. These polygonal subsections exhibit varied fracturing styles, although commonly the fractures and ridges within a given polygon form a parallel fabric that may differ in orientation from those in adjacent polygons. In the northern parts of Sarandib and Diyar, terrains are mostly made up of striated & ridged plains (Kargel and Pozio 1996) and relatively smooth plains (cf. Passey 1983). The striated & ridged plains are bounded against the cratered plains by ridged & grooved materials; Harran Sulcus in the North and East, and Samarkand Sulcus on the West side. Also within the fractured terrains are flow-like features resembling glacier surfaces or pasty cryovolcanic deposits (Smith et al. 1982, Squyres et al. 1983, Kargel and Pozio 1996, Kargel 2006, Porco et al. 2006).

Sarandib Planitia and Diyar Planitia are separated in the north by a peculiar polygonal system of rounded narrow ridges called dorsa, and elongate domes, all of which appear to have been extruded from pre-existing fractures. The most prominent examples Ebony Dorsum and Cufa Dorsa (Fig. 21.6, C1), were visible in Voyager images (Smith et al. 1982). At the highest Cassini ISS resolution of this area (65 m per pixel), the features are crosscut by sub-kilometer scale parallel cracks that seem to cover the entire surface of Enceladus (Miller et al. 2007). The only other Eastern hemisphere ridge structure of comparable relief is a 120 km long, N-S trending ridge at the southern end of Samarkand Sulcus along the western edge of Sarandib Planitia. The Samarkand Sulcus ridge is morphologically distinct from the dorsa: It appears to be a compressional feature composed of angular, tilted icy slabs that are stacked en echelon as chevron-shaped cuestas that dip southward at shallow angles. Their morphology suggests that the Sarandib ridge is a compressional feature, most likely a thrust (Kargel and Pozio 1996, Helfenstein et al. 2009).

At about 15°S, a distinct south-facing scarp marks an abrupt southward transition from the equatorial and northern fractured plains units to the eastern hemisphere reticulated plains (Helfenstein et al. 2009). Reticulated plains are characterized by a complex network of crosscutting fractures that contain at least two recognizable superposed fracture patterns of generally different stratigraphic age. The base tectonic fabric is a stratigraphically old pattern of curvilinear fractures that generally intersect at acute angles and divide the terrain into lenticular mesas and hills. Superposed on this pattern is a system of quasi-parallel bands that cut the preexisting terrain into lanes along which lateral shear displacements are sometimes evident. In the eastern hemisphere, the reticulated terrain is overprinted with sparse impact craters

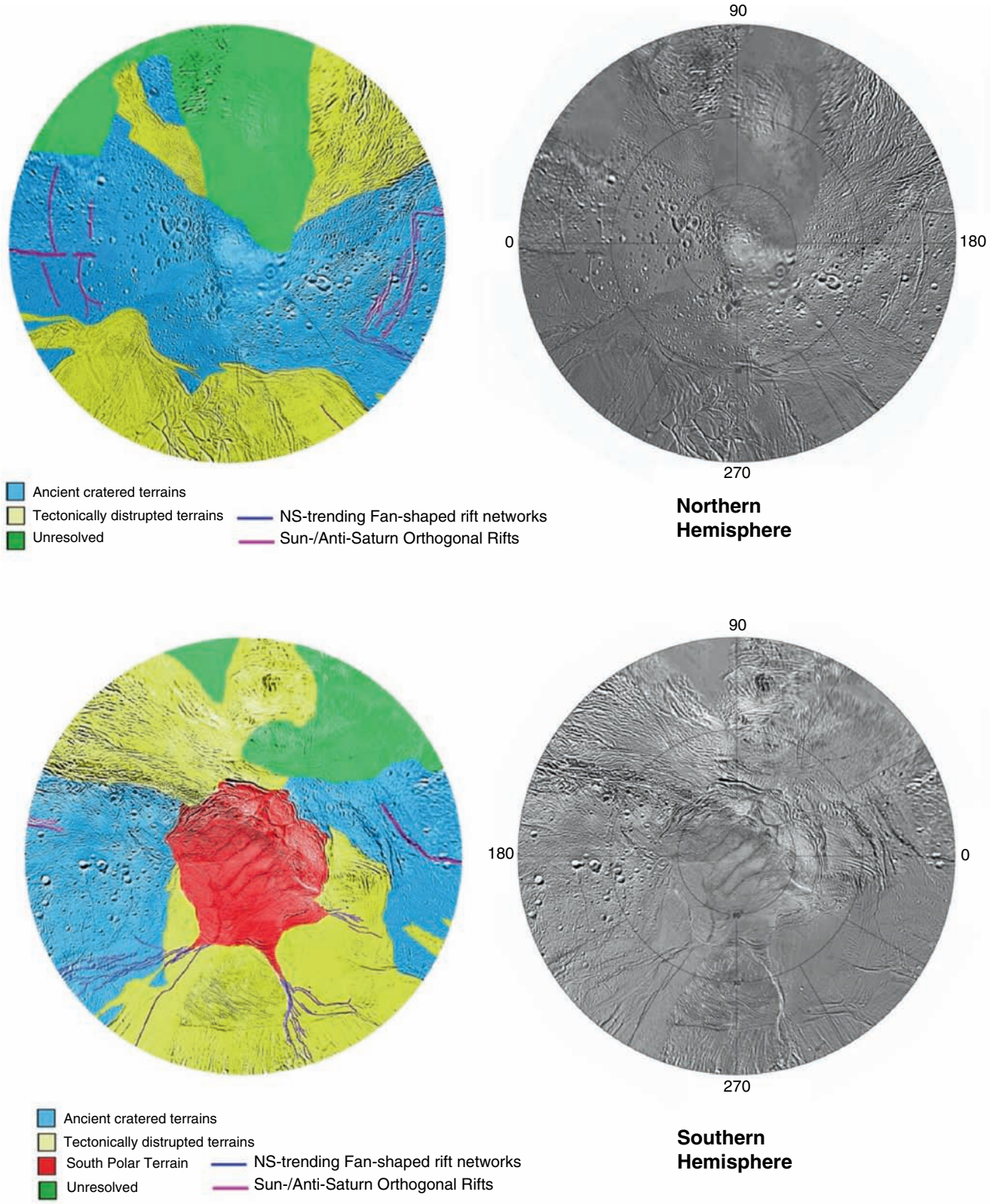

Fig. 21.5 Simplified geological unit map of the southern hemisphere (*bottom*) and northern hemisphere (*top*), respectively, showing principal terrain subdivisions and prominent tectonic patterns. Colored unit maps at left are keyed to the corresponding grayscale basemaps at right. Longitude 0 points towards Saturn. See text for discussion

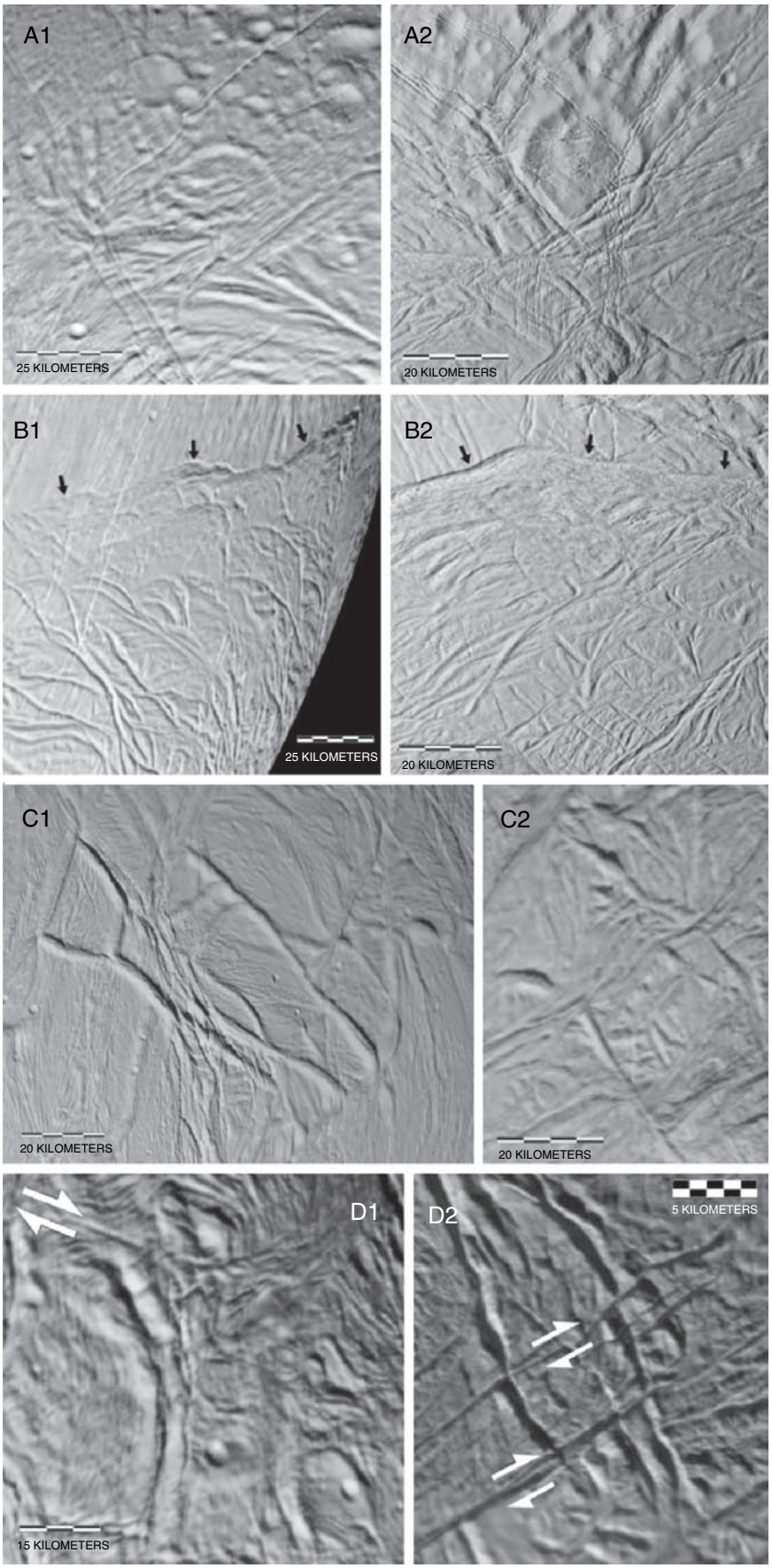

Fig. 21.6 Comparison of proposed relict SPT-style features in Enceladus' eastern hemisphere with SPT examples (Helfenstein et al. 2009). A1-A2 shows highly relaxed, laterally deformed craters that suggest that regions bounding Sarandib Planitia (A1 at 38°N, 316°W) and the SPT (A2 at 50°S, 177°W) have undergone very similar thermal histories and margin deformation. B1-B2 compares (B1) the south facing scarp and enclosed reticulated plains (near 255°W, 15°S) in the eastern hemisphere with (B2) a similar bounding scarp and enclosed reticulated plains in the SPT (55°S, 200°W). C1-C2 compares the eastern hemisphere dorsum network (C1 at 5°N, 285°W) containing Ebony Dorsum and Cufa Dorsa with (C2 at 73°S, 320°W) a similar unnamed dorsa network within the south polar reticulated plains. D1-D2 compares (D2 at 76°S, 0°W) morphologically degraded relict tiger stripe features at the end of Damascus Sulcus with (D1 at 20°N, 277°W) a morphologically similar example in the Eastern hemisphere within Diyar Planitia. Arrows in D1-D2 identify right-lateral strike-slip offsets

that have diameters up to about 10 km. The eastern hemisphere reticulated terrain is bounded in the south by the South Polar Terrain margin (see below and Fig. 21.5).

21.3.2.3 Western (Leading) Hemisphere Fractured Plains

While the eastern hemisphere of Enceladus has been imaged at kilometer-scale resolution or better by both Voyager and Cassini spacecraft, at present only about 30% of the western hemisphere (centered at 90°W) has been covered at this resolution. Coverage is sufficient to show that, as in the eastern hemisphere, large areas of the western hemisphere have been modified by fracturing and tectonism. However, unlike in the eastern hemisphere, tectonic resurfacing of the western hemisphere may not have eradicated all evidence of early large impact craters. Figure 21.5 shows that, in the western hemisphere, the edge of the near-global N-S band of cratered plains borders against fractured plains. To the extent that they can currently be identified, the fractured plains are ridged & grooved materials, generally trending N-S where they are closest to cratered plains, transitioning to E-W near the boundary with north polar cratered plains and the south polar Terrain boundary.

In spite of widespread fracturing, the remnants of the early geological history of the western hemisphere may possibly remain. Figure 21.7A shows possible highly relaxed ancient impact features (palimpsests). While there is some evidence for overprinting by fractures, the features, if they are indeed palimpsests, are relatively undistorted by widespread tectonism. Other large, possible relict impact craters are shown Fig. 21.7B, where arcuate patterns of narrow ridges outline a cluster of large quasi-circular features. These are perhaps the buried or thermally eroded rims of large ancient impact craters. If these are impact features, they are larger in diameter by a factor of two or more than any unambiguously identified impact crater on Enceladus. In that case the western hemisphere would preserve some of the oldest terrain on Enceladus. The high state of thermal degradation of the possible palimpsests in the western hemisphere is evidence that this region, like the eastern hemisphere and SPT, may have evolved through a period of elevated thermal flux (Bland et al. 2007, Giese et al. 2008).

21.3.2.4 South Polar Terrain (SPT)

The SPT province is a geologically active region centered on the south pole (Porco et al. 2006). It is bounded at about 55°S latitude by a prominent circumpolar chain of south-facing arcuate scarps and confined mountain chains, from which a series of N-S trending fractures and rifts extend toward the equator (Figs. 21.1, 21.5, and 21.8, see also Porco et al. 2006, Fig. 2A). These fractures crosscut all other terrains in their path and are thus stratigraphically youthful

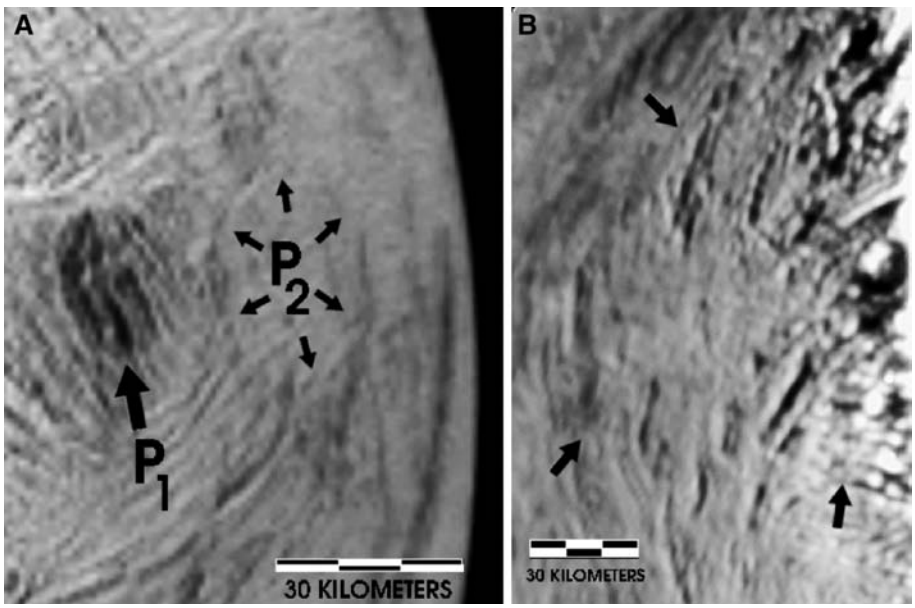

Fig. 21.7 Possible palimpsests in the western hemisphere of Enceladus. (**A**) Portion of ISS NAC image N1489087056 that shows a possible dark palimpsest (P_1, 11°N, 79°W) and adjacent bright palimpsest (P_2, 15°S, 70°W). The dark palimpsest possibly the darkest feature on the surface of Enceladus. Its albedo contrast with the surrounding brighter terrain is about 40%. North is up. (**B**) Portion of Cassini ISS NAC image N1485423252 that shows an array of arcuate ridges that appear to outline relict crater rims (*arrows*) near 18°N, 140°W. The phase angle is 105° and north is 15° counter clockwise from up (Helfenstein et al. 2009)

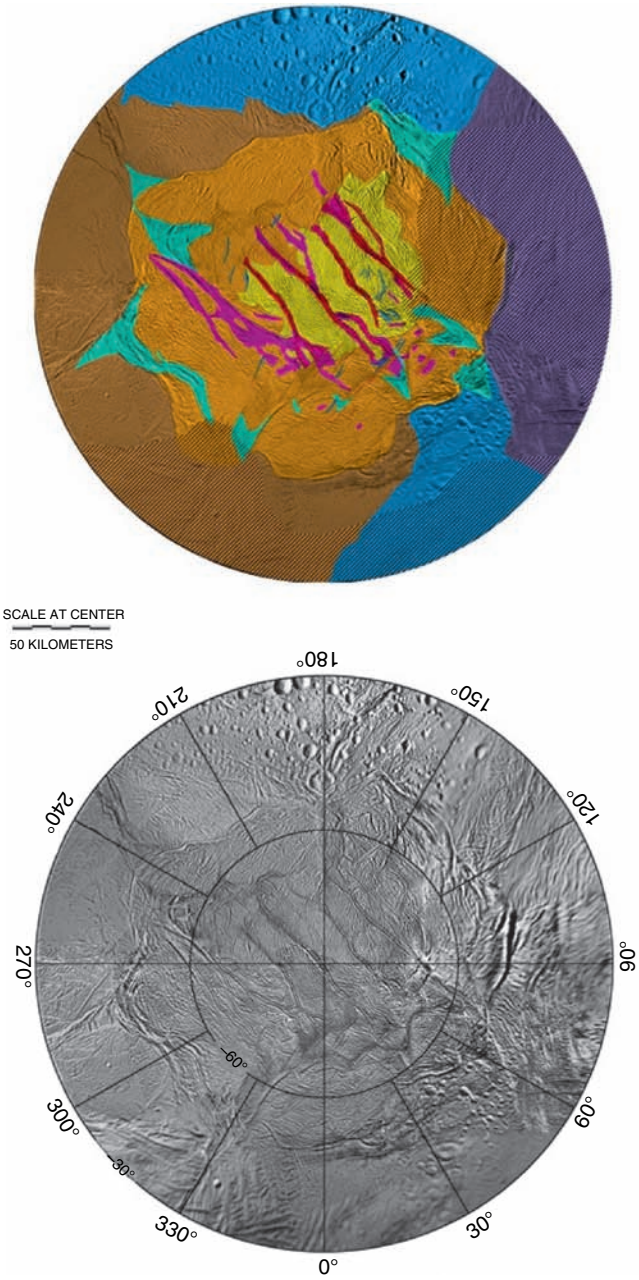

Table 21.2 Enceladus South Polar Terrain Units (Fig. 21.8)

	Tiger stripe smooth flank formation
	Tiger stripe platy flank formation
	Tiger stripe medial dorsum structure
	Relict tiger stripe structure
	South polar funiscular plains
	South polar lateral fold-and-wedge formation
	Dorsum
	South polar reticulated plains
	Eastern hemisphere reticulated plains
	Shear zone
	Western hemisphere fractured plains
	Cratered plains
	Uncertain due to inadequate imaging

Fig. 21.8 Preliminary South Polar Terrain unit map (*top*) and the corresponding ISS clear-filter photomosaic map (*bottom*) (Helfenstein et al. 2009). The legend is given in Table 21.2. The polar stereographic projection is centered on the south pole with latitude range in 30° increments from 30°S to 90°S with west longitudes given. Diagonally hashed sections delineate areas where the classification is tentative due to inadequate imaging

(Porco et al. 2006). Topographic measurements from Cassini images (Helfenstein et al. 2009) indicate that the central portion of the SPT region is topographically depressed by 500 m or more relative to the mean elevation, consistent with recent determinations of Enceladus' global figure (Thomas et al. 2007).

The terrain features within the SPT province are complex and varied (Fig. 21.8). In addition to the marginal arcuate scarps and mountain ranges, they include a series of four prominent parallel rifts, informally called tiger stripes (Porco et al. 2006) from which plumes of water vapor (Hansen et al. 2008) and icy particles (Spitale and Porco 2007) are erupting; a network of quasi-parallel ropy ridges, or funiscular plains, between the tiger stripes; and surrounding the tiger stripes, an outer circumpolar ring of chaotic, highly fractured south polar reticulated plains.

Along more than half the perimeter of the SPT margin, between longitudes 110°W to 320°W, the arcuate scarps that bound the SPT exhibit convex faces that uniformly point southward, and at longitudes where the arcs border cratered plains to the north, they intersect to form cusp-shaped "kinks" that crudely resemble the dihedral cusps of intersecting terrestrial island arc systems (Porco et al. 2006). Along much of the remainder of the SPT boundary, the arcuate scarps are concave southward and the dihedral cusps point toward rather than away from the SPT region (Helfenstein et al. 2009). The circumpolar boundary has been interpreted as a convergent tectonic boundary that formed in response to compressive stresses oriented N-S (Porco et al. 2006, Helfenstein et al. 2009). At longitudes where convex, south facing arcuate scarps bound pre-existing eastern hemisphere reticulated terrains to the north, they do not intersect in a sharp cusp. Instead, they bend northward through about 90° in azimuth to form the parallel, tapered ends of Y-shaped discontinuities (Porco et al. 2006) that interrupt the otherwise continuous circumpolar outline. The Y-shaped discontinuities transition northward into sub-parallel N-S trending rifts and cracks (Figs. 21.1, 21.5, and 21.8). The cracks are most closely spaced at the tapered end of the Y-shaped discontinuities from which they emerge and progressively fan-out as

they propagate toward equatorial latitudes and often merge with major N-S rift systems, e.g., Labtayt Sulci and Lahej Sulci that, near the equator, are each parallel to a stratigraphically old system of ridges and grooves. A south-trending rift system from Anbar Sulcus merges with cracks that extend north from another Y-shaped discontinuity.

Prominent icy mountain ranges with hundreds of meters of relief occur just within the SPT margin (Porco et al. 2006, Gioia et al. 2007, Helfenstein et al. 2009). The mountain ranges consist of curved, parallel ridges and grooves that are nested and arc together so that in plan-form they have a laterally folded appearance with the fold axis running approximately N-S. A triangular wedge-shaped prism, often topographically raised relative to flanking terrain, is usually present at the crest of the fold shape. On the eastern hemisphere side of the SPT, these Lateral Fold-and-Wedge structures penetrate the SPT margin scarps into the bordering eastern hemisphere reticulated terrains. The mountain belts are particularly well developed on the eastern hemisphere side of the SPT region, and especially when they are adjacent to or confined by the southward-facing openings of Y-shaped discontinuities. There, in plan form the lateral folds generally bend northward such that the horizontal fold axis is in line with the discontinuity's axis of symmetry. The Lateral Fold-and-Wedge structures are interpreted as thrust belts (Helfenstein et al. 2009). The icy thrust wedges evidently focus stresses at the tapered end of the Y-shaped discontinuities and appear to cleave apart the already highly cracked reticulated terrain and initiate a fan of north-going tension cracks from the wedge tip, where crack-tip propagation stresses are most focused (Gioia et al. 2007, Helfenstein et al. 2009). The Y-shaped discontinuities appear to be more evolved examples of the dihedral margin cusps. Helfenstein et al. (2009) propose that the Y-shaped discontinuities can penetrate through reticulated plains, but not cratered plains because the highly fractured reticulated terrains are mechanically weaker than the cratered plains lithosphere and that reactivation of the many reticulated terrain fractures allow the lithosphere to deform on a large scale in a pseudo-ductile behavior.

The thinnest region of Enceladus' lithosphere may be right at the South Pole where the tiger stripes could extend to the depth of a volatile reservoir of liquid water (Collins and Goodman 2007, Manga and Wang 2007) or clathrate (Kieffer et al. 2006). Currently published estimates of this thickness vary: Roberts and Nimmo (2008b) give a minimum thickness of 5 km based on modeling of shear heating along tiger stripes, while Gioia et al. (2007) postulate that tiger stripe fractures penetrate a 35 km thick lithosphere equivalent to the mean spacing between them, and Rudolph and Manga (2009) calculate that complete cracking is of the crust is possible if it is less than 25 km thick.

21.3.2.5 Tiger Stripes

As described by Porco et al. (2006), the tiger stripes are linear depressions or cracks, typically about 500 m deep, 2 km wide and 130 km in length. They are flanked on both sides by 100-m-high ridges. The four major tiger stripes (Alexandria, Cairo, Baghdad, and Damascus Sulci) are sequentially arranged in a right lateral en echelon placement across the south polar region (Helfenstein et al. 2009), suggesting that the tiger stripes and south polar region have evolved through a regional system of right-lateral shear parallel to the trends of the tiger stripes. The tiger stripes are known sources of thermal emission (Spencer et al. 2006 and Fig. 21.14) and plume jets (Spitale and Porco 2007). Cassini obtained high-resolution (as fine as 7 m per pixel) images of most of the known jet vents during two close flybys of Enceladus in August and October 2008. These have been mapped by Helfenstein et al. 2009 (e.g., Fig. 21.9).

All of the known active portions of the tiger stripes are covered with smooth deposits identified as Smooth Flank Formations. These smooth deposits also extend along most of the lengths of the tiger stripes. These deposits appear to drape over the raised flanks and valley walls of tiger stripes and extend laterally outward to surrounding terrains, where they gradually thin out, especially toward the ends of the tiger stripes. The summits and outer limbs of raised flanks have a smoothly undulating texture, suggesting that they are mantled with a particulate blanket. They are overlain by numerous ice blocks up to tens of meters in size. Smooth Flank Formations along the walls of the tiger stripe rifts are often striated, perhaps from the down slope movement of icy blocks or from scouring by plume jets.

The appearance, shape, and surface texture of long inactive tiger stripe flanks are subtly different from the active regions. Platy Flank Formations are noticeably less covered by smooth mantling material than Smooth Flank Formations. They can be distinguished by the presence of visible small cracks and the dissection of the exposed surface into small slabs or plates that are absent on active tiger stripes. On multi-kilometer scales, Platy Tiger Stripe Formations develop gradual lengthwise topographic undulations along tiger stripe flanks, with lobate margins, and partial segmentation of the flanks into parallel chains of rounded connected hills.

Relict Tiger Stripe materials represent more evolved degradational states of the aforementioned tiger stripe formations. They cover a range of rift structures with raised smooth or segmented parallel flanks and they have a similar scale, branching structure, width dimensions, and sometimes trend parallel to or extend from other Tiger Stripe formations. They can occur as long smooth-appearing parallel ridges that are similar in appearance, but often wider with more muted

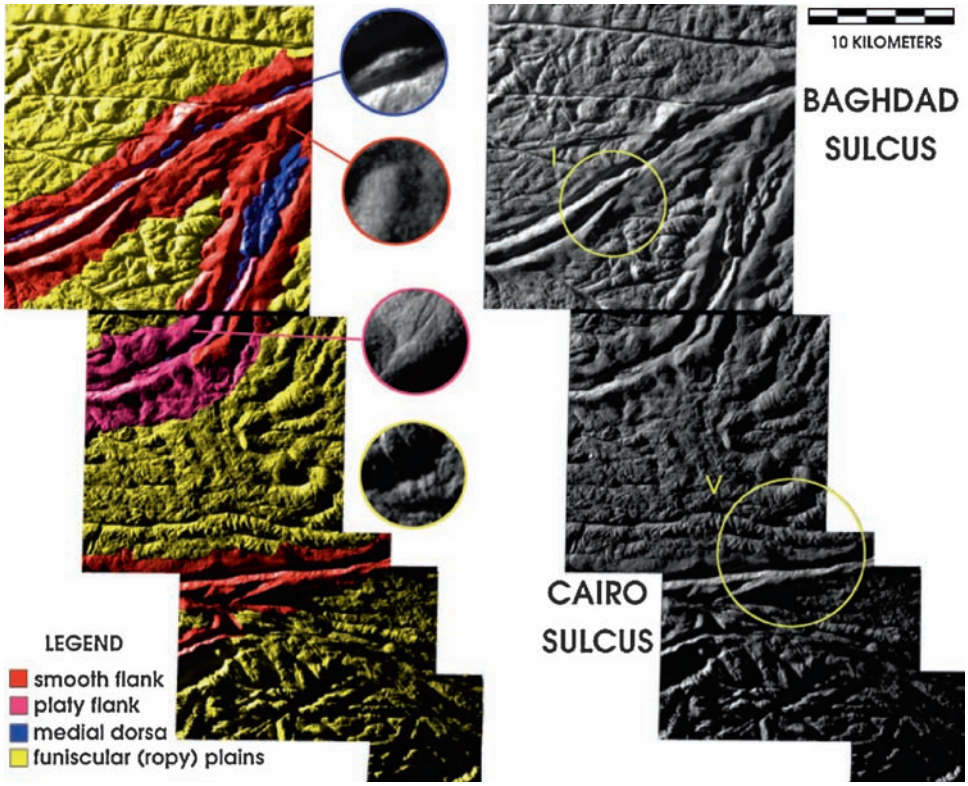

Fig. 21.9 High-resolution local terrain unit map (*left*) and corresponding photomosaic (*right*) of parts of Cairo and Baghdad Sulci, from Cassini's August 11, 2008 flyby (Helfenstein et al. 2009). Terrain unit maps are keyed to the legend in Table 21.2. Insets show textural and structure details that help define the units (see text). Yellow circles labeled with Roman numerals I and V correspond to erupting jet sources (Spitale and Porco 2007)

topography and higher albedos than the smooth tiger stripe formations. They appear to be extinct or dormant tiger stripes that have accumulated a coating of icy, probably particulate, regolith material over time.

The high-resolution ISS images reveal narrow ridges and elongated domes within the tiger stripe valleys. Helfenstein et al. (2009) class these features as Tiger Stripe Medial Dorsum Structures: They are narrow (~100 m wide) lenticular or sinuous ridges, or clustered collinear or parallel formations of such ridges, that rise tens to hundreds of meters from within a tiger stripe valley. Solitary examples have a distinct free-standing dorsal fin like shape, and are informally called "shark fins". They may also appear as irregular masses of oblate, smoothly rounded hills. They are interpreted as transpressional ridges that are extruded from the tiger stripe rifts, perhaps as a result of cyclic tidal flexing (cf. Hurford et al. 2007, Helfenstein et al. 2009). As such, their presence lends support for recent theories that invoke shear-heating along tiger stripes as a mechanism for generating plume jets (Nimmo et al. 2007, Smith-Konter and Pappalardo 2008). Free-standing dorsa occur throughout the SPT region, as polygonal networks (Fig. 21.6D) and also along strike-slip faults, restraining bends, and shear zones (Fig. 21.8). Their frequent association with shear zones implies that, like tiger stripe medial dorsa, they are transpressional features that have been extruded from faults.

Between the tiger stripes are curved, quasi-parallel knobby ridges and clustered arrangements of elongated barrel-shaped knobs (Fig. 21.9), classified as funiscular (i.e., ropy) plains by Helfenstein et al. (2009). They were first recognized as "grooved bands" by Porco et al. (2006) and trend approximately parallel to tiger stripes. Their lengths and kilometer-scale widths are comparable to those nearby tiger stripe flanks. On scales of tens to hundreds of meters, they have a broken, platy surface texture. They are often finely dissected by thin parallel cracks spaced tens of meters apart and less. Near their distal ends where funiscular plains intersperse and grade into south polar reticulated terrain (see below) they appear to break into a more chaotic arrangement of knobs and cylindrical segments. Color ISS and VIMS data show that the funiscular plains are generally covered with more fine-grained ice than the tiger stripes themselves (Brown et al. 2006, Porco et al. 2006, Jaumann et al. 2008).

Surrounding the tiger stripes and funiscular plains is an approximately 50 km wide annulus of South Polar Reticulated Plains (see also Gioia et al. 2007, Helfenstein et al. 2009). This terrain unit is broadly similar to eastern

hemisphere reticulated plains material and likely represents a stratigraphically younger South Polar extension of that terrain. It is characterized by at least two superposed fracture patterns of generally different age, as determined by cross-cutting relationships. The base unit is a tectonic fabric of old curvilinear fractures that usually intersect at acute angles and divide the terrain into lenticular mesas and hills. The terrain is further divided by a system of quasi-parallel bands that cut the pre-existing terrain into lanes along which lateral shear displacements sometimes are evident. This unit is morphologically distinguished from eastern hemisphere reticulated plains by its near-absence of recognizable kilometer sized or larger impact craters and by the frequent occurrence of isolated polygonal islands of recognizable Relict Tiger Stripe material within it. Among the most significant mechanical roles that this annulus of reticulated terrain may play in SPT tectonism is that, like its eastern hemisphere counterpart, it is highly fractured, apparently mechanically weak and can likely deform easily in response to regional stresses. Because it surrounds the tiger stripes and funiscular terrain, it may act to partially decouple deformations of the central polar cap from those near the SPT margin (Helfenstein et al. 2009).

21.3.3 Surface Age Distribution Through Crater Counting

Crater counts on Enceladus confirm the wide range of surface ages (Plescia and Boyce 1983, Lissauer et al. 1988, Kargel and Pozio 1996, Porco et al. 2006). Depending on the flux model used, which can be either lunar-like and therefore asteroidal (Neukum 1985) or, more plausibly, based on models of cometary impact rates (Zahnle et al. 2003), cratered plains materials have absolute ages as old as 4.2 billion or 1.7 billion years, respectively. In general, the eastern fractured terrain has formed either between 3.7 and 1.0 billion years ago in the lunar-like scenario or it is as young as 200–10 million years based on the Zahnle et al. model. The south polar terrain shows crater ages younger than 100 million to few hundreds of thousands years, respectively, consistent with the ongoing activity at the tiger stripes.

21.3.4 Global Tectonics and Possible Rotational Changes

The newly recognized, remarkably simple global symmetry and systematic placement of terrain provinces on Enceladus have inspired different theories about the large scale mechanisms that have produced them. Among the first hypotheses to emerge (Porco et al. 2006) was that a simple uniaxial global deformation mechanism might be responsible for the circumpolar SPT boundary at about 55°S with attendant N-S tension cracks that extend to the equator. Increased flattening of the rotational axis was proposed, as would be predicted from an increased spin rate (perhaps as a result of a large, suitably oriented impact) or some global deformation mechanism that mimics the hemispheric deformation effects of spin-up (like the melting of a subsurface sea at the South Pole (Collins and Goodman 2007)). To first order, this single mechanism appears to account for the circumpolar location and orientation of the SPT boundary if it is interpreted entirely as a convergent tectonic margin (evidenced by convex-southward arc-and-cusp scarp and thrust-faults associated with N-S lateral fold-and-wedge features). However, this simple hypothesis fails to explain the tiger stripes as a system of parallel tension cracks at the South Pole and it does not account for the absence of an SPT type province at the North Pole. Separate mechanisms for the origin of tiger stripes and the hemispheric north–south asymmetry are thus needed to amend this hypothesis. The model also ignored changes in the tidal figure of Enceladus.

Matsuyama and Nimmo (2008) present a more complete global deformation model that considers changes in the triaxial tidal figure that would accompany increased spin rate. In their refined model, the zone of polar thrust faulting begins poleward of about $\pm 70°$ latitude, 15° closer to the South Pole than the SPT margin. To extend the thrust zone to SPT boundary latitudes, a decrease in internal volume of Enceladus would need to accompany the increase in spin rate. Matsuyama and Nimmo also show that, if Enceladus fractures always form by shear failure, strike-slips faults that are inclined relative to lines of latitude and longitude are predicted to occur closer to the equator, contrary to observation, except for regions that surround the sub-Saturn and anti-Saturn points on the surface where N-S trending normal faults are predicted. Consequently, simple uniaxial deformation about the spin axis is insufficient to account for the observed arrangement of SPT tectonic features. And of course, stress patterns from changes in spin rate and orientation are always symmetric between the north and south hemispheres, so additional mechanisms are required to explain the hemispheric asymmetry.

Gioia et al. (2007) propose a model in which thermotectonic stresses arise from a postulated deep-seated hot thermal anomaly under south polar cap. The thermal expansion of warm materials under their "Tiger Stripe Terrain" or TST (corresponding to tiger stripes, funiscular plains, and adjoining portions of the south polar reticulated plains in Fig. 21.9) causes lateral tension throughout the central south polar cap occupied by tiger stripes. Toward the SPT boundary, horizontal radial stresses transition to compression, while hoop

stresses parallel to lines of latitude remain tensile. Gioia et al. note that the TST region is not circular, but somewhat rectangular in shape. If a 210 × 148 km rectangular shape is chosen for the thermal anomaly, with the longest side approximately matching the length and orientation of the tiger stripes, then the resulting azimuthal variations in horizontal TST tensile stresses predict the formation of tiger stripes as tension cracks or normal faults with the observed orientation. At the same time, horizontal radial stresses near the SPT become preferentially more compressive parallel to the tiger stripes. Finally, if the depth of the lithosphere and thickness of the thermal anomaly is chosen to be about 35 km, then the model predicts to first order a reasonable match for the spacing of dihedral cusps along the SPT bounding scarps and the mean spacing of the tiger stripes.

The Gioia et al. model is interesting especially because it invokes a single mechanism to predict the placement and orientation of the SPT boundary, the fold-and-wedge structures, and the tiger stripes. However, the model requires additional development: It treats the SPT region as a flat plate rather than realistically as a curved thick shell, it ignores temperature-dependent rheological behaviour of deep seated warm materials, and it postulates post hoc the existence and orientation of a rectangular-shaped thermal anomaly on the basis of the current shape and orientation of the tiger stripes and adjacent terrains.

As described in earlier sections, Nimmo and Pappalardo (2006) propose that the current placement of South Polar volcanism and active tectonism is a result of global reorientation of a warm diapir from a different southern latitude closer to the equator. Collins and Goodman (2007) further suggest that such a reorientation could also be caused by the melting of a subsurface sea. Matsuyama and Nimmo (2008) find that the global deformation model which most easily explains the observed placement and orientations of the SPT boundary involves approximately 90° of true polar wander about an almost stationary tidal axis. That is, the paleo-South Pole and paleo-tidal axis would have been located at (2°N, 270°W) and (4°S, 0°W), respectively. An additional small amount of global dilatation is needed to place circumpolar thrust faults at their currently observed latitude of about 55°S, but the model otherwise accounts for the SPT boundary and the N-S tension cracks closer to the equator. As in the rotational spin-up model, polar thrust faults are predicted to occur in the SPT region and thus a separate mechanism such as diurnal tidal flexure (Porco et al. 2006, Hurford et al. 2007) must be invoked to account for the presence and orientation of tiger stripes as tension cracks.

Two independent lines of geological evidence from the analysis of Cassini ISS images reinforce a polar wander mechanism for the origin of the SPT and the evolution of fractured plains on the eastern hemisphere. Helfenstein et al. (2009) identified a suite of tectonic features in the eastern hemisphere fractured plains that are possible analogs to SPT tectonic features, some examples of which are compared in Fig. 21.6. Their placement in Sarandib Planitia and Diyar Planita, and the spatial patterns of tectonic forces that they imply, suggest that either polar wander has occurred following a path from eastern hemisphere equatorial latitudes toward the south pole, or at least that SPT-style tectonism was once more widespread, extending to these eastern hemisphere locations and progressively dissipating over time toward the only remaining active region at the South Pole.

The second line of evidence involves the possibility that tiger stripes and the funiscular terrain are surface manifestations of lithospheric spreading (Helfenstein et al. 2009). Helfenstein et al. (2009) have recently identified transform faults perpendicular to tiger stripes and apparent lateral spreading across the funsicular terrain. Preliminary reconstructions of lithospheric spreading across the tiger stripe region indicates that at least 70 km of lateral spreading has occurred from the western hemisphere side of the SPT region toward the eastern hemisphere side. This would be most easily accomplished by the presence of a buried warm diapir or subsurface sea, or both.

21.4 The Surface: Composition and Processes

21.4.1 Surface Composition

21.4.1.1 Water Ice, and Its Spatial Variability

Near infrared spectroscopy reveals that Enceladus' surface is almost completely dominated by water ice, which is mainly in a crystalline state (Cruikshank 1980, Grundy et al. 1999, Cruikshank et al. 2005, Emery et al. 2005, Verbiscer et al. 2006, Brown et al. 2006, Jaumann et al. 2008, Newman et al. 2008, Fig. 21.10).

H_2O band depths are sensitive to the abundance of ice, degree of contamination by other materials, and the particle sizes of the H_2O-ice grains (Clark 1981, Clark and Lucey 1984). Ice temperature is also important (Grundy et al. 1999). Given that water ice dominates the surface composition (Brown et al. 2006, Newman et al. 2008) spectral variations are mainly due to differences in particle sizes, with increasing absorption band depth indicating increasing particle size according to a simple power law (Jaumann et al. 2008). Global grain size variations are seen in ground-based near-IR spectra, which find somewhat stronger absorptions, implying larger grain sizes, on the leading hemisphere than on the trailing hemisphere (Verbiscer et al. 2006). VIMS data provide more detail on spatial variability, and

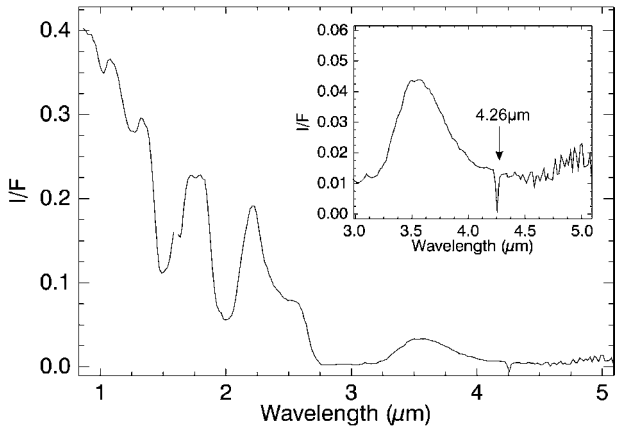

Fig. 21.10 VIMS spectrum of Enceladus' south polar region. The absorptions at 1.04 μm, 1.25 μm, 1.5 μm, 1.65 μm, 2.0 μm, and the Fresnel peak at 3.1 μm (see small *inset*) indicate almost pure water ice, with an additional strong CO_2 absorption at 4.26 μm (Brown et al. 2006)

show significant spectral variations across the surface of Enceladus, particularly in the H_2O ice absorption bands (Jaumann et al. 2008, Newman et al. 2008).

The spatial resolution of VIMS image cubes is sufficient to distinguish the three major geologic units on Enceladus: heavily cratered terrain, fractured and ridged terrain and active tiger stripes at the south pole region. Variations in the main water ice absorptions at 1.04, 1.25, 1.5, and 2.0 μm indicate that on Enceladus particle size is directly correlated with geological units (Jaumann et al. 2008, and Fig. 21.11). The heavily cratered terrains exhibit a mean particle size of 15 ± 5 μm within a VIMS pixel. Local increases of particle diameters up to 30 ± 10 μm seems to be correlated either with impact craters that expose fresh material from underneath or have locally melted the water crust, or with ridges and fractures marking the transition zone to the lightly cratered plains. Icy particles in the fractured and ridged terrain peak at a size of about 30 ± 10 μm. The tectonically deformed regions exhibit particles ranging from 40 μm to about 120 μm with the largest ones (about 2% reaching values of about 0.2 mm) located close to the center of the south polar tiger stripes.

Similar patterns are seen in the ISS multispectral images of the south polar region, which show enhanced near-infrared absorption near the tiger stripes and other tectonically disrupted regions, consistent with larger grain sizes (up to 100 μm) near the tiger stripes (Porco et al. 2006). These regions of larger grain size appear blue/green in false-color ISS images (Fig. 21.1). Possible causes for the large grain sizes near the tiger stripes include preferential fallout of larger, slower, plume grains near their sources (Jaumann et al. 2008, Hedman et al. 2009, Section 21.5.2.6), or sintering and growth of grains resulting from deposition of plume gases or from the enhanced temperatures near the tiger stripes.

Disk-integrated spectra of Enceladus indicate that the water ice in the equatorial and mid- to high-latitude regions is primarily crystalline (Grundy et al. 1999, Emery et al. 2005). However, VIMS has detected locally abundant amorphous ice in the south polar region between the tiger strips, while the stripes themselves are dominated by crystalline ice (Brown et al. 2006, Newman et al. 2008). Amorphous ice can form when water condenses from a vapor at temperatures below 100 K, and it is thus possible the south polar amorphous ice results from surface condensation of plume gases. Away from the tiger stripes, south polar surface temperatures are well below 100 K (Spencer et al. 2006), so amorphous ice should be able to form and remain stable for long periods there.

21.4.1.2 Minor Constituents

Other constituents have minor abundance and are restricted to certain areas. Some telescopic spectra show a weak 2.2–2.4 μm feature tentatively ascribed to NH_3 absorption (Grundy et al. 1999, Emery et al. 2005, Fig. 21.12), though the match is not perfect, and other spectra do not show this feature (Cruikshank et al. 2005). Spectral modeling of earth-based observations by Verbiscer et al. (2006) suggest the possibility of modest concentrations (~1%), of ammonia hydrate ($NH_3 \cdot 2\,H_2O$) on both hemispheres, though no specific ammonia hydrate spectral features were identified. No features compatible with NH_3 absorptions have been detected VIMS data of Enceladus, indicating an upper limit to NH_3 content on the surface of no more than 2% (Brown et al. 2006). H_2O_2 has been tentatively identified in VIMS spectra, via a weak 3.5 μm absorption feature (Newman et al. 2007). The wavelength of the feature varies slightly with terrain type, perhaps due to varying crystallinity of the H_2O_2 or the surrounding H_2O.

Another constituent found in VIMS spectra at 4.26 μm is CO_2-ice, seen in small amounts on a global scale and in higher concentrations near the south pole (Fig. 21.10, Brown et al. 2006). Near the tiger stripes, CO_2 is highly abundant but the band position indicates that it is not in the form of free CO_2 ice. Instead, it is complexed, probably with water ice. Small amounts of free CO_2 ice are seen elsewhere on the satellite. The lack of free CO_2 ice near the tiger stripes may be due to the higher temperatures in this area (Spencer et al. 2006), which would cause free CO_2-ice to rapidly migrate northward to colder temperatures (Brown et al. 2006). The high concentration of complexed CO_2 in the tiger stripes

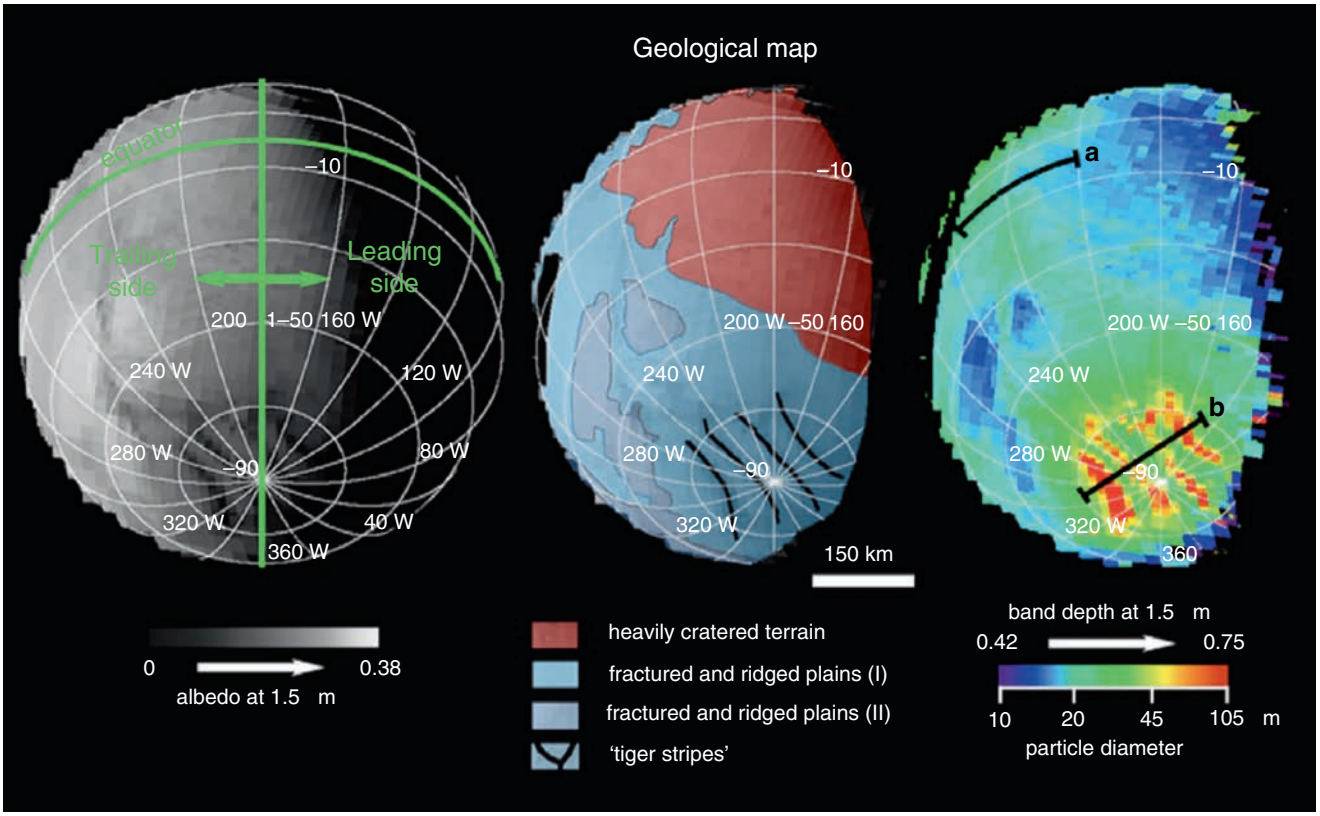

Fig. 21.11 VIMS cube image of the southern hemisphere of Enceladus, from orbit 11, with resolution <30 km per pixel. Left: albedo at 1.5 μm; middle: geologic map; right: absorption band depth at 1.5 μm indicating increasing particle diameters from blue to red. From Jaumann et al. (2008)

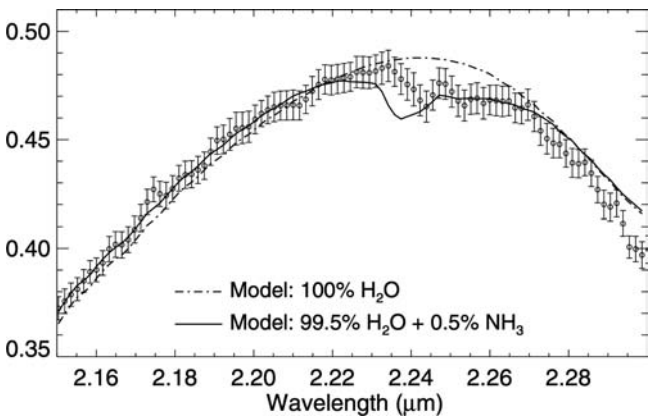

Fig. 21.12 A portion of a disk-integrated ground-based spectrum of Enceladus' trailing side, with central longitude 320 W, from Emery et al. (2005), showing a feature at 2.25 μm possibly due to NH_3 ice or ammonia hydrate. Emery et al. suggest that the wavelength shift of the band relative to the model might be due to complexing of NH_3 with water ice

may result from active replenishment by cryovolcanic activity in this area (Brown et al. 2006). No signature of CO in ice, gas, clathrate, or any other physical form is detected on the surface (Brown et al. 2006). However, VIMS spectra show 3.44 and 3.53 μm C-H stretch features near the tiger stripes, indicating simple organics in the south polar tectonic features (Brown et al. 2006). Hydrated salts or acids, such as those found on Europa (McCord et al. 1998), which might be indicative of surface materials derived from a salt-rich ocean in contact with the silicate core, have not been detected on the surface so far.

The surface composition of Enceladus, dominated by H_2O with small quantities of CO_2, and simple organics near the tiger stripes, and possible NH_3, is quite similar to that of the plume gases (Section 21.5.2.4), consistent with the possibility that much of the surface is coated by plume fallout.

21.4.2 Surface Processes

Surface modification processes on the icy Saturnian satellites include charged particle bombardment (implantation or sputtering), E-ring grain bombardment or coating, thermal processing, UV photolysis, and micrometeoroid bombardment. Such processes result in chemical as well as structural changes.

Models of Enceladus' surface must explain its extraordinarily high albedo, the highest of any known solar system body. Geometric albedo, including the strong opposition effect, is 1.41 at 0.55 μm (Verbiscer et al. 2005) and bolometric albedo is 0.80 (Spencer et al. 2006). The high albedo is probably due to a coating of plume particles, derived both directly from plume fallout and from re-impact of plume particles stored temporarily in the E-ring. Support for the importance of direct or indirect plume fallout comes from the observation that the geometric albedo of the inner Saturnian satellites correlates closely with the local density of the E-ring (Verbiscer et al. 2007), with both quantities peaking at Enceladus. This coating affects the reflectance spectra of the satellites, and could mask the signatures of other species: Buratti (1988) found no relationship between crater density and albedo in Voyager images of Enceladus and suggested that E-ring coating dominates any micrometeorite gardening. The visible orbital phase curve of Enceladus shows that the trailing hemisphere is ∼1.2 times brighter than the leading hemisphere (Buratti and Veverka 1984, Buratti et al. 1998), and ground-based spectra show smaller ice particles on the trailing hemisphere (Verbiscer et al. 2006): these differences may reflect hemispheric differences in Enceladus' interaction with the E-ring.

The Cassini CDA team is performing extensive modeling of Enceladus' interaction with the E-ring, constrained by CDA's measurements of the dust population (e.g., Spahn et al. 2006b, Kempf et al. 2008). Bombarding E-ring particles and interplanetary dust particles will both eject more dust into the E-ring, with E-ring particles greatly dominating the dust production rate (Spahn et al. 2006b). These impacts should produce an isotropic dust source for the E-ring that is in addition to, but much smaller than, the south polar plume source (Spahn et al. 2006a).

Plasma sputtering rates have been calculated recently using Cassini plasma data (Johnson et al. 2008). Water ions are the dominant sputtering agents, and rates are estimated to be about 0.1 μm year^{-1}, or 10 cm per million years, which is not insignificant.

The VIMS spectra reveal a consistent pattern of increasing grain size with decreasing surface age (Jaumann et al. 2008), as discussed above. This might be due to gradual comminution of particles over time by impact gardening or sputtering. In the south polar region, patterns of plume fallout are probably also important, with larger particles falling closer to the tiger stripe plume sources. However, it is puzzling that older surfaces, such as the lightly cratered fractured and ridged terrain and the heavily cratered terrain, have distinctive grain sizes, as their optical surfaces might be expected to be dominated by E-ring and plume fallout that is younger than either surface and would not reflect the underlying geology. Perhaps enhanced mass wasting on the rougher slopes of the younger tectonically disrupted terrain exposes fresher, coarser-grained material there.

Surface temperatures away from the active south pole probe the physical structure of the regolith by constraining the thermal inertia, and are also important for understanding the stability of volatiles and for modeling temperature-dependent spectral features. Observations by CIRS show that Enceladus has a very low average thermal inertia of 15 W m^{-2} s$^{-1/2}$ K^{-1}, which is 3–4 times lower than the Galilean satellites, though similar to the other inner Saturnian satellites, with increasing thermal inertia towards the active south pole (Spencer et al. 2006, Howett et al. 2009). A highly unconsolidated particulate surface at least a few centimeters deep is implied. Equatorial temperatures reach a peak of about 75 K at noon and drop to 50–60 K at night. At the north pole, which had been in darkness since 1995, CIRS measured an upper-limit effective temperature of 33 K during the July 2005 flyby, implying a thermal inertia of $<$100 W m^{-2} s$^{-1/2}$ K^{-1}, and thus an unconsolidated surface to a depth of at least ∼1 m (Spencer et al. 2006).

21.5 Plumes and System Interaction

21.5.1 Introduction

The Enceladus plumes are both a probe of subsurface conditions and a remarkable phenomenon in themselves. Some of the important questions regarding the plumes are: Where (at what depth) and how is the heat generated? How does it get to the surface? Is liquid water involved? What is the composition of the ice? How deep do the cracks extend? How long does each plume remain active? Potentially useful observations include: the rate of vapor and particle mass loss in the plumes; the composition of the gas; the speed of the gas; the speed, size, and composition of the particles; the total power in the plumes; the time dependence of the plumes; and the association between the plumes and surface features. We review the most significant observational evidence from Cassini instruments and ground-based sources, and then consider how modeling can help us to interpret these observations.

21.5.2 Observations

21.5.2.1 Imaging Science Subsystem (ISS)

The ISS measures the brightness of the ice grains in the plumes in spatially resolved images at wavelengths from

340 to 930 nm. The ISS images reveal the brightness of the solid particle portion of the plumes, the multiplicity of plume sources, the degree of collimation, the rate of fall-off of brightness with altitude, and the plumes source locations on the surface.

Because the plumes are optically thin, brightness at a fixed wavelength and phase angle is directly proportional to the column density $\int nds$, where n is the number of particles per unit volume and s is distance along the line of sight. The constant of proportionality depends on the cross sectional area of the particles, their albedo, and their scattering phase function. The latter governs the fraction of scattered light that goes into each direction and is a strong function of the phase angle (the sun-plume-spacecraft angle). Forward scattering is when the phase angle is close to 180°. Particles whose radius a is larger than the wavelength of light λ have a strong forward scattering lobe that narrows as λ/a decreases.

One of the highest resolution ISS images of the plume jets is shown in Fig. 21.13. The phase angle is just outside the forward scattering lobe for particles whose radius is 1.0 μm. To determine plume particle abundance, the ISS team assumed a particle size distribution with an effective radius $a = 1\,\mu\text{m}$. This is the dominant radius of particles in the E ring (e.g., Nicholson et al. 1996), which Cassini has revealed to be supplied by the Enceladus plumes. Brightness is measured in units of I/F, where I is the observed radiance in a given filter and πF is the solar irradiance in the same filter. The I/F values for the plume in this image are typically in the range 10^{-3} to 10^{-2}. With these assumptions about particle size, the ISS team estimated a column number density of $6 \times 10^8\,\text{m}^{-2}$, corresponding to mass of ice in the column of $3 \times 10^{-6}\,\text{kg m}^{-2}$. This is for a line of slight whose closest approach to Enceladus is at an altitude of 15 km and a latitude of 76°S. Comparison to the column density of vapor of $7 \times 10^{-6}\,\text{kg m}^{-2}$ reported by the UVIS instrument (Hansen et al. 2006, see Section 21.5.2.3 below) gave an ice/gas mass ratio of ~0.4. This ratio is quite uncertain because the particle size distribution is uncertain, and smaller mass ratios (ice/gas <0.1) have been derived from a recent re-analysis of the original data (Kieffer et al. 2009). The ice/gas ratio is a significant constraint on the processes that form the plumes (Section 21.5.3.2).

Plume brightness falls off with altitude more or less exponentially. The scale height within 50 km of the surface is ~30 km, which is much less than the radius of the planet, and implies that most of the particles close to the ground are falling back. The scale height is larger at higher altitudes, which means that many particles are escaping as well. The vertical fall-off fits a model in which the distribution of speeds of the particles leaving the vent is a Gaussian of the form $\exp[-(v/v_0)^2]$. The best fit gives a mean velocity $v_0/\pi^{1/2} = 60\,\text{m s}^{-1}$. This is much less than the escape speed ($235\,\text{m s}^{-1}$) and much less than the velocity of the gas molecules, $\sim(2RT)^{1/2}$, where R is the specific gas constant (the ideal gas constant divided by the gas molecular weight), of $406\,\text{m s}^{-1}$ for $T = 180\,\text{K}$ (Spencer et al. 2006), or the ~300–500 m s^{-1} speed inferred from UVIS observations (Tian et al. 2007). The inference again is that most of the particles are falling back to the surface.

Spitale and Porco (2007) use images taken over a 2-year period to triangulate the source locations for the most prominent jets and compare them with the observed hotspot locations (Spencer et al. 2006) and surface features (Fig. 21.14). The jets are located on or very close to the tiger stripes, and tend to occur near the warmest regions of the tiger stripes. These observations also show that at least some of the plume jets are persistent over the 2-year period.

Further analysis of the ISS images should yield an estimate of the phase function, and therefore the particle size, though possible temporal variability is a potential complication, since the observations at different phase angles necessarily occur at different times. The wavelength dependence of the plume brightness provides a further particle size constraint.

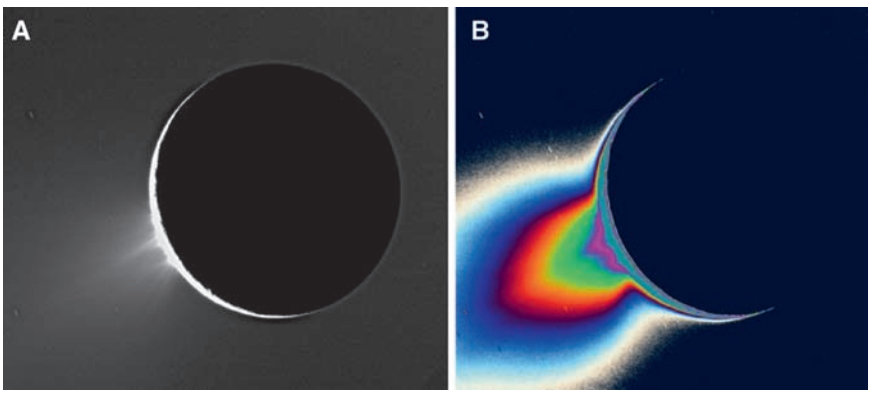

Fig. 21.13 Image of the Enceladus plumes take on November 27 2005 at a phase angle of 161.4° with a spatial resolution of 0.9 km per pixel. Individual plume jets are visible in image **A**, and image **B** has been enhanced using pseudocolor to bring out the fainter portions of the plume. From Cassini Press Releases PIA07758 and PIA07759, NASA/JPL/SSI, and Porco et al. (2006)

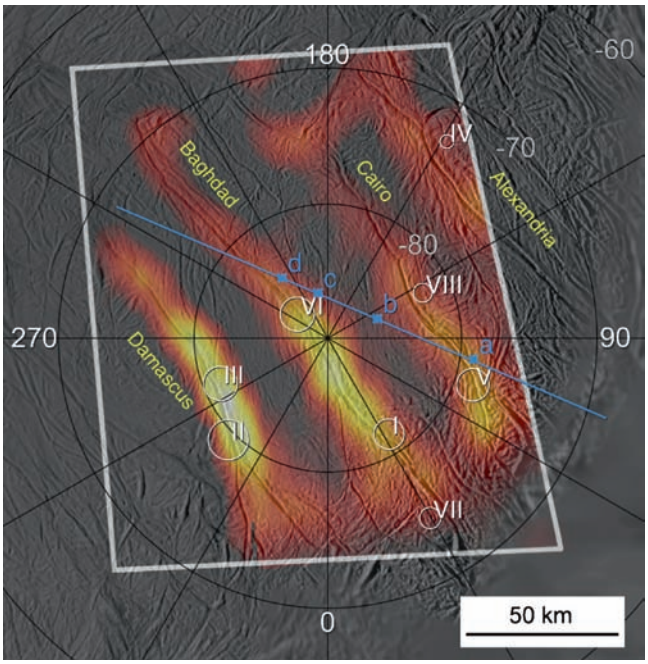

Fig. 21.14 Locations of thermal emission, plume sources, and jets seen in stellar occultations relative to the geological features of Enceladus' south polar region. The warm colors superposed on the base map show the distribution of 9–17 μm thermal emission seen by CIRS on March 12th 2008 (Cassini press release image PIA10361 NASA/JPL/GSFC/SwRI/SSI), with a spatial resolution of about 15 km. Only the region within the white trapezoidal outline was mapped by CIRS. The white circles show the locations (with uncertainties) of dust plume sources seen by ISS, from Spitale and Porco 2007). The blue line shows the surface trace of a stellar occultation observed by UVIS (Hansen et al. 2008), with letters identifying the locations, projected onto the occultation trace, of discrete gas jets seen in the occultation (Fig. 21.17)

21.5.2.2 Composite Infrared Spectrometer (CIRS)

The thermal emission from Enceladus' warm south pole is observed by the CIRS instrument, which obtains spatially resolved spectra with resolution down to a few kilometers, sufficient to map the warm areas in relation to surface features such as the tiger stripes. CIRS uses three detectors covering the 10–1,500 cm^{-1} range, and CIRS' most useful observations prior to 2008 were taken with the 600–1,100 cm^{-1} (9.1–16.6 μm) detector. CIRS observations constrain the total radiated power from the south polar region, and the spatial distribution of temperatures.

Figure 21.15 shows mid-IR maps, superposed on an ISS base map, and spectra of the south polar region from the 14 July 2005 flyby and from a distant observation on November 9th 2006 (Abramov and Spencer 2009). The prominent south polar hot spot seen in both observations corresponds to the location of the tiger stripes, and higher spatial resolution CIRS observations in March 2008 (Fig. 21.14) show that nearly all the thermal emission comes from the tiger stripes and associated fractures. The observed emission is much brighter than the expected passive thermal emission from the sun-heated surface (blue curves in Fig. 21.15): the elevated temperatures are therefore maintained by heat from within, escaping along the tiger stripes.

The shape of the average CIRS south polar spectra in Fig. 21.15 require relatively high temperatures occupying a small fraction of the CIRS field of view. After subtracting the expected passive thermal radiation, the average spectrum south of 65°S from July 2005 can be fit by a blackbody at about 133 K occupying an area of about 345 km^2 (Fig. 21.15), which is a small fraction of the 37,000 km^2 area of the region and is equivalent to a strip with an average width of 700 m along the approximately 500 km length of the tiger stripe fractures. This width is a small fraction of the 2 km distance between the ridge crests of the fractures. 1,100–1,500 cm^{-1} spectra of Damascus Sulcus from the August 2008 flyby, at higher spatial resolution, indicate places on the surface as warm as 167 K (JPL news release 2008–185). The power radiated by the tiger stripes, determined from the July 2005 blackbody fits, is 5.8 ± 1.9 GW, with an uncertainty that is dominated by the assumed temperature. This is a lower limit to Enceladus' total endogenic power, because additional power is likely to be radiated at temperatures too low to be detected in the CIRS 600–1,100 cm^{-1} bandpass. Assuming the total length of the tiger stripes is 500 km, the average power per unit length is thus at least ∼12 kW m^{-1}.

Spencer et al. (2006) note that if the plume gases seen by UVIS were in vapor pressure equilibrium with surface ice that was visible to CIRS, a temperature of at least 180 K could be inferred for the gas source: lower temperatures would require a larger area of exposed ice to produce the H_2O flux observed by UVIS, and would thus produce a brighter thermal infrared signature than CIRS observed. The corresponding upper limit to the width of the plume source is 50 m, averaged along the length of the tiger stripes. Because of the strong dependence of vapor pressure and sublimation rate on temperature, the source width decreases rapidly for higher temperatures: ∼10 cm for 225 K, and ∼1 mm for 273 K.

Additional CIRS observations of the south pole in November 2006 (Fig. 21.15) show that the total radiated power and its spatial distribution was essentially unchanged since July 2005, with a <15% change in total 15 μm radiance (Abramov and Spencer 2009).

21.5.2.3 Ultraviolet Imaging Spectrometer (UVIS)

The Cassini UVIS instrument has probed the structure and chemistry of the Enceladus plume gases by means of two stellar occultations: a vertical cut through the plume on July

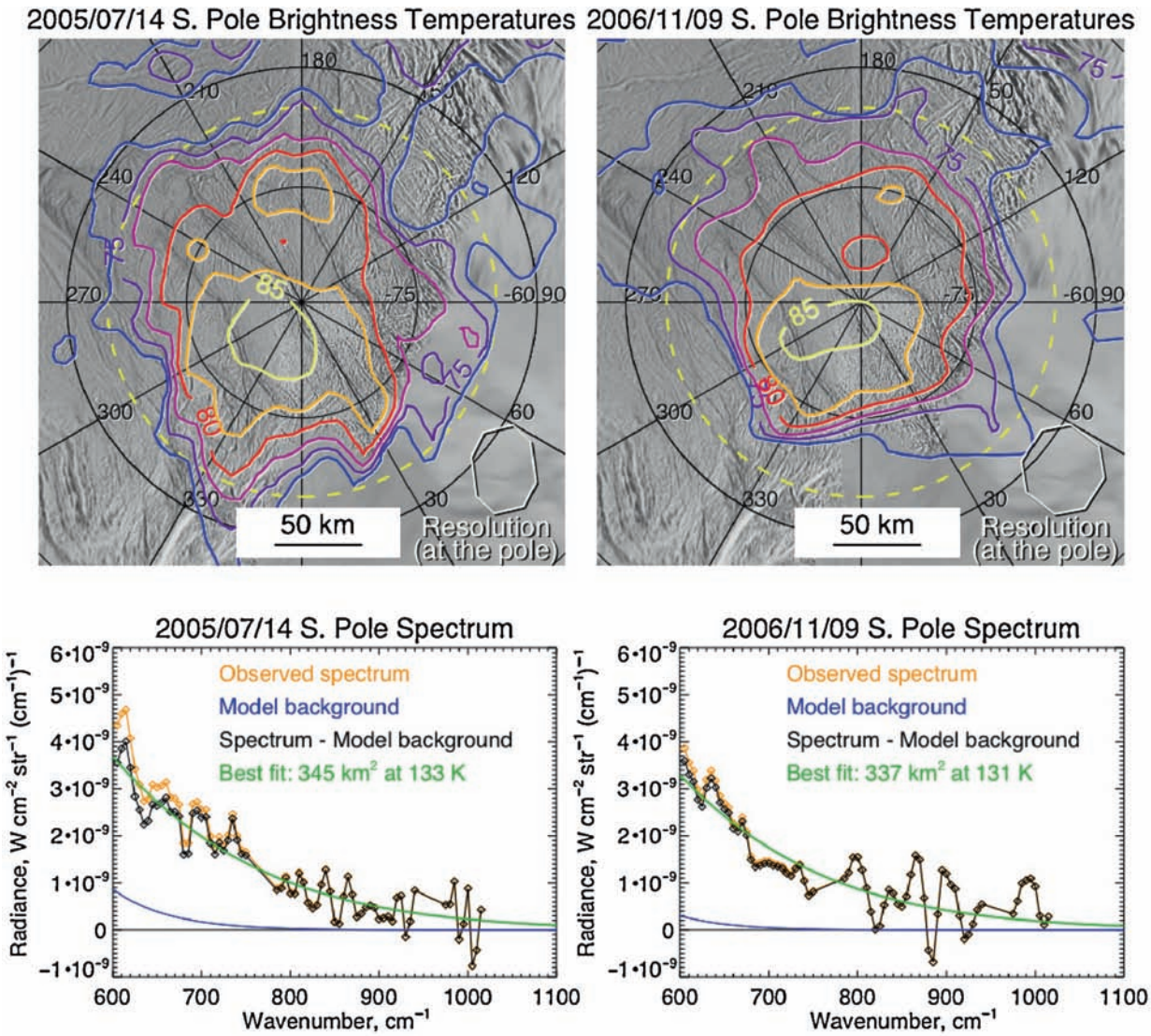

Fig. 21.15 9.1–16.6 μm (600–1,100 cm^{-1}) maps and spectra of the south pole of Enceladus, seen by CIRS during the July 14th 2005 flyby and during more distant observations on Nov. 9th 2006 (Abramov and Spencer 2009). The spectra show the average thermal emission from within the dashed yellow circle. Contours show brightness temperature, which is the temperature of a pixel-filling blackbody radiating the observed flux. See the text for details

14th 2005 (Hansen et al. 2006), extending down to the surface, and a horizontal cut on October 24th 2007 (Hansen et al. 2008), with a minimum altitude of 16 km. Two components of UVIS are used: the High Speed Photometer (HSP), which provides high time resolution over a 1,100–1,900 Å bandpass, and the Far Ultraviolet Spectrograph (FUV), which generates 1,115–1,914 Å spectra with lower time resolution. Both instruments are sensitive to absorption of starlight by water vapor and potentially by other gases.

The absorption spectrum of the plume gases from both occultations clearly shows the signature of water vapor (Fig. 21.16) and allows its abundance to be mapped as a function of position in the plume, as discussed below. Absorption due to CO is not observed in the UVIS FUV spectrum in either 2005 or 2007, with a formal 2-σ upper limit of 3.6×10^{14} cm^{-2}, corresponding to a mixing ratio with H_2O of <3% (Hansen et al. 2008). This may be consistent with the presence of CO in the INMS spectra if, as is likely (Waite et al. 2009, Section 21.5.2.4), the CO seen by INMS is primarily a breakdown product of CO_2 within the instrument.

The two occultation cuts through the plume reveal much about the plume's structure and dynamics. The attenuation of the star signal during the 2005 occultation is best fit by an exponential decline with altitude, with scale height of 80 km, and the horizontal cut through the plume in the 2007 occultation (Hansen et al. 2008) reveals additional details (Fig. 21.17). There are four statistically significant narrow jets superposed on the broader plume background. In

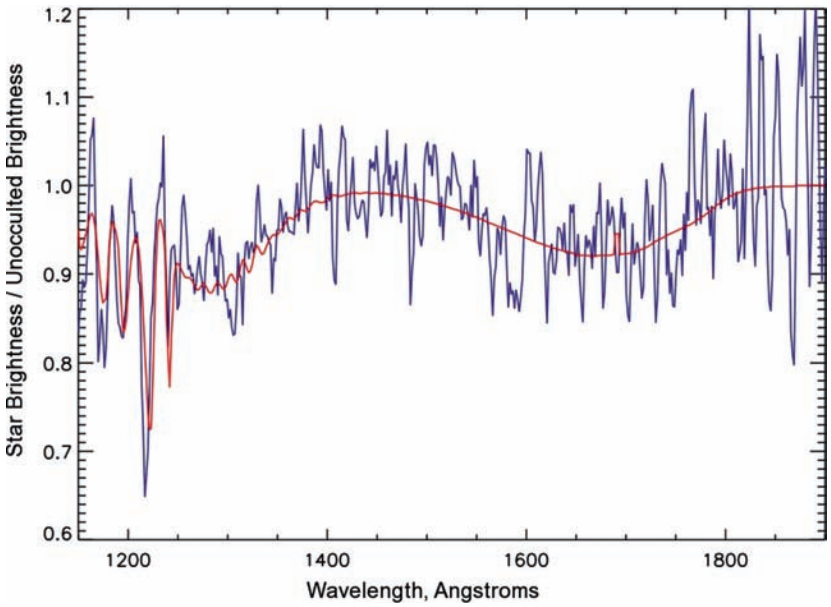

Fig. 21.16 The spectrum of the occultation star shortly before the July 14, 2005 occultation, divided by the average unocculted star spectrum (I_0), showing absorption due to H_2O vapor in the Enceladus plume. A water spectrum with column density $n = 1.5 \times 10^{16}\,\mathrm{cm}^{-2}$ is compared (*thick line*) (Hansen et al. 2006)

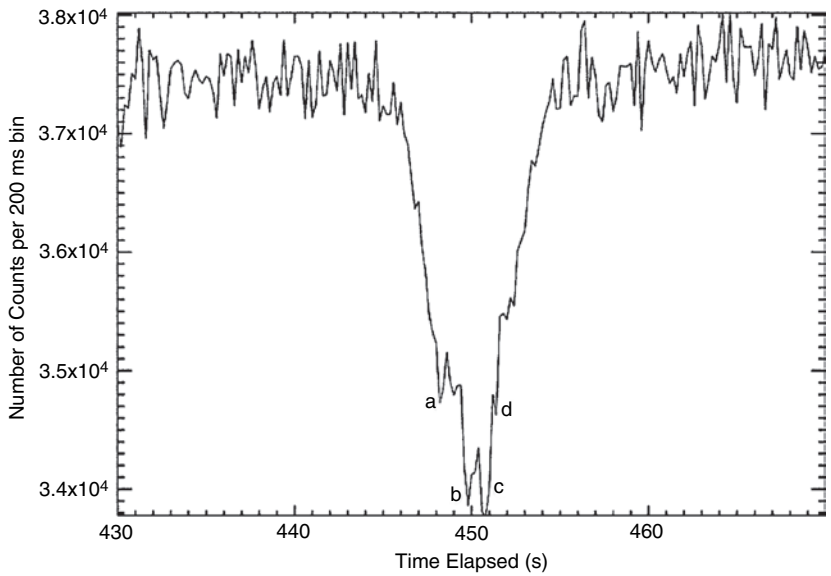

Fig. 21.17 HSP data from the 2007 UVIS plume stellar occultation is shown binned to 200 ms intervals. The large absorption is due to the water vapor in the large background plume. The narrower numbered absorption features a, b, c, and d indicate individual jets in the plume (Hansen et al. 2008)

Fig. 21.14 the blue line is the path of the point on Enceladus closest to the ray as the 2007 occultation progressed-these jets correspond roughly, but not precisely, to some of the Spitale and Porco (2007) jets. The points labeled a, b, c, d correspond to the absorption events labeled a, b, c, d in Fig. 21.17. The prominent jets 'b' and 'c' are spaced 20 km apart, and the jet width combined with the height above the surface constrains the jet opening angle, which in turn constrains the ratio v_B/v_T where v_B is the vertical bulk velocity and v_T is the thermal velocity (see Tian et al. 2007). The idea is that the gas expands horizontally at speed v_T and travels vertically at speed v_B. From these data, $v_B/v_T \sim 1.5$. The whole occultation profile can be well represented with 8 equally spaced jets whose strengths are not equal but which all share this ratio. ISS images (Spitale and Porco 2007) reveal a much more complex situation, but a model with more closely spaced jets would require a higher value of this ratio. Assuming a gas temperature of $T = 180\,\mathrm{K}$, the lower limit inferred by CIRS (Spencer et al. 2006), gives a thermal velocity $v_T = 406\,\mathrm{m\,s}^{-1}$, and thus a vertical velocity of $406 \times 1.5 = 609\,\mathrm{m\,s}^{-1}$, well above the Enceladus escape velocity of $235\,\mathrm{m\,s}^{-1}$.

The 2007 HSP data in Fig. 21.17 give a peak H_2O column density of $2.6 \times 10^{16}\,\mathrm{cm}^{-2}$ along a horizontal path passing 15 km above the surface of Enceladus. The UVIS FUV spectra, which have lower time resolution and thus provide

densities more representative of the average plume density, give water column abundances $1.26 \pm 0.14 \times 10^{16}\,\mathrm{cm}^{-2}$, and $1.36 \pm 0.14 \times 10^{16}\,\mathrm{cm}^{-2}$ for the two spectra closest to Enceladus, comparable to near-surface densities seen in the 2005 occultation (Fig. 21.16). The escape rate of water molecules from Enceladus with these column densities and the $609\,\mathrm{m\,s}^{-1}$ vertical velocity, and a plume horizontal dimension of 80 km (assumed similar to the scale height) is $\sim 6.5 \times 10^{27}$ molecule s^{-1} or $\sim 200\,\mathrm{kg\,s}^{-1}$ using the methodology of Hansen et al. (2006). Modeling of the 2005 occultation data with similar assumptions also gives a $200\,\mathrm{kg\,s}^{-1}$ escape flux. Tian et al. (2007), using a more detailed model of the plume geometry, calculate a source flux of $4–6 \times 10^{27}$ molecules s^{-1} and a vertical velocity of 300–500 m s^{-1} in order to match the UVIS vertical profile, consistent with these results.

If the density at the source n_0 is approximately the vapor pressure of the surface ice, this limits the area of a single source. For $T = 180\mathrm{K}$, $\left(n_0 = 2 \times 10^{12}\,\mathrm{cm}^{-3}\right)$, with 8 sources and the total water flux of $\sim 6.5 \times 10^{27}$ molecule s^{-1}, a single source has area $0.6\,\mathrm{km}^2$. This is highly temperature-dependent: for $T = 200\mathrm{K}$, the area would be 20 × smaller.

Comparison of the 2007 to the 2005 plume column density at ∼15 km altitude from the FUV spectra gives a value 1.7 times higher in 2007. HSP values at the same altitudes, 15.6–22 km, give a ratio of the attenuation in 2007–2005 of 1.4 ± 0.4, which is consistent. An increased plume density in 2007 is inferred (Hansen et al. 2008), though comparison is complicated by the differing geometry of the two occultations.

21.5.2.4 Ion and Neutral Mass Spectrometer (INMS)

INMS has sampled the structure and chemistry of the plume on several flybys. The July 2005 flyby (Waite et al. 2006) indicated that the plume gas composition (Table 21.3) was dominantly H_2O with minor CO_2, CH_4, and a mass 28 peak which could be due to CO and/or N_2. The structure of the water vapor profile during the encounter suggested the existence of both a plume source for the gas and a more distributed source due to sputtering of the surface of Enceladus.

In March and October 2008 there were two much deeper plume penetrations that were optimized for plume sampling. Cassini came within 25–50 km of the surface of Enceladus and flew through the center of the plume at altitudes of a few 100 km on its outbound path (Figure 21.2). The proximity to the plume source resulted in a two order of magnitude increase in signal to noise relative to the July 2005 flyby. The mass spectrum obtained from the October 9th 2008 flyby (Waite et al. 2009) is shown in Fig. 21.18. The complexity of the organic mixture leads to many overlapping mass

Table 21.3 Composition of the Enceladus plume as measured by INMS during the October 9th 2008 flyby (Waite et al. 2009)

Species	Molar mixing ratio
H_2O[a]	0.90 ± 0.01
CO_2[a]	0.053 ± 0.001
H_2CO	$(3.1 \pm 1) \times 10^{-3}$
CH_3OH	$(1.5 \pm 0.6) \times 10^{-4}$
C_2H_4O	$<7.0 \times 10^{-4}$
C_2H_6O	$<3.0 \times 10^{-4}$
H_2S	$(2.1 \pm 1) \times 10^{-5}$
^{40}Ar	$(3.1 \pm 0.3) \times 10^{-4}$
$^{36}Ar + {}^{38}Ar$	$<1 \times 10^{-5}$
NH_3	$(8.2 \pm 0.2) \times 10^{-3}$
N_2[b]	<0.011
HCN[b]	$<7.4 \times 10^{-3}$
CH_4	$(9.1 \pm 0.5) \times 10^{-3}$
C_2H_2	$(3.3 \pm 2) \times 10^{-3}$
C_2H_4[b]	<0.012
C_2H_6	$<1.7 \times 10^{-3}$
C_3H_4	$<1.1 \times 10^{-4}$
C_3H_6	$(1.4 \pm 0.3) \times 10^{-3}$
C_3H_8	$<1.4 \times 10^{-3}$
C_4H_2	$(3.7 \pm 0.8) \times 10^{-5}$
C_4H_4	$(1.5 \pm 0.6) \times 10^{-5}$
C_4H_6	$(5.7 \pm 3) \times 10^{-5}$
C_4H_8	$(2.3 \pm 0.3) \times 10^{-4}$
C_4H_{10}	$<7.2 \times 10^{-4}$
C_5H_6	$<2.7 \times 10^{-6}$
C_5H_{12}	$<6.2 \times 10^{-5}$
C_6H_6	$(8.1 \pm 1) \times 10^{-5}$

[a]Includes CO and H_2 which are assumed to be derived from dissociation of H_2O and CO_2 in the instrument.
[b]INMS cannot distinguish between (N_2+ HCN) and C_2H_4. N_2 and HCN abundances equal the given upper limit if C_2H_4 is absent, and C_2H_4 abundance equals the given upper limit if N_2 and HCN are absent. The N_2/HCN ratio, however, is well constrained by the data.

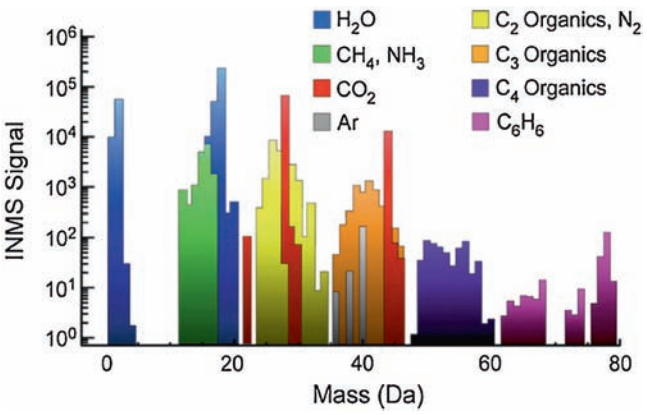

Fig. 21.18 Mass spectrum of the Enceladus plume from the October 9th 2008 flyby. The colors show contributions from various species and their breakdown products using the composition shown in Table 21.3. Reprinted by permission from Macmillan Publishers Ltd: Nature (Waite et al. 2009), copyright 2009

peaks that cannot be uniquely separated with the mass resolution of INMS, and many molecules are dissociated on impact with the instrument, especially at the high speeds of the 2008 flybys (14.4 and 17.7 km s^{-1}), resulting in detection of molecular fragments. Another complication is the tendency for water vapor to stick to the interior wall of the antechamber. This has two consequences: (1) it may displace gases already absorbed onto the surface and complicate the interpretation of minor species, and (2) the stickiness produces a shift in time and broadening of the water vapor time dependent structure. Mass deconvolution and modeling of impact dissociation leads to the estimated composition shown in Table 21.3. Water is again the dominant constituent, and may be even more abundant than indicated here, due to instrumental effects. The mass 28 species appears to be a mixture of CO and N_2 and/or C_2H_4, with the CO derived primarily from CO_2 dissociation in the instrument. The fact that the observed CO may be largely created within INMS is consistent with the lack of CO in the UVIS (Hansen et al. 2006) or VIMS (Brown et al. 2006) data. Methane (CH_4) and CO_2 are seen as in July 2005, and there is also, for the first time, a firm detection of NH_3, which is important because of its potential role as an antifreeze inside Enceladus. There are also many heavier organics, including benzene. Radiogenic ^{40}Ar is also apparently detected, at surprisingly high abundance, but primordial, non-radiogenic, ^{36}Ar and ^{38}Ar are not seen. The data also yield a D/H ratio of 2.9 $(+1.5/-0.7) \times 10^{-4}$, which is close the cometary value, twice the terrestrial value, and ten times the protosolar value (Waite et al. 2009).

The water density in the March and October 2008 flybys was strongly peaked over the south pole, indicating a dominant plume source for the gas. Unlike the July 2005 flyby, there was no evidence of more widely distributed source of gas at other latitudes on Enceladus. The difference may be due to the different flyby geometry, though instrumental effects may also be involved.

21.5.2.5 Cosmic Dust Analyzer (CDA)

The CDA makes direct measurements of the particles encountered by the spacecraft. ("Dust" includes particles of any composition, including ice). Spahn et al. (2006a) show data collected during the July 2005 flyby with a CDA sensor that is sensitive to particles with a radius larger than 2 μm. The sensor recorded a maximum impact rate of ∼4 particles s^{-1} at 1 min before the closest approach to Enceladus, during passage through the plume. Modeling these data, including the dynamics of particles that escape from Enceladus and go into orbit around Saturn, Spahn et al. inferred a rate of particles larger than 2 μm emitted by the south pole source and escaping the moon's gravity of 5×10^{12} particles s^{-1}. They also inferred an isotropic source, perhaps impact ejecta, with about 5× smaller strength., similar to the isotropic gas source seen by INMS in July 2005 (but not in March 2008). These dust numbers correspond to an escaping dust mass of at least 0.2 kg s^{-1}, assuming a 2 μm radius for all grains. The authors concluded that these processes probably provide the dominant source of Saturn's E ring. Kempf et al. (2008) show that the ejected particles must have a speed greater than 222 m s^{-1} to avoid re-collision with Enceladus. This is significantly larger than the 3-body escape speed from the South pole.

CDA has also measured the compositions of dust particles in the E-ring, which are derived from the Enceladus plume. Postberg et al. (2008) report several classes of particles, including pure water ice particles, and water ice particles contaminated by organic compounds and/or silicate minerals. They speculate that the pure ice particles might be impact ejecta from Enceladus' surface, while the impure particles are from the Enceladus plumes, though it is also plausible that both particle types come from the plumes. Most particles also contain a small amount of sodium. However, a few percent of measured particles are enriched in the sodium salts NaCl, $NaHCO_3$, and/or Na_2CO_3 by several orders of magnitude, with potassium salts also present (Postberg et al. 2009).

More detailed dust measurements were made by CDA during the deeper plume passages on August 11th 2008 and October 9th 2008, but these results were not published at the time of writing.

21.5.2.6 Visual and Infrared Mapping Spectrometer (VIMS)

VIMS has obtained spectra of both the plume itself and the surface deposits around the plume sources, constraining both particle size and particle composition. Spectra of surface plume deposits are roughly consistent with the plume composition, as discussed in Section 21.4.1. However alteration of the particle properties – radiation damage, sintering, loss of volatiles, and change in crystal size – complicates the interpretation since the time scale and degree of alteration are hard to determine.

Spectra of the surface seen through the plume provide an upper limit on CO in the plume gas of 10^{14} molecules cm^{-2} (Brown et al. 2006), which is less than 1% of the water vapor column density detected by UVIS, and the likely global upper limit to NH_3 on the surface is 2%. Both of these limits are consistent with recent interpretation of INMS results (Section 21.5.2.4). VIMS has not yet seen thermal emission from the plume sources: the upper limit on the temperature of filled pixels 5–10 km on a side from 2005 observations is 140 K (Brown et al. 2006), which is consistent with CIRS results that show much smaller areas at these temperatures.

Hedman et al. (2009) use November 2005 VIMS spectra of the plume itself, seen at high phase angle, to infer the size of particles in the plumes at altitudes between 50 and 300 km. Smaller particles have weaker water ice spectral signatures, because a greater fraction of the light is scattered off the particle surfaces without penetrating into the material. They find typical particle radii of order 1 μm, consistent with the size of E ring particles. They also find a falloff in particle size with altitude, and used this to model the distribution of ejection speeds, in the 80–180 m s^{-1} range, as a function of particle radius. They inferred a uniform distribution of ejection speeds in this range for 1 μm particles, but a strong preference for speeds at the slow end of the range for 3 μm particles.

21.5.2.7 Magnetometer (MAG) and Cassini Plasma Spectrometer (CAPS)

During the February and March 2005 Enceladus flybys, the Cassini magnetometer detected the magnetic signature of the deflection of the Saturn magnetospheric plasma around a conductive barrier at Enceladus, and also detected cyclotron waves at the water group gyrofrequency which indicated a major ion source at Enceladus (Dougherty et al. 2006). These discoveries prompted the reduction in the altitude of the July 2005 flyby and thus enabled the first direct sampling of the plume. The July 2005 flyby also provided additional details of the magnetic signature, showing that the source of the magnetic perturbation was centered south of Enceladus, consistent with other observations of the south polar plume. Differences between the magnetic signatures on the three 2005 flybys suggested temporal variations in plume activity. Saur et al. (2008) modeled the magnetic signature and for the March and July 2005 flyby data obtained densities of H_2O molecules in the plume that are in good agreement with those inferred from the UVIS stellar occultations (Hansen et al. 2006). The February 2005 data, in contrast, indicated a 8× larger gas density during that flyby, suggesting large temporal variability on several-week timescales, though again the different geometry of the various observations complicates comparison.

During the March 2008 flyby, the Cassini plasma spectrometer (CAPS) saw signatures apparently due to the impact of nanometer-sized ice grains with the instrument (Jones et al. 2009), with flux spike locations consistent with the jet locations determined by Spitale and Porco (2007).

21.5.2.8 Groundbased Observations

Although almost all recent data on the Enceladus plumes has come from Cassini, recent ground-based work provides additional constraints on the plume composition. Schneider et al. (2009) use Earth-based spectroscopy to establish a strong upper bound on neutral sodium from Enceladus ($Na/H_2O < 4 \times 10^{-7}$ in the plume and $<7 \times 10^{-6}$ in the E-ring). This constraint is consistent with the CDA sodium detection in the E-ring particles discussed above even if (as is likely) the particles release their sodium as they are sputtered away, because the particles comprise a small fraction of the total plume mass, and only a small fraction of the particles contain significant quantities of sodium.

21.5.3 Plume Models

The plumes offer a unique window into the interior of Enceladus, and there has already been much work to infer the nature of the plume source from the available data. A critical question is whether liquid water is required to generate the plumes, and if so, how close to the surface the water must be.

21.5.3.1 Transfer of Heat to the Surface

To use the surface temperatures and radiated power to infer subsurface conditions, it is necessary to consider the mechanisms that bring the observed heat to the surface where it is detected. The heat may be transferred to the surface from the source by conduction through the ice, or by the plume gases, either as sensible or latent heat, or by flow of liquid water. The radiated power per unit length of the tiger stripes, assuming the >6 GW total is distributed evenly along the 500 km cumulative length of the tiger stripes is at least 12 kW m^{-1}. An additional ∼0.5 GW (the vapor loss rate of ∼200 kg s^{-1} multiplied by the latent heat, L, of the water vapor, $\sim 2.8 \times 10^6$ J kg^{-1}), is carried away in the form of latent heat in the plume.

Spencer et al. (2006) note that liquid water would have to be very close to the surface if the warm surface temperatures were maintained only by thermal conduction from below. For instance a 180 K blackbody has a heat flux $F = 60$ W m^{-2}, and ice near its melting point has a thermal conductivity $k = 2.4$ W $(m\,K)^{-1}$, which means that the temperature gradient dT/dz into the ice would be 25 K m^{-1}. With a surface temperature of 180 K, the ice would melt at 4 m depth if thermal conduction were the only heat loss mechanism.

Spencer et al. (2006), and Nimmo et al. (2007) point out that the vapor provides another way to transport heat to the surface. The simplest picture is that vertical fractures run the length of the tiger stripes, and plume vapor traveling up these fractures delivers heat to the fracture walls. The shape of the CIRS thermal emission spectra is roughly consistent with this model. Abramov and Spencer (2009) use a 2-D

thermal model to show that both the total power and the wavelength distribution of the thermal emission spectra can be matched quite well by assuming that most of the internal heat is radiated from the near-fracture surfaces, which are warmed by conduction through the ice from the fractures themselves. Assuming that the conduction is through solid ice, fracture temperatures near 225 K match the CIRS spectra well, though higher fracture temperatures cannot be ruled out if there is a thin insulating layer on the surface. However, multiple fractures are required along at least some portions of the tiger stripes to match the total south polar radiated power.

Ingersoll and Pankine (2009) argue that in a gas-filled fracture, condensation and evaporation are so rapid that the vapor pressure of the gas is fully determined by the saturation vapor pressure of the walls. Tiny differences between the two pressures drive large mass fluxes of water between the walls and the gas. These fluxes maintain the gas at the saturation vapor pressure of the walls. Condensation and evaporation occur, but they occur under quasi-equilibrium, i.e., reversible conditions.

Assuming the gas moves upward at thermal speeds, and is in vapor pressure equilibrium with the walls, the rate of upward heat transport is given by $wL\, e\,(T)\,(RT)^{-1/2}$, where $e(T)$ is the ice vapor pressure and w is the fracture width (Ingersoll and Pankine 2009). The observed average heat flow of $12\,\mathrm{kW\,m^{-1}}$ can be matched by a single fracture with temperatures of ∼215 K and ∼276 K for fracture widths of 1 m and 2 mm, respectively. Heat can thus be transported fast enough to prevent near-surface melting if the fractures are wider than a few millimeters. If there are several cracks per tiger stripe, each crack has to supply only a fraction of the $12\,\mathrm{kW\,m^{-1}}$, and the temperatures will be lower.

Schmidt et al. (2008) note that condensation of vapor on the fracture walls may close the fractures on a timescale of months. Ingersoll and Pankine (2009) reach similar conclusions. Very near the surface, where the depth is comparable to the width of the crack, they note that the heat flux into the walls is comparable to the heat flux that is radiated into space. This means that the crack closes at a rate $F/(L\rho_i) = 0.74\,\mathrm{m\,year^{-1}}$ using F appropriate for a surface at 180 K, where $\rho_i = 917\,\mathrm{kg\,m^{-3}}$ is the density of ice and $F = 60\,\mathrm{W\,m^{-2}}$. A crack of width 1 m will close in a little more than a year, while crack of width 2 mm will close in less than a day. New cracks would therefore have to be forming constantly. If the surface is warmer, then F is greater and the crack will close even faster. Narrow cracks might perhaps be kept open by erosion of the walls by the vapor and entrained particulates, or by mechanical stresses associated with the tidal flexing.

The efficiency of vapor transport also affects conditions at depth, where the tidal dissipation is occurring. The Nimmo et al. (2007) shear heating model assumes efficient transport of heat from the shear zone to the surface by water vapor – the heat transport reduces temperatures in the shear zone, thus increasing viscosity and enhancing shear heating, and allowing generation of the observed heat and vapor flux without subsurface melting. This model is able to reproduce the observed heat flow and the observed vapor production rate. However, the model overestimates the efficiency of vapor transport because it neglects condensation of the vapor onto the surrounding ice matrix, as noted by Ingersoll and Pankine (2009). The water vapor pressures assumed by the Nimmo et al. model (Fig. D of their supplemental material) are several orders of magnitude higher than the vapor pressure of ice at the assumed temperature, so the vapor should condense and would not be able to transport the heat to the surface, as the model requires. Sufficient heat transport can be maintained at the lower equilibrium vapor pressures only if the diffusion coefficient of the vapor in the subsurface ice is much higher than assumed by Nimmo et al.

Ingersoll and Pankine (2009) use a hydrodynamic model to show that if the heat is generated on meter-sized cracks in the near-surface brittle zone, and if the cracks open and close with position in the orbit (Hurford et al. 2007), the upward flow of vapor can carry the heat away. However removal of any frictional heat generated in the underlying ductile zone is more difficult, because open fractures are less likely, and conduction or convection are likely to be the dominant heat transport methods. If the ductile zone warms to a temperature where viscosity is low enough that frictional heating is negligible, melting in the ductile zone might be avoided, but detailed self-consistent models have not yet been developed.

Kieffer et al. (2006) and Gioia et al. (2007) postulate a low-temperature plume source, below 200 K, driven by clathrate decomposition at depth (see the discussion of plume composition below). In this model open cracks extend all the way down to the source, at depths of 35 km or greater, and again, advection of plume vapor up these fractures is sufficient to carry the heat away. Accordingly, they call this the "Frigid Faithful" model. In this model, thermal expansion in the source region accounts for the tiger stripes and other surface features seen in the south polar region. The cracks must have a certain minimum width, on the order of 10 cm. Gioia et al. argue that the crust is so cold and is strengthened by the presence of clathrate hydrates, that it behaves like a brittle elastic solid, so the cracks do not close up.

In summary, vapor transport along the tiger stripe fractures may be able to bring heat to the surface of Enceladus efficiently enough to explain the observed thermal signature without requiring liquid water near the surface or at depth. Whether temperatures reach the melting point depends on the width of the fractures and the details of the heat generation mechanism, and new observations and models may provide a clearer answer.

Liquid water would presumably transport heat to the surface more efficiently than gas. However, Postberg et al.

(2009) show (in the paper's supplementary information) that for evaporation from a water surface in a fracture of constant width, heat cannot be transported upward through the water, by conduction or convection, quickly enough to replace the latent heat lost by evaporation at the water surface. Such a water column would therefore rapidly freeze at the surface. For heat transport to be sustainable, the cross-sectional area of the water column must be several orders of magnitude greater than the area venting to space. Postberg et al. therefore suggest that the plumes are fed by narrow fractures in the roof of vapor-filled chambers overlying relatively large bodies of water.

21.5.3.2 Plume Dynamics and Particle Formation

A high-pressure gas erupting into a low-pressure environment is a classic fluid dynamics problem, with applications ranging from rocket nozzles to volcanoes and geysers (e.g., Kieffer 1982). In ideal cases the gas can convert all of its initial enthalpy c_pT into kinetic energy. The specific heat c_p of water vapor is 1,850 J $(\mathrm{kg\,K})^{-1}$, which is almost exactly four times the gas constant R for water vapor. Thus the plumes could theoretically reach speeds of $\left(2C_pT\right)^{1/2} = 816$ and 1,005 m s^{-1} for $T = 180$ and 273 K, respectively. Actual gas speeds inferred from the plume shape seen by UVIS ($\sim$600 m s^{-1}, see Section 21.5.2.3 above), are lower than this maximum but higher than the thermal speed.

However, the fact that the temperature of the walls completely controls the temperature and pressure of the vapor means that the dynamics of the vapor is uncertain. If the temperature gradient dT/dz is small, then the pressure gradient dP/dz is small, and the force that accelerates the fluid is small. The velocity will be small as well. The fact that the observed velocity is not small, i.e., is larger than the thermal speed $(RT)^{1/2}$ implies that dT/dz is not small. Clearly the length, width, and temperature gradient in the crack are important parameters for the dynamics, but they depend on the thermal and mechanical history of the crack, which is uncertain.

The ice particles in the plume are the most readily observed aspect of Enceladus' activity. Their number density, speed distribution, size, and composition provide valuable constraints on the nature of the plumes and their source regions. Schmidt et al. (2008, Fig. 21.19) use models of the plume behavior in subsurface conduits to infer that the plume particle speeds and densities are consistent with particle formation by direct condensation of the water vapor in the plume before it reaches the surface. Their detailed hydrodynamic model includes homogeneous nucleation and particle growth in the gas as it expands toward the surface. The reservoir is at a given temperature T. The flow does not interact with the walls after it leaves the reservoir. Schmidt et al. derive particle speed and size distributions that match the observed and inferred properties of the plumes. The cracks have variable width, and Schmidt et al. show that repeated collisions of the grains, with re-acceleration by the gas, induce an effective friction that explains the reduced velocity of the grains when they leave the vent. Large grains emerge at slower speeds, consistent with the VIMS results (Hedman et al. 2009). The distance between collisions L_{coll} is assumed to be similar to the width of the crack. Thus $L_{\mathrm{coll}} = 0.1-1.0$ m. They then adjust the density of the gas to get the right velocity and cutoff radius for the

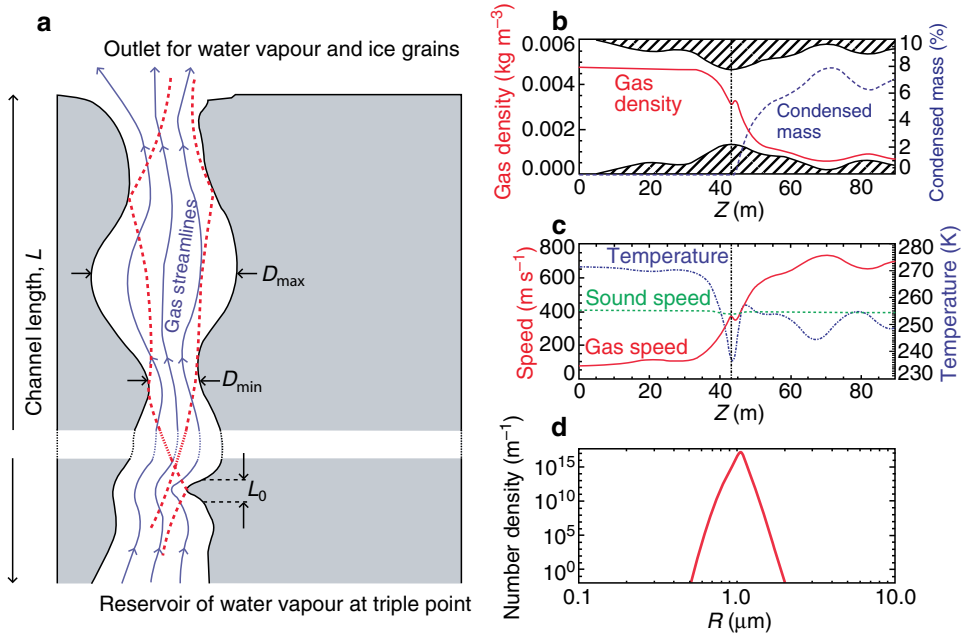

Fig. 21.19 Water vapor and ice grain interaction with the walls of a model plume vent, reprinted by permission from McMillan Publishers Ltd: Nature Schmidt et al. (2008), copyright 2008. (**a**) Model schematic. Gas flow upward from a liquid reservoir is modified by constrictions in the vent, and ice particles collide with the vent walls, slowing the particles. (**b**) Typical solution for gas density and condensed grain mass fraction as a function of depth z. Most grains nucleate at the narrowest part of the vent. (**c**) Profiles of gas speed and temperature. The gas becomes supersonic near the narrowest part of the vent. (**d**) Example distribution of condensed particle radii R

particles that escape to supply the E ring, given the gas speed inferred from the UVIS observations (Section 21.5.2.3). Since density depends on temperature when the gas is saturated, Schmidt et al. are able to estimate the temperature of the source. They find it is above 260 K, suggesting liquid water at the plume sources. Note that the Schmidt et al. model does not consider the effects on the gas and particle dynamics of vapor condensation on the walls, which is probably important especially near the surface (Ingersoll and Pankine 2009), though whether inclusion of these effects would change the conclusions remains to be seen.

The high ice/gas ratio in the plumes inferred from comparison of ISS images and UVIS measurements of the plume (Section 21.5.2.1) led Porco et al. (2006) to suggest that the observed plume particles might form directly from near-surface boiling of liquid water, which could provide an efficient way to generate particles. However, modeling by Brilliantov et al. (2008) implies that such particles would have speeds much lower than is inferred for the actual plume particles. Also, recent estimates of the ice/gas mass ratio are considerably lower (Kieffer et al. 2009), and ice/gas *production* ratios are lower still because of the average speed of the ice particles is much lower than that of the gas. The Kieffer et al. (2006) clathrate dissociation model may also have trouble explaining the speed of ice particles, because it is difficult for the low H_2O vapor density, resulting from the low temperatures of that model, to accelerate particles to the speeds observed (Brilliantov et al. 2008).

21.5.3.3 Plume Composition

While the plume is dominated by water vapor and water ice particles, the presence of additional species, including numerous gas species and salts in the plume particles, provides additional valuable clues to the plume origin.

Kieffer et al. (2006) point out that the other gases seen by INMS in the plume, notably N_2 (if present), CO_2 and CH_4, are insufficiently soluble in liquid water to have originated in their observed abundances from a liquid aqueous phase. Improved INMS 2008 plume composition measurements and solubility calculations confirm this conclusion (Waite et al. 2009). If the plume source is dominantly liquid water, the other gases must be present in another phase, such as gas bubbles. However, the solubility of these gases in clathrate hydrates (ices with a cage-like structure in which water ice traps other volatile components) is enormous compared with their solubility in liquid water. The observed molar ratio of H_2O vapor to non-condensable gases in the plume is $\sim$10:1. The similarity between this ratio and the ratio of water to guest molecules in a clathrate (hydration number is 6:1 to 8:1) suggests that the reservoir could consist of clathrates or clathrates plus water ice. Kieffer et al. suggest that the water and other gases can be released by depressurization of the clathrate to form the plumes at relatively low temperatures, below 200 K.

A problem with the Kieffer et al. model is that the sudden de-pressurization of clathrate-hydrate does not necessarily lead to vaporization of all the constituents. Only the more volatile constituents come off at low temperatures. For the Enceladus plumes, they come off in the order N_2, CH_4, and then CO_2 followed by water, which vaporizes at relatively high temperatures only. The plume should therefore be depleted in water vapor relative to the clathrate, and it is thus not clear whether clathrate dissociation can explain the abundance of water in the plume. Further laboratory work is needed. Halevy and Stewart (2008) elaborate on the clathrate dissociation model by considering non-equilibrium dissociation, modulated by the tidal opening and closing of the fractures described by Hurford et al. (2007). They predict that variations in both plume composition and density are possible as function of Enceladus' position in its orbit.

The ultimate source of the complex organics seen by INMS is an intriguing question. The detailed compositional information provided by INMS is likely to provide a strong constraint on possible formation mechanisms for the organics and other species, including interactions between the presumed ocean and the silicate core (e.g., Matson et al. 2007).

The detection of ice particles rich in NaCl and $NaHCO_3$ in the E-ring by CDA (Postberg et al. 2009) provides perhaps the strongest evidence yet for a liquid water plume source. The composition of these particles strongly suggests that they originate by direct freezing of saline water at the plume source, while the more common sodium-poor particles may be vapor condensates. The salt-rich particle compositions are similar to those expected for an Enceladus ocean that has been in contact with warm rock (Zolotov 2007), suggesting direct communication of the plume source with such an ocean. However, it is possible that preferential evaporation of H_2O has increased the salinity in the plume source reservoir, and that the ocean itself is less saline (Schneider et al. 2009). The extremely low sodium content of the neutral gases near Enceladus' orbit determined by Schneider et al. rules out plume production by wholesale boiling into space, without fractionation, of water derived from a salty ocean.

The apparent presence of abundant radiogenic ^{40}Ar in the plume provides additional indirect evidence for liquid water within Enceladus, because aqueous processes provide an efficient way to leach ^{40}Ar (or its parent species, ^{40}K) from the core and to concentrate the ^{40}Ar in the plume (Waite et al. 2009).

21.5.4 System Interaction

Saturn's system is filled with neutral products from the electron-impact dissociation and photodissociation of H_2O molecules. From measured O and OH abundances and theoretical estimates of the loss processes of all water products from the system, various investigators have estimated H_2O supply rates necessary to maintain a steady state as $> 2 \times 10^{27}$ H_2O molecules s^{-1} (Shemansky et al. 1993), possibly as high as 3.75×10^{27} (Jurac et al. 2002) or 10^{28} H_2O molecules s^{-1} (Jurac et al. 2005). These numbers are very similar to the inferred UVIS source rate of 6.5×10^{27} H_2O molecules s^{-1} (Hansen et al. 2008). It is thus very probable that Enceladus is the dominant source of the observed O and OH in the Saturn system. Johnson et al. (2006) suggest that the extended OH torus seen by Hubble is derived from charge exchange with a denser, colder, neutral gas torus that is populated directly by the Enceladus gas plumes. The neutrals are ionized to produce much of the magnetospheric plasma, though most of the mass loading occurs at some distance from Enceladus (Khurana et al. 2007). It is likely that nitrogen or ammonia from Enceladus' plumes is also the dominant source of the nitrogen found in the magnetosphere (Smith et al. 2008a), and products of ammonia have also been tentatively identified in the magnetosphere (Smith et al. 2008b).

Similarly, Enceladus' particle plumes are almost certainly the dominant source of Saturn's E-ring (Fig. 21.20), though a significant contribution from impact ejecta from the surface has also been suggested (Spahn et al. 2006a, Postberg et al. 2008). The ring, composed of water ice grains that are primarily 0.3 to 3 μm in size (Showalter et al. 1991, Nicholson et al. 1996), extends from about three to at least eight Saturn radii, with a peak density at or very close to Enceladus' orbit (Baum et al. 1981, Showalter et al. 1991). The lifetimes of 1-μm grains are <50 years (Jurac et al. 2002, Johnson et al. 2008), because water molecules are sputtered from the grains' surfaces by the plasma trapped in Saturn's magnetosphere. If Enceladus' plume has a comet-like particle-to-gas production ratio of 10%, then the mass of ice coming from Enceladus is roughly $20\,kg\,s^{-1}$, which is more than sufficient to compensate for the estimated particle loss rate of the E-ring of $1\,kg\,s^{-1}$ (Juhász and Horányi 2002). The Cassini CDA instrument has extensively sampled the E-ring, and the measured vertical structure can be used to constrain the plume dynamics. The ring thickness appears to be controlled by particles with ejection speeds near $230\,m\,s^{-1}$ (Kempf et al. 2008). Plasma drag effects are also important in determining the morphology of the ring (Juhász et al. 2007).

The E-ring particles in turn modify the surfaces and albedos of the other mid-sized Saturnian moons, as implied by the decrease in satellite albedo with distance from Enceladus (Verbiscer et al. 2007). In addition, the fact that Rhea, Dione, and Tethys, orbiting outside Enceladus, have trailing hemispheres that are darker than their leading hemispheres, while the reverse is true on Enceladus itself and Mimas (Buratti et al. 1998), is consistent with brightening of their surfaces by E-ring particles (Hamilton and Burns 1994).

21.5.5 Variability of the Activity

The E-ring has been in existence since at least 1966, when it was discovered (Feibelman 1967). Because the lifetime of the E-ring particles against sputtering is about 50 years (Jurac et al. 2002, Johnson et al. 2008), this implies that the current dust plumes have been feeding the E-ring for many

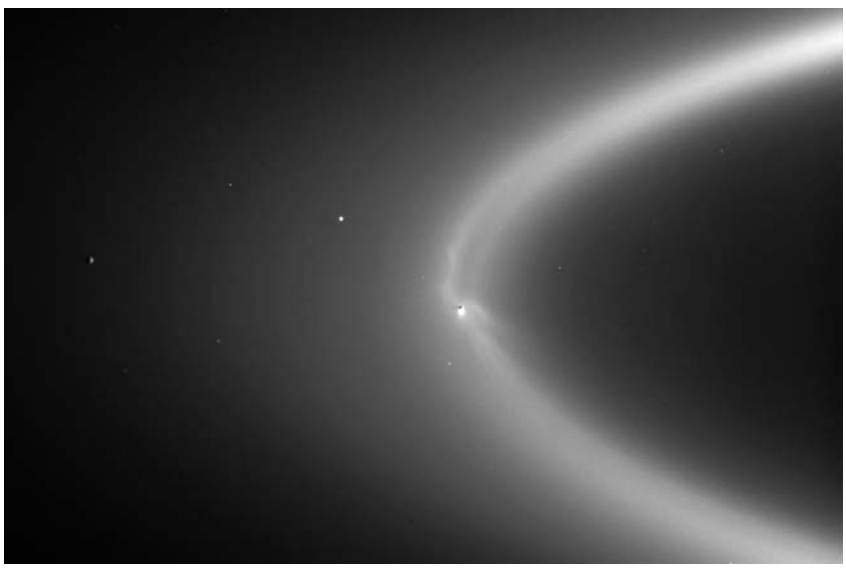

Fig. 21.20 Enceladus' complex interaction with the E ring, as seen by ISS at a phase angle of 175° on September 15, 2006. Enceladus is the dark dot in the center of the image (only its night side is visible at this phase angle), and the plume is the bright patch immediately below it. In contrast, no enhancement in ring density is visible near Tethys, which is on the far left of the image. Cassini press release image PIA08321, NASA/JPL/SSI

decades, but we have no direct information on activity earlier than about 100 years ago. We have direct evidence for gas plume activity only since the early 1990s, when the OH torus was discovered (Shemansky et al. 1993). OH lifetimes are tens of days, so gas torus variability should reveal variations in the plume activity on short timescales that would not be reflected in variations in the E-ring. Significant variability in neutral oxygen emission near Enceladus was indeed seen by UVIS during Cassini's approach to Saturn in 2004 (Esposito et al. 2005).

There is some evidence for variable features in the E-ring itself. An unusual discrete arc of particles in the E-ring, near Enceladus' orbit was seen in August 1995 using adaptive optics techniques by Roddier et al. (1998). However, they point out that its orbital longitude was distant from that of Enceladus and its lifetime was only a few hours, so it was probably not directly ejected from Enceladus.

Hurford et al. (2007) calculate the tidal stresses in an icy shell, focusing on the timing of the opening and closing of the cracks vs. position of Enceladus in its eccentric orbit, and provide maps of the stress state on each fracture as a function of orbital position. They predict greater plume activity at orbital longitudes when the cracks are open. These predictions have not yet been tested in detail, though the 1.7-fold difference between the plume gas densities inferred from the two UVIS stellar occultations (Hansen et al. 2008 and Section 21.5.2.3 above), which occurred at true anomalies of 98° and 254° respectively, are in the opposite sense to that predicted by Hurford et al. As noted above, the Cassini magnetometer data seem to indicate eightfold variations in gas plume density in the 20 days between the February and March 2005 Enceladus encounters, and comparison of E-ring particle models with CDA dust observations during close encounters also suggests variability in the particle plume output (Kempf et al. 2008). All these inferences of plume variability are somewhat model-dependent, as the geometry of the observations being compared differs significantly. As noted above, CIRS saw negligible change in the thermal emission from the south pole between July 2005 and November 2006 (Abramov and Spencer 2009).

On the longer term, several lines of evidence suggest that Enceladus is unusually active in the current epoch. See Section 21.2.7.

21.5.6 Conclusions: The Nature of the Plume Source

While many questions remain about the nature of the plume source, and the possible involvement of liquid water, progress has been made. Upward transfer of latent heat by water vapor is an effective means of bringing heat to the surface along the tiger stripes, though liquid water transport is also possible if surface freezing can be avoided. It seems likely that at least most of the observed plume particles can be produced by subsurface condensation of water vapor, though this is most easily accomplished at high subsurface gas pressures which themselves suggest near-melting temperatures. The presence of a small fraction of salt-rich particles in the E-ring is strong evidence that there is liquid water at the plume source, and that those particles are derived directly from that water. Possible alternative origins for these intriguing particles have not yet been explored, however. If the source is liquid water, it is not clear how the several percent of non-H_2O gases are introduced into the plume, and whether clathrates have a role to play. Continued analysis of the rich harvest of data from the current series of Cassini Enceladus flybys should provide a clearer picture in the near future.

21.6 Biological Potential of Enceladus

The observed plume and the associated thermal activity on Enceladus may indicate the presence of liquid water below the surface. From an astrobiological perspective, the possibility of liquid water opens up the question of life.

Discussions of life in subsurface water on Enceladus must logically begin with a consideration of the possible origin of life on that world. Unfortunately, we do not know how life originated on Earth nor have we been able to reproduce it in the laboratory. Indeed, there are many theories for how life originated on Earth (Davis and McKay 1996) and we can determine which of these would apply to Enceladus (McKay et al. 2008). Two of the theories for the origin of life on Earth would seem to apply to Enceladus, these are the organic "soup" theory and the deep sea vent theory.

The theory that the origin of life occurred in a soup of abiotically produced organic material is arguably the original theory for the origin of life and traces back to Darwin. It was given an experimental basis in the Miller–Urey experiment (Miller 1953) and has been extended since that time. On Earth the organics that comprised the soup could have been produced on the Earth or may have come in with comets and interplanetary dust. Applied to Enceladus the organic soup model might involve the formation of Enceladus from organic rich ices similar to cometary materials, consistent with INMS plume composition results. The organics would be in the mix from the start. As tidal heading forms a subsurface aquifer the solution would therefore be rich in organics comprising a suitable prebiotic soup.

The alternative theory for the origin of life on Earth that might apply well to Enceladus is the deep sea vent theory. In this scenario life began at the interface where chemically

rich fluids heated by tidal dissipation emerge from the silicate core below the sea bottom. Energy is derived from reduced gases such as H_2S and H_2 coming out from the vent in contact with a suitable oxidant, which can even be CO_2, to form a source of chemical energy (e.g., Corliss et al. 1981, Shock 1990, Wächtershäuser 1990). In this model for the origin of life the first organisms would be chemotrophs – consuming inorganics - whereas in the Miller–Urey model they would be hetereotrophs – eating organics.

The time required for the origin of life is unknown and one possible objection for the origin of life on Enceladus is that there might not be enough time. Would liquid water exist for long enough for life to start? There is evidence from cratering ages that the activity on Enceladus has persisted for at least hundreds of millions of years (Kargel and Pozio 1996, Porco et al. 2006), so long periods of time might be available, though we do not know how continuous the activity has been. The origin of life appears to have happened relatively quickly on Earth, before 3.5 Gyr ago (e.g., Tice and Lowe 2004). In a paper addressing the question of the time required for the origin of life, Lazcano and Miller (1994) suggest that, "in spite of the many uncertainties involved in the estimates of time for life to arise and evolve to cyanobacteria, we see no compelling reason to assume that this process, from the beginning of the primitive soup to cyanobacteria, took more than 10 million years." However, Orgel (1998) criticized this result stating that we do not understand the steps leading to life and consequently, we cannot estimate the time required. "Attempts to circumvent this essential difficulty are based on misunderstandings of the nature of the problem." The resolution of this question must await new data on Earth, the discovery of other life forms, or the ability to synthesize life in the laboratory.

A possibility that must also be considered is that life is present on Enceladus but did not originate there. This may also be true of the Earth. The idea that life was carried to the Earth from elsewhere is known as panspermia. The evidence that rocks from Mars have reached the Earth without experiencing temperatures high enough to sterilize their interiors has heightened interest in panspermia between the planets (Melosh 1988, Weiss et al. 2000, Gladman et al. 2005). McKay et al. (2008) point out that it is important to consider two possibilities for Enceladus: (1) life carried there from the inner solar system and (2) life brought to Enceladus as part of the material from which the Solar System formed. The former is unlikely given the distance to Enceladus and there is no data to support the latter model in which life in the Solar System comes from the pre-solar nebulae. These hypotheses are testable. If life is detected on Enceladus and found to be related to the phylogenetic tree of life on Earth this would argue for shared origin via panspermia.

For life to persist requires an environment of liquid water, the essential elements and nutrients, and a source of energy. The composition of the plume from the South Pole of Enceladus indicates that C and N, and probably S, are present in the source regions of the ice jet. If this source region is a subsurface liquid water aquifer then if phosphorous is present, all the biogenic elements (C,H,N,O,P,S) are present. Phosphorous is expected based on its abundance in rocky material. Thus, the remaining question to establish the possibility of an ecosystem is that of an energy source.

On Earth the dominant energy source for all ecosystems is sunlight. Even most subsurface ecosystems on Earth derive their energy from sunlight produced organic material from the surface. The deep sea vent communities derive energy from the reaction of H_2S from the vent with O_2 from the ambient seawater. However, this O_2 comes from surface photosynthesis. So these ecosystems are also dependent on surface photosynthesis.

To be the basis for a subsurface ecosystem on Enceladus we must turn to ecosystems on Earth that are completely independent of O_2 or organic material produced by surface photosynthesis (because of the cold vacuum conditions at the surface, we do not consider photosynthetic communities). Three such ecosystems have been reported.. The first ecosystem discovered that does not require oxygen, organic material, or sunlight is based on methanogens using H_2 derived from rock-water reactions in the Columbia River Basalts (Stevens and McKinley 1995). Chapelle et al. (2002) reported a similar system in the basalts of Idaho. A different ecosystem, also without requirements for O_2, organic material, or sunlight was discovered deep below the surface in South Africa (Lin et al. 2006) There the primary productivity of the system is based on sulfur-reducing bacteria using redox couples produced ultimately by radioactive decay.

These three microbial ecosystems are models for life that might be present inside Enceladus today – or in liquid water deep below the surface of other worlds such as Europa and Mars. Following this line of thought, McCollom (1999) considered methanogen-based biota for Europa as well as one based on sulfur-reducing bacteria. Most, if not all, of his analysis would apply to Enceladus. Figure 21.21 shows a proposed methane cycle that could support methanogens in a subsurface aquifer on Enceladus (or Europa) following the approach of McCollom (1999). Hydrogen and CO_2 present in the water provides a basis for methanogens which form CH_4 and biomass, acting as the primary producers in the community.

Gaidos et al. (1999) concluded that life trapped under thick ice covers in subsurface oceans eventually dies out due to depletion of redox pairs. In particular the availability of oxidants would eventually limit life in such an isolated ocean. A possible source of oxidants which would obviate this problem has been proposed for Europa based on oxidants produced by radiation on the surface of the ice and could be

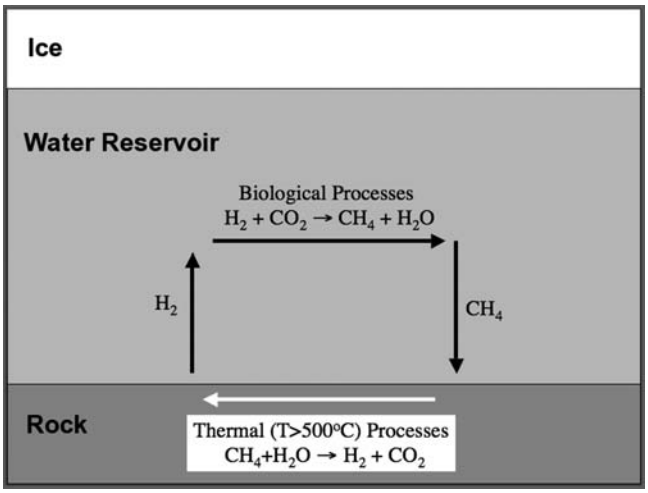

Fig. 21.21 Possible methane cycle on Enceladus (McKay et al. 2008)

carried to subsurface liquid water reservoirs that may contain reductants (Chyba and Phillips 2001, Hand et al. 2007). Parkinson et al. (2007) consider Enceladus and argue for a similar and strong source of surface oxidants there. There is no similar system on Earth but there is a rough analogy with the oxidants produced by radioactivity as observed by Lin et al. (2006).

However, it is worth noting that the three isolated microbial ecosystems discussed above provide a basis for considering how a long term biological cycle can persist in an ice-covered ocean even without a source of oxidants from the surface (McKay et al. 2008). If similar ecosystems existed on Enceladus, the chemical energy that supports life would come from long-lived non-biological energy sources (geothermal heat and radioactive decay). As shown above, these energy sources create redox pairs that recombine very slowly. Life catalyzes the recombination reaction harnessing the energy. The cycle can persist as long as the geochemical or radioactive energy is present – even if the system is isolated from outside sources of energy.

Parkinson et al. (2008) consider the geochemical cycles that might operate on Enceladus, and conclude that these may be sufficient to sustain life. Analyzing the organic compounds in the plume of Enceladus (e.g., Waite et al. 2006, 2009) is clearly the best way to detect any life in the subsurface aquifer. Life might be implicated by the presence of extreme chemical disequilibrium, for instance. The Cassini spacecraft is flying progressively more deeply through the plume as part of its extended mission, providing a steadily improving inventory of the plume's organic and inorganic chemistry, and a clearer picture of the possibility of life beneath the surface.

21.7 Summary and Future Exploration

By discovering ongoing geological activity at Enceladus' south pole, Cassini has confirmed, with a wealth of detail, earlier hints that this moon is one of the most remarkable bodies in the solar system. With the possible exception of Triton, which has active plumes that may result from either internally driven geology or sunlight-driven volatile processes (Kirk et al. 1995), Enceladus is the only icy body in the solar system known to be geologically active.

Enceladus provides living examples of phenomena that have been important at some time throughout the outer solar system. These processes can be studied as they happen on Enceladus, leading to understanding that can be applied to less currently active worlds. Already, Enceladus is testing models of shear heating and ice tectonics that were first developed for Europa, is challenging our understanding of tidal heating and orbital evolution of icy satellites, and the composition of its plume is shedding light on the internal chemistry of icy satellites and their possible oceans. Enceladus is also important because it is the source of the E-ring and the extensive torus of neutral and ionized species that fill the middle Saturnian magnetosphere, thus playing a pivotal role in the Saturnian system similar in some ways to Io's role in the Jovian system.

Evidence is accumulating that the plume source may involve liquid water, possibly in communication with a global or regional ocean that is likely to be in contact with the silicate core. Coupled with the rich chemistry apparent from the plume composition, and the energy supplied by tidal heating, the plume source provides a potential habitat for life. The plumes themselves allow the study of fresh samples from this environment, allowing relatively easy investigation of Enceladus' interior and its biological potential.

Many questions remain unanswered, including the following:

- Is the currently high level of activity on Enceladus atypical, and if not, how is the tidal heating and mass loss sustained over the long term?
- What accounts for the extreme variations in surface age, and why is the geology so symmetrical about the spin axis and the direction to Saturn?
- What mechanisms produce Enceladus' abundant and varied tectonic features?
- What generates the south polar plumes, and what are the mass loss rates?
- Is liquid water present in the interior, as a global or regional ocean, or locally at the source of the plumes? What is the detailed chemistry of these water bodies?
- Finally, can subsurface conditions sustain life, and is life actually present there?

Cassini will continue to address these questions with four more flybys in 2009 and 2010 (Table 21.1, Fig. 21.2), and (if approved) twelve additional flybys through 2015. Highlights in 2009 and 2010 will include deeper passages through the plume for in situ sampling, high resolution imaging of the plumes and additional very high resolution remote sensing of the surface, a plume solar occultation to map nitrogen abundance, and a gravity pass to search for south polar gravity anomalies.

Cassini still has much to tell us about Enceladus, but its orbit and instrumentation do not allow us to answer all the above questions. For instance, analysis of plume composition is limited by the mass range and resolution of the mass spectrometer, and the high flyby speeds prevent analysis of intact dust grains and may destroy complex molecules. The remote sensing instruments are not optimized for wide-area high-resolution coverage during the very limited time close to Enceladus afforded by the spacecraft's relatively high-speed flybys, and the configuration of the spacecraft does not permit all instruments to gather optimal data during all flybys. Cassini also lacks some instruments that would be of great value at Enceladus, such as ice-penetrating radar to map subsurface structure. Finally Cassini's Saturn-centric orbit prevents homogeneous global mapping and precludes many geophysical observations, including comprehensive measurements of Enceladus' tidal response, static gravity field, and magnetic properties, which would greatly expand our current limited information on its interior structure.

Accordingly, several recent studies have considered return missions to Enceladus. A 2006 JPL study (Reh et al. 2007) looked at missions that might be possible with a <$1 B New Frontiers budget, including a Stardust-like plume sample return mission, and a Saturn orbiter with multiple Enceladus flybys, like Cassini but with its mission and instrumentation optimized for Enceladus. The study concluded that while such missions would be scientifically worthwhile, expected costs of approximately $1.5 B each would not fit within the New Frontiers program, and the Enceladus sample return in particular would require significant technology development for high-speed plume sample capture. A NASA study of several more ambitious Flagship-class Enceladus missions was conducted by Goddard Spaceflight Center in 2007 (Razzaghi et al. 2007). Mission concepts included a Saturn orbiter with multiple Enceladus flybys and a soft lander, an Enceladus orbiter, and an Enceladus orbiter with soft lander, with costs in the $2.1 B–$3.3 B range. The Enceladus orbiter missions were the most challenging but most scientifically valuable, and made use of large numbers of gravity-assist flybys of Rhea and Dione to reduce delta-V for Enceladus orbit insertion. Orbiting Enceladus is challenging due to large orbital perturbations from Saturn, with polar orbits, which are preferred for global mapping and plume sampling, having stable lifetimes of only a few days. On the other hand, the mass of Enceladus is low enough that landing on the surface, once in orbit, would be relatively easy. The European TANDEM (Titan and Enceladus Mission) mission concept was proposed to the ESA Cosmic Vision program in 2007 (Coustenis et al. 2008). This was primarily a Titan mission, with an orbiter and landers, but included substantial Enceladus science from Saturn orbit, including a surface penetrator. The goals of this mission concept were incorporated into the 2008 joint NASA/ESA study of a Flagship-class Titan/Saturn System Mission, which would conduct Enceladus science with multiple flybys before entering Titan orbit. Such a mission may follow the Europa Jupiter Orbiter as the next-but-one outer solar system Flagship mission.

While the nature of the next mission after Cassini to visit Enceladus is still undecided, it remains a compelling target for future exploration, and Cassini itself will provide many new discoveries in the next few years. We look forward to the continuing exploration of this remarkable moon.

Acknowledgements We wish to thank everyone who has made these discoveries possible, by contributing to the success of the Cassini/Huygens project. This work was funded by the Cassini Project and by NASA.

List of Acronyms

CAPS	Cassini Plasma Spectrometer (Cassini instrument)
CDA	Cosmic Dust Analyzer (Cassini instrument)
CIRS	Composite Infrared Spectrometer (Cassini instrument)
FUV	Far Ultraviolet Spectrograph (part of UVIS)
HSP	High Speed Photometer (part of UVIS)
INMS	Ion and Neutral Mass Spectrometer (Cassini instrument)
IR	Infrared
ISS	Imaging Science Subsystem (Cassini instrument)
MAG	Magnetometer (Cassini instrument)
SLRI	Short-lived radioactive isotope
SPT	South Polar Terrain
TANDEM	Titan and Enceladus Mission
TST	Tiger Stripe Terrain
UV	Ultraviolet
UVIS	Ultraviolet Imaging Spectrograph (Cassini instrument)
VIMS	Visible and Infrared Mapping Spectrometer (Cassini instrument)

References

Abramov, O., Spencer J.R.: Endogenic heat from Enceladus' south polar fractures: New observations, and models of conductive surface heating. Icarus **199**, 189–196 (2009).

Anderson, D.L.: *Theory of the Earth*. Blackwell, London (1989).

Barr, A.C., McKinnon, W.B.: Convection in Enceladus' ice shell: Conditions for initiation. Geophys. Res. Lett. **34**, L09202. (2007a).

Barr, A.C., McKinnon, W.B.: Convection in ice I shells and mantles with self-consistent grain size, J. Geophys. Res. **112**, E02012 (2007b). doi: 10.1029/2006JE002781.

Barr, A.C.: Mobile lid convection beneath Enceladus' south polar terrain, J. Geophys. Res. **113**, E07009 (2008). doi: 10.1029/2008JE003114.

Baum, W.A., Kreidl, T., Westphal, J.A., Danielson, G.E., Seidelmann, P.K., Pascu, D., Currie, D.G.: Saturn's E ring. Icarus **47**, 84–96 (1981).

Benjamin, D., Wahr, J., Ray, R.D., Egbert, G.D. Desai, S.D.: Constraints on mantle anelasticity from geodetic observations, and implications for the J(2) anomaly, Geophys. J. Int. **165**, 3–16 (2006).

Bills, B.G.: Free and forced obliquities of the Galilean satellites of Jupiter. Icarus **175**, 233–247 (2005).

Bills, B.G. Nimmo, F.: Forced obliquity and moments of inertia of Titan. Icarus **196**, 293–297 (2008).

Bills, B.G., Nimmo F., Karatekin O., Van Hoolst, T., Rambaux, N, Levrard B., Laskar, J.: Rotational dynamics of Europa. In: Pappalardo, R., McKinnon, W. Khurana, K (eds.) *Europa*, Univ. Ariz. Press., Tucson, in press (2009).

Bland, M.T., Beyer R.A., Showman A.P.: Unstable extension of Enceladus' lithosphere. Icarus **192**, 92–105 (2007).

Brilliantov, N.V., Schmidt, J., Spahn, F.: Geysers of Enceladus: Quantitative analysis of qualitative models. Planet. Space Sci. **56**, 1596–1606 (2008).

Brown, R.H. and 24 co-authors: Composition and physical properties of Enceladus' surface. Science **311**, 1425–1428 (2006).

Buratti, B. J.: Enceladus – Implications of its unusual photometric properties. Icarus **75**, 113–126 (1988).

Buratti, B., Veverka, J.: Voyager photometry of Rhea, Dione, Tethys, Enceladus and Mimas. Icarus **58**, 254–264 (1984).

Buratti, B.J., Mosher, J.A., Nicholson, P.D., McGhee, C.A., French, R.G.: Near-infrared photometry of the Saturnian satellites during ring plane crossing. Icarus **136**, 223–231 (1998).

Chapelle, F.H., O'Neill K., Bradley P.M., Methe B.A., Ciufo S.A., Knobel L.L., Lovley D.R.: A hydrogen-based subsurface microbial community dominated by methanogens. Nature **415**, 312–315 (2002).

Chyba, C.F., Phillips, C.B.: Possible ecosystems and the search for life on Europa. Proc. Natl Acad. Sci. **98**, 801–804 (2001).

Clark, R.N.: Water frost and ice: The near-infrared spectral reflectance 0.65–2.5 μm. J. Geophys. Res. **86**, 3087–3096 (1981).

Clark, R.N., Lucey, P.G.: Spectral properties of ice–particulate mixtures and implications for remote sensing. I. Intimate mixtures. J. Geophys. Res. **89**, 6341–6348 (1984).

Collins, G.C., Goodman, J.C.: Enceladus' south polar sea Icarus **189**, 72–82 (2007).

Corliss, J.B., Baross, J.A., Hoffman, S.E.: An hypothesis concerning_the relationship between submarine hot springs and the origin of life. Oceanologica Acta **4**. suppl. C4, 59–69 (1981).

Coustenis, A. and 155 co-authors: TandEM: Titan and Enceladus mission. Exper. Astron. **23** (2008). doi: 10.1007/s10686-008-9103-z

Cruikshank, D.P.: Near-infrared studies of the satellites of Saturn and Uranus. Icarus 41, 246–**258** (1980).

Cruikshank, D.P., Owen, T.B., Dalle Ore, C., Geballe, T.R., Roush, T.L., de Bergh, C., Sandford, S.A., Poulet, F., Benedix, G.K., Emery, J.P.: A spectroscopic study of the surface of Saturn's large satellites: H_2O ice, tholins, and minor constituents. Icarus **175**, 268–283 (2005).

Czechowski, L.: Parameterized model of convection driven by tidal and radiogenic heating. Adv. Space Res. **38**, 788–793 (2006).

Davis, W.L., McKay, C.P.: Origins of life: A comparison of theories and application to Mars. Origins Life Evol. Biosph. **26**, 61–73 (1996).

Dermott, S.F., Thomas P.C.: The shape and internal structure of Mimas, Icarus **73**, 25–65 (1988).

Dermott, S.F., Malhotra, R., Murray, C.D.: Dynamics of the Uranian and Saturnian satellite systems: A chaotic route to melting Miranda? Icarus **76**, 295–334 (1988).

Dougherty, M.K., Khurana, K.K., Neubauer, F.M., Russell, C.T., Saur, J., Leisner, J.S., Burton, M.E.: Identification of a dynamic atmosphere at Enceladus with the Cassini magnetometer. Science **311**, 1406–1409 (2006).

Durham, W. B., Kirby S.H., Stern, L.A.: Effect of dispersed particulates on the rheology of water ice at planetary conditions, J. Geophys. Res. **97**, 20,883–20,897 (1992).

Durham, W.B., Stern, L.A.: Rheological properties of water ice-Applications to satellites of the outer planets. Ann. Rev. Earth Planet. Sci. **29**, 295–330 (2001).

Emery, J.P., Burr, D.M., Cruikshank, D.P., Brown, R.H., Dalton, J.B.: Near-infrared (0.8–4.0 μm) spectroscopy of Mimas, Enceladus, Tethys, and Rhea. Astron. Astrophys. **435**, 353–362 (2005).

Esposito, L.W., and 15 co-authors: Ultraviolet imaging spectroscopy shows an active Saturnian system. Science **307**, 1251–1255 (2005).

Feibelman, W. A.: Concerning the "D" ring of Saturn. Nature **214**, 793–794 (1967).

Friedson, A.J., Stevenson, D.J.: Viscosity of rock ice mixtures and applications to the evolution of icy satellites, Icarus **56**, 1–14 (1983).

Gaidos, E.J., Nealson, K.H., Kirschvink, J.L.: Life in ice-covered oceans. Science **284**, 1631–1633 (1999).

Giese, B., Wagner, R., Hussmann, H., Neukum, G., Perry, J., Helfenstein, P, Thomas, P.C: Enceladus: An estimate of heat flux and lithospheric thickness from flexurally supported topography. Geophys. Res. Lett. **35**, L24204 (2008).

Gioia, G., Chakraborty, P., Marshak, S., Kieffer, S.W.: Unified model of tectonics and heat transport in a frigid Enceladus. Proc. Natl Acad. Sci. **104**, 13578–13581 (2007).

Gladman, B., Dones, L., Levison, H.F., Burns, J.A.: Impact seeding and reseeding. in the inner solar system. Astrobiology **5**, 483–496 (2005).

Glein, C.R., Zolotov, M.Y., Shock, E.: The oxidation state of hydrothermal systems on early Enceladus, Icarus **197**, 157–163 (2008).

Goldsby, D.L., Kohlstedt, D.L.: Superplastic deformation in ice: Experimental observations. J. Geophys. Res. **106**, 11,017–11,030 (2001).

Gribb, T.T., Cooper, R.F.: Low frequency shear attenuation in polycrystalline olivine: Grain boundary diffusion and the physical significance of the Andrade model for viscoelastic rheology J. Geophys. Res. **103**, 27,267–27,279 (1998).

Grott, M., Sohl, F., Hussmann, H.: Degree-one convection and the origin of Enceladus' dichotomy, Icarus **191**, 203–210 (2007). doi:10.1016/j.icarus.2007.05.001.

Grundy, W.M., Buie, M.W., Stansberry, J.A., Spencer, J.R., Schmitt, B.: Near-infrared spectra of icy outer Solar System surfaces: Remote determination of H_2O ice temperatures. Icarus **142**, 536–549 (1999).

Haff, P.K., Siscoe, G.L., Eviatar, A.: Ring and plasma – The enigmae of Enceladus. Icarus **56**, 426–438 (1983).

Halevy, I., and Stewart S.T.: Is Enceladus' plume tidally controlled?, Geophys. Res. Lett. **35**, L12203 (2008). doi: 10.1029/2008GL034349.

Hamilton, D.P., Burns, J.A.: Origin of Saturn's E-ring: Self-sustained, naturally. Science **264**, 5158 (1994).

Han, L., Showman, A.P.: Implications of shear heating and fracture zones for ridge formation on Europa, Geophys. Res. Lett. **35**, L03202 (2008). doi: 10.1029/2007GL031957.

Hand, K.P., Carlson, R.W., Chyba, C.F.: Energy, chemical disequilibrium, and geological constraints on Europa. Astrobiology **7**, 1006–1022 (2007).

Hansen, C. J., Esposito L., Stewart, A.I.F., Colwell, J., Hendrix, A., Pryor, W., Shemansky, D., West R.: Enceladus' water vapor plume. Science **311**, 1422–1425 (2006).

Hansen, C.J., Esposito, L.W., Stewart, A.I.F., Meinke, B., Wallis, B., Colwell, J.E., Hendrix, A.R., Larsen, K., Pryor, W., Tian, F.: Water vapor jets inside the plume of gas leaving Enceladus. Nature **456**, 477–479 (2008).

Hedman, M.M., Nicholson, P.D., Showalter, M.R., Brown, R.H., Buratti, B.J., Clark R.N.: Spectral observations of the Enceladus plume with Cassini-VIMS. Astron. J. **693**, 1749–1762 (2009).

Helfenstein, P., Thomas, P.C., Veverka, J., Burns, J.A., Roatsch, T., Giese, B., Wagner, R., Denk, T., Neukum, G., Turtle, E.P., Perry, J., Bray, V., Rathbun, J., Porco, C.C.: Tectonism and terrain evolution on Enceladus,. Icarus, in press (2009).

Hoppa, G.V., Tufts, R., Greenberg, R., Geissler, P.E.: Formation of cycloidal features on Europa, Science **285**, 1899–1902 (1999).

Howett, C.J.A., Spencer, J.R., Pearl, J.C., Segura, M.: Thermal inertia and bolometric albedo for Mimas, Enceladus, Dione, Rhea and Iapetus as derived from Cassini/CIRS measurements. Icarus: doi: 10.1016/j.icarus.2009.07.016 (2009).

Hurford, T.A., Helfenstein, P., Hoppa, B.V., Greenberg, R., Bills, B.: Eruptions arising from tidally controlled periodic openings of rifts on Enceladus. Nature **447**, 292–294 (2007).

Hussmann, H., Spohn, T.: Thermal-orbital evolution of Io and Europa. Icarus **171**, 391–410 (2004).

Ingersoll, A.P., Pankine, A.A.: Models of the Enceladus plumes: Criteria for melting. Icarus, submitted (2009).

Jackson I., Faul, U.H., Gerald, J.D.F., Tan B.H.: Shear wave attenuation and dispersion in melt-bearing olivine polycrystals 1. Specimen fabrication and mechanical testing, J. Geophys. Res. **109**, B06201 (2004).

Jacobson, R.A., and 13 co-authors: The gravity field of the Saturnian system from satellite observations and spacecraft tracking data. Astron. J. **132**, 2520–2526 (2006).

Jaumann, R., and 18 co-authors: Distribution of icy particles across Enceladus' surface as derived from Cassini-VIMS measurements. Icarus **193**, 407–419 (2008).

Johnson, R.E., Famá, M., Liu, M., Baragiola, R.A., Sittler, E.C., Smith, H.T.: Sputtering of ice grains and icy satellites in Saturn's inner magnetosphere. Planet. Space Sci. **56**, 1238–1243 (2008).

Johnson, R.E., Smith, H.T., Tucker, O.J., Liu, M., Burger, M.H., Sittler, E.C., Tokar R. L.: The Enceladus and OH tori at Saturn. Astrophys. J. **644**, L137–L139 (2006).

Jones, G.H. and 20 co-authors: Fine jet structure of electrically charged grains in Enceladus's plume. Geophys. Res. Lett., in press (2009).

Juhász, A., Horányi, M.: Saturn's E ring: A dynamical approach. J. Geophys. Res. **107**, 1066 (2002).

Juhász, A., Horányi, M., Morfill, G.E.: Signatures of Enceladus in Saturn's E ring. Geophys. Res. Lett. **34**, L09104 (2007).

Jurac, S., Johnson, R.E., Richardson, J.D.: Saturn's E Ring and production of the neutral torus. Icarus **149**, 384–396 (2001).

Jurac, S., Richardson, J.D.: A self-consistent model of plasma and neutrals at Saturn: Neutral cloud morphology. J. Geophys. Res. **110**, A09220 (2005).

Jurac, S., McGrath, M.A., Johnson, R.E., Richardson, J.D., Vasyliunas, V.M., Eviatar, A.: Saturn: Search for a missing water source. Geophys. Res. Lett. **29**, 25–1 (2002).

Karato, S.: A dislocation model of seismic wave attenuation and microcreep in the Earth: Harold Jeffreys and the rheology of the solid Earth. Pure Appl. Geophys. **153**, 239–256 (1998).

Kargel J. and Pozio, S. (1996) The volcanic and tectonic history of Enceladus. Icarus 119, 385–404.

Kargel, J.S.: Enceladus: Cosmic gymnast, volatile miniworld. Science **311**, 1389–1391 (2006).

Kempf, S., Beckmann, U., Moragas-Klostermeyer, G., Postberg, F., Srama, R., Economou, T., Schmidt, J., Spahn, F., Grün, E.: The E ring in the vicinity of Enceladus. I. Spatial distribution and properties of the ring particles. Icarus **193**, 420–437 (2008).

Khurana, K.K., Dougherty, M.K., Russell, C.T., Leisner, J.S.: Mass loading of Saturn's magnetosphere near Enceladus. J. Geophys. Res. **112**, A08203 (2007).

Kieffer, S. W.: Dynamics and thermodynamics of volcanic eruptions: Implications for the plumes of Io. In: Morrison, D. (ed.) *Satellites of Jupiter*, pp. 647–723. Univ. Ariz. Press, Tucson (1982).

Kieffer, S., Lu, X., Bethke, C.M., Spencer, J.R., Marshak, S., Navrotsky, A.: A clathrate reservoir hypothesis for Enceladus' south polar plume. Science **314**, 1764–1766 (2006).

Kieffer, S.W., Lu, X., McFarquhar, G., Wohletz, K.H.: A redetermination of the ice/vapor ratio of Enceladus' plumes: Implications for sublimation and the lack of a liquid water reservoir. Icarus, submitted (2009).

Kirk, R.L., Soderblom, L.A., Brown, R.H., Kieffer, S.W., Kargel, J.S.: Triton's plumes: Discovery, characteristics, and models. In: Cruikshank, D.P. (ed.) *Neptune and Triton*, pp. 949–989. Univ. Ariz. Press, Tucson (1995).

Lazcano, A., Miller, S.L.: How long did it take for life to begin and evolve to cyanobacteria? Journal of Molecular Evolution **39**, 546–554 (1994).

Lin, L.-H., and 13 co-authors: Long-term sustainability of a high-energy, low-diversity crustal biome. Science **314**, 479–482 (2006).

Lissauer, J.J., Peale, S.J., Cuzzi J.N.: Ring torque on Janus and the melting of Enceladus, Icarus **58**, 159–168 (1984).

Lissauer, J.J., Squyres, S.W., Hartmann, W.K.: Bombardment history of the Saturn system. J. Geophys. Res. **93**, 13776–13804 (1988).

Lunine, J.I., Gautier, D.: Coupled physical and chemical evolution of volatiles in the protoplanetary disk: A tale of three elements. In: Festou, M.C., Keller, H.U., Weaver, H.A. (eds.), *Comets II*, pp. 105–113, Univ. Ariz. Press, Tucson (2004).

Manga, M., Wang, C.-Y.: Pressurized oceans and the eruption of liquid water on Europa and Enceladus. Geophys. Res. Lett. **34**, L07202 (2007).

Matson, D.L., Castillo, J.C., Lunine, J., Johnson, T.V.: Enceladus' plume: Compositional evidence for a hot interior. Icarus **187** 569–573 (2007).

Matsuyama, I., Nimmo, F.: Tectonic patterns on reoriented and despun planetary bodies. Icarus **195**, 459–473 (2008).

McCollom, T.M.: Methanogenesis as a potential source of chemical energy for primary biomass production by autotrophic organisms in hydrothermal systems on Europa. J. Geophys. Res. **104**, 30,729–30,742 (1999).

McCord, T.B., and 11 co-authors: Salts on Europa's surface detected by Galileo's Near Infrared Mapping Spectrometer. Science **280**, 1242 (1998).

McKay, C.P., Porco, C.C., Altheide, T. Davis, W.L., Kral, T.A.: The possible origin and persistence of life on Enceladus and detection of biomarkers in the plume. Astrobiology **8**, 909–919 (2008).

McKinnon, W. B.: On convection in ice I shells of outer solar system bodies, with specific application to Callisto. Icarus **183**, 435–450 (2006).

Melosh, H.J.: The rocky road to panspermia. Nature **332**, 687–688 (1988).

Meyer, J., Wisdom, J.: Tidal heating in Enceladus. Icarus **188**, 535–539 (2007).

Meyer, J., Wisdom, J.: Tidal evolution of Mimas, Enceladus, and Dione. Icarus **193**, 213–223 (2008).

Miller, D.J., Barnash, A.N., Bray, V.J., Turtle, E. P., Helfenstein, P., Squyres, S. W., Rathbun, J. A.: Interactions between impact craters and tectonic fractures on Enceladus and Dione. Workshop on Ices,

Oceans, and Fire: Satellites of the Outer Solar System, held August 13–15, 2007. Boulder, Colorado, LPI Contribution No. 1357, pp. 95–96 (2007).

Miller, S.L.: A production of amino acids under possible primitive Earth conditions. Science **117**, 528–529 (1953).

Mitri, G., Showman, A.P.: A model for the temperature-dependence of tidal dissipation in convective plumes on icy satellites: Implications for Europa and Enceladus, Icarus **195**, 758–764 (2008).

Moore, J.M., Schenk, P.M., Bruesch, L.S., Asphaug, E., McKinnon, W.B.: Large impact features on middle-sized icy satellites. Icarus **171**, 421–443 (2004).

Mousis, O, Gautier, D., Bockelee-Morvan, D.: An evolutionary turbulent model of Saturn's subnebula: Implications for the origin of the atmosphere of Titan. Icarus **156**, 162–175 (2002). doi:10.1016/icar.2001.6782.

Murray, C., Dermott, S.: *Solar System Dynamics*. Cambridge Univ. Press, Cambridge (1999).

Nash, D.B., Carr, M.H., Gradie, J., Hunten, D.M., Yoder, C.F.: Io. In: Burns J.A., Matthews, M.S. (eds.) *Satellites*, pp. 629–688. Univ. Ariz. Press, Tucson (1986).

Neukum, G.: Cratering records of the satellites of Jupiter and Saturn. Adv. Space Res. **5**, 107–116 (1985).

Newman, S.F., Buratti, B.J., Jaumann, R., Bauer, J.M., Momary, T.W.: Hydrogen peroxide on Enceladus. Astrophys. J. **670**, L143–L146 (2007).

Newman, S.F., Buratti, B.J., Brown, R.H., Jaumann, R., Bauer, J., Momary, T.: Photometric and spectral analysis of the distribution of crystalline and amorphous ices on Enceladus as seen by Cassini. Icarus **193**, 397–406 (2008).

Nicholson, P.D., Showalter, M.R., Dones, L., French, R.G., Larson, S.M., Lissauer, J.J., McGhee, C.A., Sicardy, B., Seitzer, P., Danielson, G.E.: Observations of Saturn's ring plane crossings in August and November 1995. Science **272**, 509–515 (1996).

Nimmo, F., Pappalardo, R.T.: Diapir-induced reorientation of Saturn's moon Enceladus. Nature **441**, 614–616 (2006).

Nimmo, F., Gaidos E.: Thermal consequences of strike-slip motion on Europa. J. Geophys. Res. **107**, 5021 (2002).

Nimmo, F., Spencer, J.R., Pappalardo, R.T., Mullen, M.E.: Shear heating as the origin of the plumes and heat flux on Enceladus. Nature **447**, 289–291 (2007).

Ojakangas, G.W., Stevenson, D.J.: Thermal state of an ice shell on Europa. Icarus **81**, 220–241 (1989).

Ojakangas, G.W., Stevenson, D.J.: Episodic volcanism of tidally-heated satellites with application to Io. Icarus **66**, 341–358 (1986).

Orgel, L.E.: The origin of life – how long did it take? Origins Life Evol. Biosphere. **28**, 91–96 (1998).

Pang, K.D., Voge, C.C., Rhoads, J.W., Ajello, J.M.: The E ring of Saturn and satellite Enceladus. J. Geophys. Res. **89**, 9459–9470 (1984).

Pappalardo, R.T., Barr A.C., The origin of domes on Europa: The role of thermally induced compositional diapirism. Geophys. Res. Lett. **31**, L01701 (2004).

Parkinson, C.D., Liang, M.-C., Hartman, H., Hansen, C.J., Tinetti, G., Meadows, V., Kirschvink, J.L., Yung Y.L.: Enceladus: Cassini observations and implications for the search for life. Astron. Astrophys. **463**, 353–357 (2007).

Parkinson, C.D., Liang, M.-C., Yung, Y.L., Kirschvink, J.L.: Habitability of Enceladus: Planetary conditions for life. Origins Life Evol. Biospheres (2008). doi:10.1007/s11084-008-9135-4.

Passey, Q.: Viscosity of the lithosphere of Enceladus. Icarus **53**, 105–120 (1983).

Peale S.J., Cassen P.: Contribution of tidal dissipation to lunar tidal history, Icarus **36**, 245–269 (1978).

Plescia, J.B., Boyce, J.M.: Crater numbers and geological histories of Iapetus, Enceladus, Tethys and Hyperion. Nature **301**, 666–670 (1983).

Porco, C. C., and 24 co-authors: Cassini observes the active south pole of Enceladus. Science **311**, 1393–1401 (2006).

Postberg, F., Kempf, S., Hillier, J.K., Srama, R., Green, S.F., McBride, N., Grün, E.: The E-ring in the vicinity of Enceladus II. Probing the moon's interior—The composition of E-ring particles. Icarus **193**, 438–454 (2008).

Postberg, F., Kempf, S., Schmidt, J., Brillantov, N., Beinsen, A., Abel, B., Buck, U., Srama, R.: Sodium salts in E Ring ice grains from an ocean below Enceladus' surface. Nature **459**, 1098–1101 (2009).

Rappaport, N.J., Iess, L., Tortora, P., Anabtawi, A., Asmar, S., Somenzi, L., Zingoni, F.: Mass and interior of Enceladus from Cassini data analysis, Icarus **190**, 175–178 (2007).

Razzaghi, A., Di Pietro, D., Simon-Miller, A., Spencer, J.: Enceladus Flagship Mission Concept Study. NASA-Goddard Spaceflight Center, http://www.lpi.usra.edu/opag/Enceladus_Public_Report.pdf (2007). Accessed 9 April 2009.

Reh, K., Elliot, J., Spilker, T., Jorgensen, E., Spencer, J., Lorenz, R.: Titan and Enceladus $1B mission feasibility study report. JPL D-37401B (2007).

Roatsch, T., Wählisch, M., Giese, B., Hoffmeister, A., Matz, K.-D., Scholten, F., Kuhn, A., Wagner, R., Neukum, G., Helfenstein, P., Porco, C.: High-resolution Enceladus atlas derived from Cassini-ISS images. Planet. Space Sci. **56**, 109–116 (2008).

Roberts, J.H., Nimmo F.: Tidal heating and the long-term stability of a subsurface ocean on Enceladus. Icarus **194**, 675–689 (2008a).

Roberts, J.H., Nimmo F.: Near-surface heating on Enceladus and the south polar thermal anomaly. Geophys. Res. Lett. **35** L09201 (2008b).

Roddier, C., Roddier, F., Graves, J.E., Northcott M.: Discovery of an arc of particles near Enceladus' orbit: A possible key to the origin of the E ring. Icarus **136**, 50–59 (1998).

Ross, M., Schubert, G.: Tidal dissipation in a viscoelastic planet. Proc. 16th Lunar Planet Sci. Conf. Pt 2, J. Geophys Res. **91**, D447–D452 (1986).

Ross, M.N., Schubert, G.: Viscoelastic models of tidal heating in Enceladus, Icarus **78**, 90–101 (1989).

Rudolph, M.L., Manga, M.: Fracture penetration in planetary ice shells. Icarus **199**, 536–541 (2009).

Saur, J., Schilling, N., Neubauer, F.M., Strobel, D.F., Simon, S., Dougherty, M.K., Russell, C.T., Pappalardo, R.T.: Evidence for temporal variability of Enceladus' gas jets: Modeling of Cassini observations. Geophys. Res. Lett. **35**, 20105 (2008).

Schmidt, J., Brilliantov, N., Spahn, F., Kempf, S.: Slow dust in Enceladus' plume from condensation and wall collisions in tiger stripe fractures. Nature **451**, 685–688 (2008).

Schneider, N.M., Burger, M.H., Schaller, E.L., Brown, M.E., Johnson, R.E., Kargel, J.S., Dougherty, M., Achilleos N.: No sodium in Enceladus' vapor plumes. Nature **459**, 1102–1104 (2009).

Schubert, G., Anderson, J.D., Travis, B.J., Palguta, J.: Enceladus: Present internal structure and differentiation by early and long-term radiogenic heating. Icarus **188**, 345–355 (2007).

Segatz, M.T., Spohn, T., Ross, M.N., Schubert G.: Tidal dissipation, surface heat flow, and figure of viscoelastic models of Io. Icarus **75**, 187–206 (1988).

Shemansky, D.E., Matheson, P., Hall, D.T., Hu, H.-Y., Tripp, T.M.: Detection of the hydroxyl radical in the Saturn magnetosphere. Nature **363**, 329–331 (1993).

Shock, E.L.: Geochemical constraints on the origin of organic compounds in hydrothermal systems. Origins Life Evol Biosphere **20**, 331–367 (1990).

Showalter, M.R., Cuzzi, J.N., Larson, S.M.: Structure and particle properties of Saturn's E Ring. Icarus **94**, 451–473 (1991).

Showman A.P., Stevenson, D.J., Malhotra, R.: Coupled orbital and thermal evolution of Ganymede. Icarus **129**, 367–383 (1997).

Showman, A.P., Han, L.J.: Effects of plasticity on convection in an ice shell: Implications for Europa. Icarus **177**, 425–437 (2005).

Smith, B.A., and 28 co-authors: A new look at the Saturn system: The Voyager 2 images, Science **215**, 504–537 (1982).

Smith, H.T., Shappirio, M., Johnson, R.E., Reisenfeld, D., Sittler, E.C., Crary, F.J., McComas, D.J., Young, D.T.: Enceladus: The likely dominant nitrogen source in Saturn's magnetosphere. Icarus **188**, 356–366 (2008a).

Smith, H.T., Shappirio, M., Johnson, R.E., Reisenfeld, D., Sittler, E.C., Crary, F.J., McComas, D.J., Young, D.T.: Enceladus: A potential source of ammonia products and molecular nitrogen for Saturn's magnetosphere. J. Geophys. Res. **113**, A11206 (2008b).

Smith-Konter, B., Pappalardo R.T.: Tidally driven stress accumulation and shear failure of Enceladus's tiger stripes. Icarus **198**, 435–451 (2008).

Solomatov, V.S., Barr A.C.: Onset of convection in fluids with strongly temperature-dependent, power-law viscosity 2. Dependence on the initial perturbation. Phys. Earth and Planet. Int. **165**, 1–13 (2007).

Sotin, C., Head, J.W., Tobie G.: Europa: Tidal heating of upwelling thermal plumes and the origin of lenticulae and chaos melting. Geophys. Res. Lett. **29**, 1233 (2002).

Spahn, F. and 15 co-authors: Cassini dust measurements at Enceladus and implications for the origin of the E ring. Science **311**, 1416–1418 (2006a).

Spahn, F. Albers, N., Hörning, M., Kempf, S., Krivov, A.V., Makuch, M., Schmidt, J., Seiß, M., Miodrag, S.: E ring dust sources: Implications from Cassini's dust measurements. Planet. Space Sci. **54**, 1024–1032 (2006b).

Spencer, J.R., Pearl, J.C., Segura, M., Flasar, F.M., Mamoutkine, A., Romani, P., Buratti, B.J., Hendrix, A.R., Spilker, L.J., Lopes, R.M.C.: Cassini Encounters Enceladus: Background and the discovery of a south polar hot spot, Science **311**, 1401–1405 (2006).

Spitale, J.N., Porco, C.C.: Association of the jets of Enceladus with the warmest regions on its south-polar fractures. Nature **449**, 695–697 (2007).

Squyres, S.W., Reynolds, R.T., Cassen P.M., Peale, S.J.: The evolution of Enceladus, Icarus **53**, 319–331 (1983).

Stevens, T.O., McKinley J.P.: Lithoautotrophic microbial ecosystems in deep basalt aquifers. Science **270**, 450–454 (1995).

Thomas, P.C. Burns, J.A., Helfenstein, P., Squyres, S., Veverka, J., Porco, C., Turtle, E.P., McEwen, A., Denk, T., Giese, B., Roatsch, T., Johnson, T.V., Jacobson, R.A.: Shapes of the Saturnian icy satellites and their significance. Icarus **190**, 573–584 (2007).

Tian, F., Stewart, A.I.F., Toon, O.B., Larsen, K.W., Esposito, L.W.: Monte Carlo simulations of the water vapor plumes on Enceladus. Icarus **188**, 154–161 (2007).

Tice, M.M., Lowe, D.R.: Photosynthetic microbial mats in the 3,416-Myr-old ocean. Nature **431**, 549–552 (2004).

Tobie, G., Mocquet, A., Sotin, C.: Tidal dissipation within large icy satellites: Applications to Europa and Titan. Icarus **177**, 534–549 (2005).

Tobie, G., Cadek, O., Sotin, C.: Solid tidal friction above a liquid water reservoir as the origin of the south pole hotspot on Enceladus, Icarus **196**, 642–652 (2008). doi:10.1016/j.icarus.2008.03.008.

Tyler, R. H.: Strong ocean tidal flow and heating on moons of the outer planets. Nature **456**, 770–772 (2008).

Verbiscer, A.J., French, R.G., McGhee, C.A.: The opposition surge of Enceladus: HST observations 338–1022nm. Icarus **173**, 66–83 (2005).

Verbiscer, A.J., Peterson, D.E., Skrutskie, M.F., Cushing, M., Helfenstein, P., Nelson, M.J. Smith, J.D., Wilson J. C.: Near-infrared spectra of the leading and trailing hemispheres of Enceladus. Icarus **182**, 211–223 (2006).

Verbiscer, A., French, R., Showalter, M., Helfenstein, P.: Enceladus: Cosmic graffiti artist caught in the act. Science **315**, 815 (2007).

Wächtershäuser, G.: The case for the chemoautotrophic origin of life in an iron-sulfur world. Origins Life Evol. Biosphere **20**,173–176 (1990).

Waite, J. H., and 16 co-authors: Ammonia, radiogenic Ar, organics, and deuterium measured in the plume of Saturn's icy moon Enceladus. Nature **460**, 487–490 (2009).

Waite, J. H., and 13 co-authors: Cassini Ion and Neutral Mass Spectrometer: Enceladus plume composition and structure. Science **311**, 1419–1422 (2006).

Weiss, B.P., Kirschvink, J.L., Baudenbacher, F.J., Vali, H., Peters, N.T., Macdonald, F.A., Wikswo J.P.: A low temperature transfer of ALH84001 from Mars to Earth. Science **290**, 791–795 (2000).

Wisdom, J.: Spin-orbit secondary resonance dynamics of Enceladus. Astron. J. **128**, 484–491 (2004).

Zahnle, K., Schenk, P., Levison, H., Dones L.: Cratering rates in the outer Solar System. Icarus **163**, 263–289 (2003).

Zolotov, M. Y.: An oceanic composition on early and today's Enceladus, Geophys. Res. Lett. **34**, L23203 (2007). doi:10.1029/2007GL031234.

Zschau, J. Tidal friction in the solid Earth: Loading tides versus body tides. In: Brosche P., Sundermann, J. (eds.) Tidal Friction and the Earth's Rotation. Springer, Berlin (1978).